6-19-2024

Optical Imaging to Investigate Neurovascular Injury, Repair, and Disease

Ryan Michael Bowen
Washington University – McKelvey School of Engineering

WASHINGTON UNIVERSITY IN ST. LOUIS
McKelvey School of Engineering
Department of Biomedical Engineering

Dissertation Examination Committee:
Jin-Moo Lee, Chair
Adam Bauer
Nico Dosenbach
Dan Moran
Colin Nichols

Optical Imaging to Investigate Neurovascular Injury, Repair, and Disease

by
Ryan Michael Bowen

A dissertation presented to
the McKelvey School of Engineering
of Washington University in
partial fulfillment of the
requirements for the degree
of Doctor of Philosophy

August 2024
St. Louis, Missouri

Table of Contents

List of Figures iv
List of Abbreviations vi
Acknowledgements vii
Abstract ix
Chapter 1: Optical Imaging in Neurovascular Disease 1
1.1 Introduction to Optical Imaging 1
1.2 Optical Imaging of Neural Activity 2
1.3 Neurovascular Coupling and Optical Imaging 5
1.4 Neurovascular Coupling in Disease 7
1.5 Cantu Syndrome 8
1.6 Summary of Findings 9
Chapter 2: Control of Neurovascular Coupling by ATP-Sensitive Potassium Channels 10
2.1 Abstract 10
2.2 Significance Statement 11
2.3 Introduction 11
2.4 Methods 13
2.4.1 Mouse lines 13
2.4.2 Cranial windows for optical imaging 14
2.4.3 Wide-field optical imaging 15
2.4.4 Image acquisition 16
2.4.5 Image processing 16
2.4.6 Patch-clamp analysis 17
2.4.7 Inter-contrast analysis 18
2.4.8 Statistics 19
2.5 Results 19
2.5.1 Pharmacological modulation of K_{ATP} markedly alters neurovascular coupling 19
2.5.2 K_{ATP} knockout or Cantu syndrome K_{ATP} GOF also reduce neurovascular coupling 22
2.6 Discussion 27
2.6.1 Ion channel players in neurovascular coupling 27
2.6.2 Dual mechanisms of K_{ATP} in neurovascular coupling 28
2.6.3 Feedback vasculo-neural coupling? 29
2.6.4 Pathological implications 29

2.7 Conclusion 31
Chapter 3: Optical Imaging in Neurovascular Injury and Repair 32
3.1 Optical Imaging after Stroke 32
3.2 Summary of Findings 35
Chapter 4: Early Changes in Spatiotemporal Dynamics of Remapped Circuits and Global Networks Predict Functional Recovery After Focal Ischemia in Mice 36
4.1 Abstract 36
4.2 Introduction 37
4.3 Methods 40
4.3.1 Study design 40
4.3.2 Mice and procedures 42
4.3.3 Wide-field optical imaging recordings 44
4.3.4 Optical imaging processing and analyses 45
4.3.5 Statistical analyses 48
4.4 Results 50
4.4.1 Variance in photothrombotic infarct size 50
4.4.2 Altering $S1_{FP}$ stroke size elicits markedly different remapping patterns 53
4.4.3 Neuronal fidelity is differentially disrupted after $S1_{FP}$ stroke in an infarct size-dependent manner 60
4.4.4 Disruptions in evoked coherence of bilateral forepaw somatosensory cortices predict functional outcome after stroke 64
4.4.5 Larger $S1_{FP}$ strokes trigger hyperconnectivity across the contralesional hemisphere and with ipsilesional remapped circuits 66
4.5 Discussion 70
4.5.1 Disparate spatial patterns of neuronal remapping after $S1_{FP}$ stroke 71
4.5.2 Temporal dynamics of remapped circuits 74
4.5.3 Connectivity changes after stroke 75
Chapter 5: Conclusions and Future Directions 78
5.1 Neurovascular Coupling in Cantu Syndrome 78
5.2 Early Repair and Long-Term Recovery after Stroke 87
References 93

List of Figures

Figure 2.1: Effect of pharmacological K_{ATP} modulation on neurovascular coupling and neural activity 21

Figure 2.2: Effect of SUR2 KO on neurovascular coupling 24

Figure 2.3: Effect of K_{ATP} GOF mutation on neurovascular coupling 26

Figure 4.1: Experimental design to predict long-term stroke recovery using early patterns of repair 41

Figure 4.2: Quantification of infarct size using optical imaging is a reliable proxy of histological infarct volume 51

Figure 4.S1: Multiple Week 1 imaging measures predict histological infarct size at Week 8 52

Figure 4.S2: Stimulus-evoked GCaMP fluorescence is markedly attenuated after stroke in mice 55

Figure 4.3: Altering $S1_{FP}$ stroke size elicits differential changes in early spatial remapping patterns of affected paw circuits 56

Figure 4.4: Larger stroke in $S1_{FP}$ causes diffuse remapping of unaffected forepaw circuits 59

Figure 4.5: Neuronal fidelity of affected and unaffected circuits is differentially impacted in an infarct size-dependent fashion after $S1_{FP}$ stroke 62

Figure 4.6: $S1_{FP}$ stroke size disparately influences bilateral coherence changes during unilateral stimulation of each forepaw 65

Figure 4.7: Larger stroke in $S1_{FP}$ causes substantial and maladaptive hyperconnectivity within the contralesional hemisphere 67

Figure 4.S3: Early changes in dynamics of local circuits and global networks predict functional recovery independently of infarct size 69

Figure 5.1: Role of pericyte K_{ATP} in neurovascular coupling response 82

Figure 5.2: Proposed dual role of Kir6.1/SUR2-dependent K_{ATP} channels in neurovascular coupling 84

List of Abbreviations

K_{ATP}: ATP-sensitive subtype 6 inward rectifying potassium channels

$S1_{FP}$: Primary forepaw somatosensory cortex

Acknowledgements

As I reflect on my journey to get to this point, I am incredibly humbled while considering the people to whom I owe much of this honor. This achievement is not only mine; it is a shared victory for those who have encouraged my curiosity, picked me up when I was defeated, and pushed me to better myself, both in science and in life. I am deeply thankful:

…To Jin-Moo, for mentoring me as I grow as a scientist and leader. I am constantly amazed by your breadth of knowledge, your willingness to meet with me regardless of how little time you may have in your week, and your seemingly infinite patience with me and everyone else around you.

…To Adam, for teaching me more about optical imaging in our conversations than I learned in the remainder of my graduate school experience, and for your candor when I asked for help.

…To my thesis committee members: Nico, Dan, and Colin, for your encouragement and advice throughout my PhD journey.

…To Zach, for teaching me everything I know how to do in the Lee lab, for validating my neuroses (“People don’t put things back where they found them and it upsets me,” may be the simplest, most apt description of this), and for your camaraderie and mentorship in matters both personal and scientific.

…To Nathan York, for all of your help, and willingness to help, with the Cantu experiments. I could not have done this without you.

…To Eric and Asher, for the lively discussions about science, and for complimenting my work and giving me confidence in it.

…To the rest of the Lee lab, for your companionship and support during the last few years. I wouldn't be here without all the laughs to keep me sane, not to mention all of the murine, histological, and administrative aid.

…To my parents, for reassuring me through the doldrums of my third and fourth years of the PhD program and helping me to maintain my perspective. You have kept me grounded and supported me through my failures and triumphs, and I am forever grateful for all you have done for me.

…To my brother, Collin, for providing company, listening to me, and asking questions that inspire new perspectives and help solve problems.

….To my friends from all stages of life, for the warm greetings, laughs, and open ears, no matter how long we've been apart.

…To my friends from graduate school, for the Cardinals, Blues, and Chiefs games, closing down HandleBar, Mardi Gras, and feeding my NFL and Domino's obsessions.

…To Galina, for your unwavering support and love; your smile was the highlight of more of my days than you know. You have encouraged me to grow in every aspect of my life, even in my patience for the catastrophe that is driving in St. Louis.

…To the NIH (1F31NS122499), for financial support.

Ryan Bowen

Washington University in St. Louis

August 2024

ABSTRACT OF THE DISSERTATION

Optical Imaging to Investigate Neurovascular Injury, Repair, and Disease

by

Ryan Michael Bowen

Doctor of Philosophy in Biomedical Engineering

Washington University in St. Louis, 2024

Professor Jin-Moo Lee, Chair

Local neural circuitry and global neural networks in the brain are often investigated using mesoscopic, hemodynamic imaging such as optical intrinsic signal (OIS) imaging or functional magnetic resonance imaging (fMRI), relying on oximetric signals as proxies of neural activity. However, the tight neurovascular coupling that ties regional changes in blood flow to changes in neural activity in normal states can be severely disrupted in disease states. I show that neurovascular coupling is significantly interrupted in mouse models of Cantu syndrome, a rare disease caused by gain-of-function mutations in ATP-sensitive potassium (K_{ATP}) channels. Such marked disruptions in neurovascular coupling in disease states like Cantu motivate the direct measurement of neural activity to examine changes in local circuits and global networks in neurovascular disease, such as stroke. I then demonstrate that minute increases in stroke size in mice can elicit very different profiles of repair and recovery, and that early changes in spatiotemporal dynamics of both local circuits and global networks predict long-term functional outcome after stroke. Together, these results add to our understanding of neurovascular coupling, raise

concerns about the validity of hemodynamic signals as surrogate measures of neural activity in disease states, and help to elucidate early mechanisms of repair in injured neural circuits and networks.

Chapter 1:

Optical Imaging in

Neurovascular Disease

1.1 Introduction to Optical Imaging

Since its discovery almost 50 years ago [1], optical imaging has burgeoned into an incredibly useful neuroimaging technique, especially in animal models. One of the first uses of optical imaging in neuroscience showed that changes in diffuse light reflectance gathered from exposed cortical tissue of cats could be observed during visual evoked activity [1]. It was later discovered that these changes in diffuse reflectance, termed the optical intrinsic signal (OIS), were owed to changes in concentrations of intrinsic chromophores, such as hemoglobin [2-4], cytochromes [5, 6], and other chromophores within the vasculature of a tissue. Though hemoglobin is the most common intrinsic chromophore studied in optical imaging, recent breakthroughs in FAD and NADH optical imaging have shed light on spatial metabolism patterns in normal states [7, 8], as well as various disease states, such as cancer [9, 10].

Often compared to other hemodynamic imaging modalities like functional magnetic resonance imaging (fMRI), optical imaging benefits from a higher temporal resolution than

its rivals. While early investigations of OIS were performed at a sampling frequency around 5 Hz [1, 2], more recent developments have pushed the boundaries of its temporal resolution up to over 25 Hz, making optical imaging a far quicker readout of hemodynamics than other oximetric measures. When used in conjunction with genetic and pharmacological manipulations, this level of temporal resolution can help to tease apart the contributions of different tissue and cell types to hemodynamic responses. Access to higher frequency ranges also allows for the examination of faster hemodynamic and neural activity.

1.2 Optical Imaging of Neural Activity

Given its temporal and spatial precision, scientists recognized the potential of optical imaging for the direct measurement of neural activity *in vivo*, motivating a new wave of advancements in optical imaging to realize this potential. Voltage-sensitive dyes (VSDs), the first iteration of this technology, were first used in 1974 [11] as an optical alternative for the measurement of electric potentials in voltage clamp experiments. While proving very useful, *in vivo* VSD imaging requires invasive craniotomies, rendering them better suited for acute preparations and poorly suited for longitudinal experiments. VSDs have recently been replaced by genetically encoded calcium indicators (GECIs), which have ballooned in popularity over the last 15 years [12], allowing for genetic encoding of fluorescent calcium indicators in animal models. GCaMP, a fusion protein of calmodulin and green fluorescent protein (GFP) [13, 14], has been the most commonly used GECI in the past 15 years due to its availability, flexibility, and fast dynamics.

One of the salient advantages of GECIs lies in their genetic encoding, allowing them to be expressed under various promoters, which can target them to specific cell types. As 80-90% of cells in the cortex are excitatory [15], most GECI use has focused on expression in excitatory cells. Thy1, one of the most popular promoters for the expression of GECIs, was first used to target GCaMP expression to a subset of excitatory neurons in the mouse cortex, and shows robust fluorophore expression in layers 2/3 and 5 [16]. Recently, GECIs have begun to be expressed under inhibitory cell-specific promoters, such as the PV promoter [17, 18]. Though current leading GECI kinetics are not yet fast enough to examine activity at the frequency ranges at which most interneurons operate, targeted expression of GECIs in inhibitory cells may help to distinguish the roles inhibitory interneurons play in local circuits and global brain networks.

However, with every advancement comes challenges. In its beginnings, skeptics questioned the validity of GCaMP recordings as a reliable readout of population-level neural activity. This criticism was answered in the finding that GCaMP activity is significantly correlated to multi-unit activity of electrophysiological recordings [19]. It was also noted that the emission spectrum of GCaMP overlaps with the emission spectrum of hemoglobin, causing artifactual bleed-through of hemodynamic signals into GCaMP fluorescence signals. This characteristic of GCaMP's spectroscopy created challenges for the optical imaging community, but multiple methods have been developed to remove hemodynamic confound from GCaMP fluorescence activity. Initial correction methods used diffuse reflectance levels to measure the proportion of light absorbed by

hemoglobin, and then inferred information about hemoglobin concentrations based on a modified Beer-Lambert law relating light absorption by hemoglobin to mean scattering path through tissues [20, 21]. More recent work has further developed this correction method by applying a linear model of the modified Beer-Lambert law to each pixel to avoid the inaccuracies of estimating physical parameters, like scattering path length, in different spatial locations of the cortex [22]. Both methods have effectively removed artifactual hemoglobin signals from GCaMP fluorescence activity and greatly improved the fidelity of the direct measurement of neural activity during optical imaging. Moreover, the advent of red-shifted calcium indicators, such as RGECO, along with improvements in GECI signal-to-noise ratio, have further enhanced optical calcium imaging techniques, ridding calcium indicators of much of the hemodynamic confound that plagued green-shifted fluorophores, while simultaneously improving their signaling efficiency and decreasing signal attenuation in deeper cortical layers [12, 23].

In addition to its temporal precision, the other supreme advantage of optical imaging is the large viewing window with which it can be performed. In rodents, whose entire dorsal neocortex is visible during wide-field optical imaging, this is useful for the investigation of correlations between fluorescence signals across the cortex, known as functional connectivity (FC), which provide a proxy measure of network connectivity between anatomically distant regions. Many pathologies, like schizophrenia [24] and stroke [25-28], show abnormalities in network connectivity, suggesting that network integrity is essential for proper brain function. With the arrival of GECIs, optical imaging

could be used to study network topologies and function without the confound of neurovascular coupling, which is altered in many disease states and will be described in more detail in the next section. The spatial resolution of optical imaging has rendered sharper topologies of functional networks, while its temporal resolution, aided by the fast kinetics of GECIs, has allowed access to higher frequency bands of neural networks.

1.3 Neurovascular Coupling and Optical Imaging

Blood flow and hemodynamic signals have long been associated with underlying neural activity, with the first hypotheses of this phenomenon, known as neurovascular coupling, originating over 100 years ago [29, 30]. Canonical fMRI studies in the late 1990s linked neural activity with increased local oxygen metabolism in humans [31, 32]. Since then, it has been well established that neural activity drives a hemodynamic response to replenish oxygen and metabolic fuel.

Although myriad observations have been made about the characteristics and dynamics of neurovascular coupling in both healthy and disease states, the mechanisms behind this phenomenon are still poorly understood. The simplest understanding of neurovascular coupling relies on metabolic molecular signaling cascades, including mediating factors such as NAD+/NADH (nicotinamide adenine dinucleotide/+hydrogen) balance, ATP/ADP (adenosine tri/biphosphate) balance, and lactate [33-35]. In this hypothesis, neural activity creates a metabolic deficit in these proposed molecular factors, which then elicits vasodilation, leading to increases in blood flow. The principal competitor

to this idea holds natural byproducts of neural activity, such as neurotransmitter release and changes in ionic gradients, to be the primary drivers of changes in blood flow, skipping any sort of metabolic sensing or signaling [33, 36, 37].

With the addition of GECIs to the optical neuroimaging field, simultaneous monitoring of neural and hemodynamic activity has opened new doors for the analysis of neurovascular coupling. Computational advancements in signal processing have allowed for the creation of hemodynamic response functions (HRF) to quantify features of the hemodynamic response to neural activity. While this approach had existed in fMRI analysis for years, its use was predictive, trying to make inferences about unmeasured underlying neural activity based on measured hemodynamic responses, and then in turn making conclusions about the dynamics of neurovascular coupling [38]. It was not until the introduction of GECIs to optical imaging that the simultaneous measurement of neural and hemodynamic activity could be performed on the same system. Since then, the study of neurovascular coupling has been streamlined, especially in experiments aimed at elucidating the effects of drugs and disease on hemodynamic responses to neural activity.

Recently, developments in two-photon microscopy have allowed for the measurement of changes in microvascular diameters, and it has been demonstrated that drivers of blood flow changes, including changes in synaptic activity, metabolite concentrations, and metabolic-sensing ion channel activity, preferentially act on first order capillaries and capillary sphincters rather than on arterioles and higher order capillaries

[39]. Furthermore, local increases in potassium ion concentrations ([K+]) caused by neural activity have been shown to activate subtype 2 inward rectifying potassium channels (Kir2) in vascular endothelial cells, causing rapid hyperpolarization of vascular endothelial cells surrounding arterioles [40] and vasodilation. Together, these results suggest a role for metabolic-sensing ion channels in vascular cells in the control of neurovascular coupling, a subject that will be addressed in depth in Chapter 2. Still, advances in microscopic technologies and techniques to image cellular level activity will be imperative for elucidating causative mechanisms of neurovascular coupling.

1.4 Neurovascular Coupling in Disease

Recruitment of so many physiological resources to maintain tight neurovascular coupling is a steep cost, and disruptions in this highly regulated system coincide with adverse results. Indeed, disrupted neurovascular coupling can be observed in many disease states, such as Alzheimer's disease [41-45], frontotemporal dementia [42], Amyotrophic Lateral Sclerosis (ALS) [42, 46], Parkinson's Disease [42, 47], hypertension [42, 48], and stroke [41, 42, 49-51]. Changes in the parameters and dynamics of functional hyperemia, the state in which cerebral blood flow locally increases following amplified neural activity, can thus create inconsistencies in neurovascular coupling between healthy and disease states. Hemodynamic-based imaging, such as optical intrinsic signal imaging techniques and fMRI [52], therefore present a conundrum when attempting to indirectly measure neural activity from oximetric signals in disease states.

1.5 Cantu Syndrome

In Section 1.3, I briefly discussed the role of metabolic-sensing potassium channels expressed in vascular cells in neurovascular coupling. Although their exact role is still unclear, pathologies of these channels offer insight into their responsibility in neurovascular coupling, and animal models of such pathologies are therefore of great value to the scientific community. One such pathology is Cantu syndrome, a very rare disease caused by gain-of-function mutations in genes KCNJ8 and ABCC9, which encode the pore-forming (Kir6.1) and regulatory (SUR2) subunits of the ATP-sensitive type 6 inward rectifying potassium channel (K_{ATP}), respectively [53-56]. This subclass of potassium channel is most commonly expressed in endothelial and mural cells and is activated by Mg-ADP and inhibited by ATP, linking it to metabolism. The function of Kir6 channels is to hyperpolarize cells in which they are expressed, leading to relaxation of endothelial and mural cells, which dilates blood vessels and allows increased regional blood flow. As Cantu syndrome represents gain of function in these channels, symptoms generally relate to the decreased vascular tone observed in the disease, and include cardiac hypertrophy, hypotension, dilated and tortuous blood vessels, and pericardial effusion [53, 57, 58].

Murine models of Cantu syndrome express point mutations in either Kir6.1 or SUR2, with Kir6.1 mutations leading to more extreme cardiovascular phenotypes and being lethal when mutations are homozygous [57]. Aortic smooth muscle cells from these animal models have shown higher potassium conductance in both Kir6.1 and SUR2

mutant cells during whole cell voltage clamp recordings, with Kir6.1 mutants showing more extreme conductance increases than those observed in SUR2 mutants [57]. These conductance changes are also noted in the presence of the K_{ATP} activator pinacidil and inhibitor glibenclamide [57]. However, the effects of these genetic mutations and pharmacological manipulations on hemodynamics *in vivo* remain unknown.

1.6 Summary of Findings

To investigate the role of K_{ATP} channels in neurovascular coupling of mice *in vivo*, we used wide-field optical imaging to examine differences in hemodynamic responses to mechanical whisker stimulation between Cantu mutant and wild-type mice administered pinacidil and glibenclamide. Both increased (pinacidil) and decreased (glibenclamide) K_{ATP} activity via pharmacological intervention significantly disrupted neurovascular coupling in the cerebral cortex of wild-type mice, with pinacidil completely abolishing coupling and glibenclamide slowing and attenuating the hemodynamic response. Kir6.1 and SUR2 mutant animals demonstrated a similar slowed and reduced hemodynamic response at baseline to that observed in wild-type mice after administration of glibenclamide. Cantu mouse models exhibited inherent differences in neurovascular coupling compared to wild-type mice, in addition to showing an enhanced sensitivity to pinacidil during a dose response experiment. These results demonstrate the importance of homeostatic K_{ATP} activity in neurovascular coupling and provide motivation for further investigation into cell-type-specific contributions of K_{ATP} activity to neurovascular coupling in Cantu syndrome and other neurovascular diseases.

Chapter 2:

Control of Neurovascular Coupling by ATP-Sensitive Potassium Channels

2.1 Abstract

Regional blood flow within the brain is tightly coupled to regional neural activity, a process known as neurovascular coupling (NVC). In this study, we demonstrate the striking controlling role of SUR2- and Kir6.1-dependent ATP-sensitive potassium (K_{ATP}) channels in NVC, in the sensory cortex of conscious mice, in response to mechanical stimuli *in-vivo*. We demonstrate that either increased (pinacidil-activated) or decreased (glibenclamide-inhibited) K_{ATP} activity markedly disrupts NVC; pinacidil-activation is capable of completely abolishing stimulus-evoked cortical hemodynamic responses, while glibenclamide slows and reduces the response. The response is similarly slowed and reduced in SUR2 KO animals, as in Kir6.1 KO animals, demonstrating the clear role of both subunits. Gain-of-function (GOF) mutations in Kir6.1 and SUR2 underlie the rare channelopathy, Cantú syndrome. Compared to wild type mice, mouse models of Cantú syndrome exhibit baseline alterations in NVC as well as increased sensitivity to pinacidil. The study reveals the dramatic effects of either increasing or decreasing SUR2/Kir6.1-dependent K_{ATP} activity has on NVC, whether pharmacologically and genetically induced,

with important relevance for monogenic K_{ATP} channel diseases and for more common brain pathologies.

2.2 Significance Statement

Tight coupling of neural activity and blood flow is necessary to maintain normal brain function. In this study we provide *in vivo* demonstration of the dramatic effects of altering K_{ATP} activity on NVC, whether pharmacologically or genetically. Thus, K_{ATP} channels are revealed as important targets for modulation of NVC and a source of dysfunction in disease that results from or leads to changes in K_{ATP} channel activity such as occurs with Cantú syndrome and AIMS.

2.3 Introduction

It has long been recognized that neural activity is closely related to cerebral blood flow (CBF), and the close spatial and temporal relationship between neural activity and CBF, termed neurovascular coupling (NVC), is the basis for functional magnetic resonance imaging (fMRI) [59]. Appropriate NVC is generally assumed to be necessary for temporal matching of blood supply to neural demand, and disruption of NVC in various brain pathologies may represent a causal basis for neural dysfunction [59]. Multiple cell types, including capillary endothelial cells, astrocytes, and pericytes, have been implicated in the coupling of neural activity to increased blood flow, but underlying bases remain poorly understood. Various studies have elucidated mechanisms by which

metabolic by-products of neural activity may trigger electrical responses in nearby vascular smooth muscle (VSM) and pericytes that reduce their contractile state, leading to arteriolar and capillary dilation, and to increased blood flow [60, 61]. One potential metabolic by-product signal is elevated external [K^+], a rapid and potent vasodilator [62]. Local release of K^+ can activate Kir2 channels in vascular endothelium leading to hyperpolarization of upstream VSM, via gap junctional coupling, and consequent vasorelaxation leading to locally increased blood flow [63].

Recent studies have also implicated ATP-sensitive potassium (K_{ATP}) channels as additional transducers of NVC within the neurovascular unit [64, 65]. K_{ATP} channels are inhibited by intracellular ATP and activated by MgADP, thereby linking membrane potential to metabolic activity in K_{ATP}-channel-expressing cells [66]. These channels are formed as heteroctameric complexes, with 4 pore-forming Kir6.x subunits, responsible for ATP inhibition, and 4 regulatory SURx subunits responsible for Mg-ADP activation and sensitivity to agonists (e.g. Diazoxide/Pinacidil) and antagonists (e.g. Glibenclamide) [67]. Distinct K_{ATP} channel isoforms, encoded by two pairs of genes, are expressed in different cell types [68, 69]: *ABCC8*- and *KCNJ11*-encoded SUR1 and Kir6.2 are prominent in the pancreas and neurons, while *ABCC9*- and *KCNJ8*-encoded SUR2 and Kir6.1 are most widely expressed in vascular smooth muscle [70-72] and in cerebral pericytes [64, 73, 74].

In the present study we demonstrate a clear, controlling role for Kir6.1/SUR2B-type K_{ATP} in NVC *in vivo*, in conscious mice. Intriguingly, we demonstrate that either increase or decrease of K_{ATP} activity reduces NVC, with pharmacological K_{ATP} activation by pinacidil being capable of completely abolishing the response. Pharmacological inhibition of K_{ATP} with Glibenclamide or genetic knockout of the SUR2 subunit both result in slowed and diminished NVC. Severe loss–of-function (LOF) mutations in *ABCC9* underlie the very rare channelopathy ABCC9-dependent Intellectual disability Myopathy Syndrome (AIMS) [75], and the present results suggest a potential role for altered NVC in AIMS disease etiology. Conversely, gain-of-function (GOF) mutations in *KCNJ8* and *ABCC9* underlie the rare channelopathy, Cantú syndrome [69, 76, 77]. Characterized by cardiomegaly, hypertrichosis and distinct facial features, Cantú patients also exhibit dilated and tortuous cerebral vasculature and neurological abnormalities [78], as well as high incidence of migraines with aura [76]. Using a mouse model of *KCNJ8*-dependent Cantú syndrome, we further demonstrate a reduction in baseline NVC and increased sensitivity to Pinacidil, providing support for disrupted NVC, as a result of K_{ATP} GOF, being a causal mechanism of migraines in Cantú syndrome, or in subjects exposed to potassium channel opener drugs [79].

2.4 Methods

2.4.1 Mouse lines

All studies were performed in compliance with the standards for the care and use of animal subjects defined in the NIH Guide for the Care and Use of Laboratory Animals

and were reviewed and approved by the Washington University Institutional Animal Care and Use Committee. For optical imaging experiments including GCaMP, Thy1-GCaMP6f mice (JAX 024276) were crossed with the mouse genotype of interest. Littermate mice carrying only the GCaMP6 transgene were used for comparisons and mice were between 16 and 20 weeks old during experiments. Generation of Cantú mice using CRISPR/Cas9 genome editing was previously reported [69]. Briefly, *KCNJ8* [c.193G>A/195A>G] mutations were introduced to generate Kir6.1[V65M] (Kir6.1$^{wt/VM}$) mice which mimic the autosomal-dominant mimic Kir6.1[V65M] observed in human CS [80]. Male and female mice were used for all experimental groups.

2.4.2 Cranial windows for optical imaging

Mice were anesthetized with isoflurane (3.5 liters per minute for 4 minutes, 3-5% induction, 1.5% maintenance), and head-fixed in a stereotaxic frame. Temperature was maintained using a thermostatic heating pad. After fixation on a bite bar and lubrication of the eyes, the hair on the scalp was shaved and the scalp was cleaned with betadine and ethanol. A local injection of lidocaine was administered to the site of incision. The scalp was then incised and retracted along the midline. Metabond dental cement (C&B Metabond, Parkell Inc.) was used to secure a custom-designed Plexiglas window to the skull, completely covering the surgical opening. Mice were then placed in a temperature-controlled incubator and allowed to recover for at least 5 days. No effect of window implantation on behavior was noted.

2.4.3 Wide-field optical imaging

Wide-field optical imaging was performed to measure cortical calcium and hemodynamic activity, as previously [81-84]. The dorsal neocortex was illuminated sequentially by three light emitting diodes (LEDs) of wavelengths 470 nm (Mightex Systems, LCS-0470-50-22), 525 nm (Mightex Systems, LCS-0525-60-22), and 625 nm (Mightex Systems, LCS-0625-07-22). The 470 nm LED was used for GCaMP excitation and a 500-nm long pass filter (Semrock, FF01-500/LP-25) in front of the camera blocked residual excitation light from reaching the camera sensor. An additional 460/60 nm bandpass filter (FF01-460/60-25) was placed in front of the excitation source to spectrally separate fluorescence excitation light from fluorescence emission. The remaining LEDs provided diffuse reflectance illumination used for multispectral hemodynamic imaging. A custom light engine was built such that all LED beams were collimated using plano-convex lenses (Thorlabs, LA1433) and combined with dichroic beam combiners (Mightex Systems, LCS-BC25-0480, LCS-BC25-0605). Image detection was performed with a cooled, sCMOS camera (Zyla 5.5-USB3, Andor) with an 85-mm f/1.4 camera lens and 75 Hz acquisition framerate (25 Hz acquisition rate for each channel). The field of view was approximately 1 cm x 1 cm, covering the dorsal neocortex, and contained a 512 x 512-pixel array. To ensure a high SNR and acquisition rate, images were binned 4 x 4 on camera, resulting in images containing 128 x 128 pixels, with each pixel being approximately 78 μm x 78 μm. A series of linear polarizers were used in front of both the LED sources and the camera lens to reduce specular reflection from the mouse skull.

2.4.4 Image acquisition

LED illumination sequences and camera triggering was controlled by a data acquisition board (PCI-6733, National Instruments) using MATLAB (MathWorks). Solis (Oxford Instruments) was used for image acquisition.

Prior to data collection, mice were acclimated to head fixation while wrapped in a felt blanket for 20 minutes to ensure normal behavior before any imaging recordings were performed. Whisker stimulation was performed in awake mice for 5 minutes on the left and right whisker pads using computer controlled, 40 PSI air puffs in a block design (5 s rest; 5 s of 1 Hz, 0.1 s pulses; 10 s rest; 15 blocks/5 minutes recording per mouse).

2.4.5 Image processing

Brain masks were created for each imaging timepoint for each mouse, and all analyses that followed were performed only on pixels labeled as brain. Brain masks and image sequences of brain pixels were affine transformed to Paxinos atlas space using the cranial landmarks of the intersection of the frontonasal and interfrontal suture and the sagittal and lambdoid suture (lambda). Five seconds of dark frames were subtracted from all raw data prior to analysis. Images were temporally detrended as previously described [85]. Changes in 590nm and 625 nm reflectance were used for hemodynamic spectroscopy, using the modified Beer-Lambert Law [86]. The raw GCaMP fluorescence signal was corrected for artifacts due to hemoglobin absorption using 525-nm reflectance as previously described [83, 87]. For each mouse, maps of cortical responses to

peripheral whisker stimulation were created by averaging responses to each of the 5 air puffs per block. Regions of interest (ROIs) were defined using the GCaMP signal within right and left somatosensory whisker barrel cortex by thresholding individual and group-averaged evoked response maps, averaged across blocks and peaks at 50% of the maximum pixel intensity at each time point. The ROIs defined using GCaMP were used for analysis of hemoglobin signaling.

2.4.6 Patch-clamp analysis

Whole cell patch clamp recordings were performed on pericytes isolated from adult mice (Figure 5.1). NG2-dsred or PDGFRβ-GFP mice were used, to allow visual identification of cells expressing these two pericyte markers [88]. To isolate pericytes, adult mice were anesthetized with 2.5% avertin (10 ml;/kg, i.p.: Sigma-Aldrich) and cervical dislocation was performed. Dissociation of pericytes was carried out using the Neural Tissue Dissociation Kit (P) (Miltenyibiotec). In brief, the brain was removed and a small section of the parietal lobe placed in Hanks Balanced Salt Solution (HBSS) to clean the tissue. The tissue was then removed from solution and placed in digestion solution with enzyme P and cut into small pieces. This was digested for 17 min at 37^{o} C, followed by trituration 10x with a pastuer pipette and the subsequent addition of enzyme A. The digestion was then incubated for a further 12 min at 37^{o} C and then passed through a 21 gauge needle 10 times. The mix was then incubated for a further 10 min at 37^{o} C, and was then passed through a 70uM filter, spun down and resuspended in cell culture media.

The resulting cells were plated on shards of cover glass, on ice, which were used for patch clamp recordings after they were allowed to attach.

Whole-cell K_{ATP} currents were recorded using an Axopatch 200B amplifier and Digidata 1200 (Molecular Devices), following a previously published protocol for characterization of Kir6.1/SUR2 in SM cells [69]. Recordings were filtered at 1 kHz, and digitally sampled at 3 kHz. Currents were initially measured at a holding potential of –70 mV in a high-Na^+ bath solution containing (in mM) 120 NaCl, 6 KCl, 2.5 $CaCl_2$, 1.2 $MgCl_2$, 10 HEPES, and 12 glucose, with pH adjusted to 7.4 with NaOH before switching to a high-K^+ bath solution (130 KCl, 2.5 $CaCl_2$, 1.2 $MgCl_2$, 10 HEPES, and 12 glucose, with pH adjusted to 7.4 with KOH) in the absence and presence of pinacidil and glibenclamide as indicated. The pipette solution contained (in mM) 110 potassium aspartate, 30 KCl, 10 NaCl, 1 $MgCl_2$, 10 HEPES, 0.5 $CaCl_2$, 4 K_2HPO_4, and 5 EGTA, with pH adjusted to 7.2 with KOH.

2.4.7 Inter-contrast analysis

Cross-covariance between calcium and oxygenated hemoglobin (OxyHb) signals was used to estimate coupling between the mean calcium and oxygenated hemoglobin signals within the individual ROIs described above. This was done for each recording and then averaged within and across mice. From the cross-covariance functions, the peak amplitude, the time-to-peak amplitude (Peak lag), the full width at half maximum and the energy of cross-covariance (area under the squared covariance curves) were calculated.

2.4.8 Statistics

Data are presented as mean ± SEM, unless otherwise noted. Differences between two groups were tested using 2-tailed t-tests and among several groups were tested using analysis of variance (ANOVA) and post-hoc Turkey's test, assuming that the data are normally distributed for each variable. Significant differences among groups are indicated with p-values, and non-significant ($p > 0.05$) differences are not shown.

2.5 Results

2.5.1 Pharmacological modulation of K_{ATP} markedly alters neurovascular coupling

We first assessed the impact of pharmacological K_{ATP} channel activation and inhibition on NVC in awake conscious animals by IP injection of the K_{ATP} channel activator Pinacidil (40 mg/mL), or of the inhibitor Glibenclamide (2.5 mg/mL). The neural (GCaMP) and vascular (oxygenated hemoglobin, OxyHb) evoked response signals (stimulus: 1 Hz, 0.1-second, 40 PSI air puffs) within the whisker barrel cortex were measured before and after (20 minutes) drug injection, to determine baseline and drug-modulated responses (Figure 2.1A,B). In wild type (WT) mice, discrete whisker barrel GCaMP responses to each stimulus were reproducibly associated with a rapid local increase of OxyHb that was maintained during the stimulation period and then declined over 5-10 seconds following the end of stimulation. Glibenclamide treatment resulted in a delayed rise of the OxyHb signal and ~50% reduction in the maximum change in oxygenated hemoglobin (Oxy max, Figure 2.1B,C). Pinacidil had a more dramatic effect, essentially abolishing the OxyHb response (Figure 2.1B,C). Interestingly, both treatments slightly reduced the GCaMP

signal by ~25 % (Figure 2.1B,C). As an estimate of NVC, the relationship between GCaMP and OxyHb was quantified using cross-covariance. A significant reduction in coupling is demonstrated by reduced overall energy and reduced peak amplitude for both pinacidil and glibenclamide treatment (Figure 2.1D,E), and a significant shift in peak lag was observed in animals treated with Glibenclamide (Figure 2.1D,E).

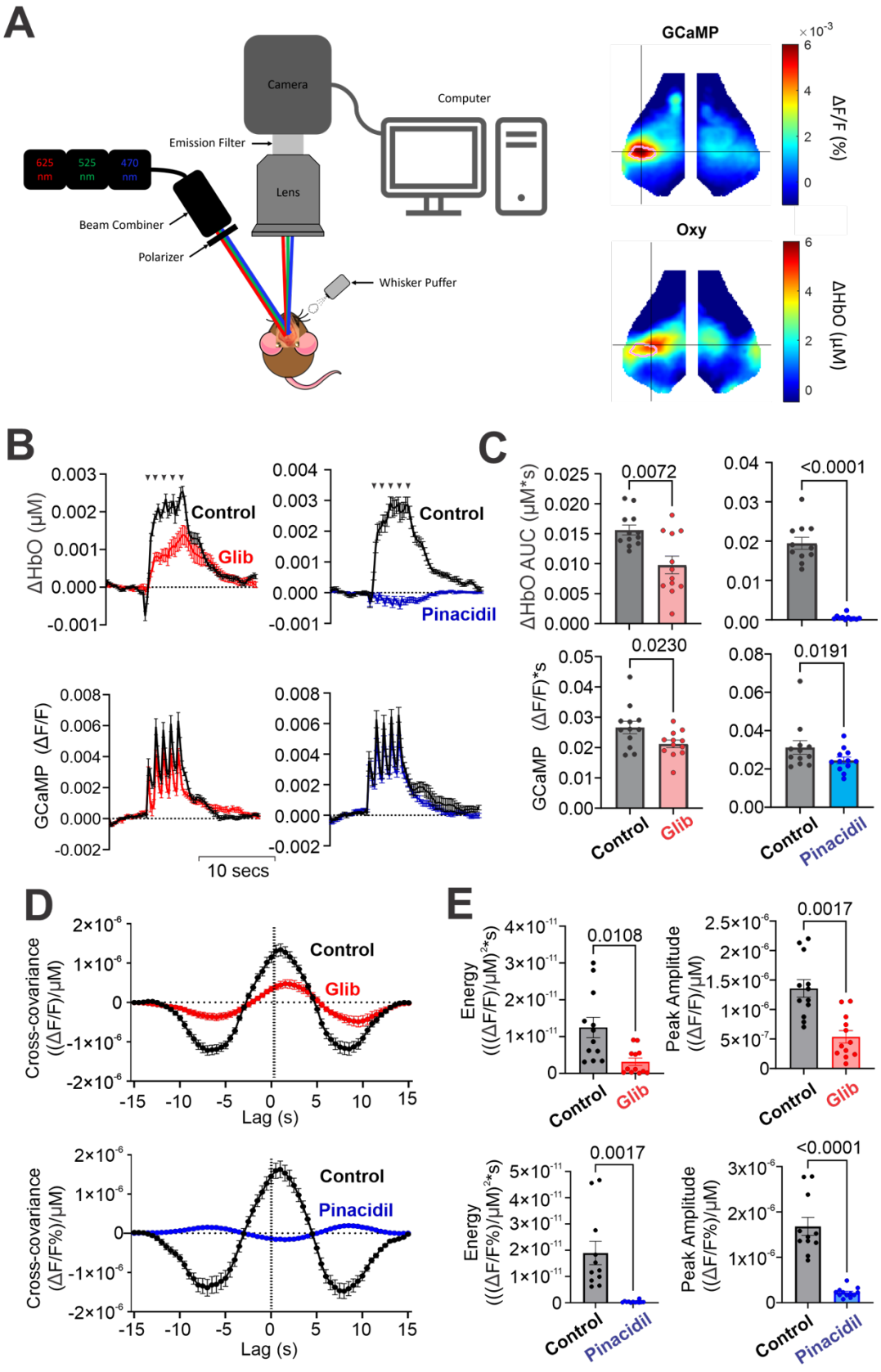
A
Camera
Computer
Emission Filter
625 nm
525 nm
470 nm
Lens
Beam Combiner
Polarizer
Whisker Puffer
GCaMP
Oxy
ΔF/F (%)
ΔHbO (μM)
B
ΔHbO (μM)
Control
Glib
Pinacidil
GCaMP (ΔF/F)
10 secs
C
ΔHbO AUC (μM*s)
0.0072
<0.0001
GCaMP (ΔF/F)*s
0.0230
0.0191
Control
Glib
Pinacidil
D
Cross-covariance ((ΔF/F)/μM)
Lag (s)
Cross-covariance (ΔF/F%)/μM)
E
Energy (((ΔF/F)/μM)^2*s)
0.0108
Peak Amplitude ((ΔF/F)/μM)
0.0017
Energy (((ΔF/F%)/μM)^2*s)
Peak Amplitude ((ΔF/F%)/μM)
<0.0001

Figure 2.1: Effect of pharmacological K_{ATP} modulation on neurovascular coupling and neural activity (A) (left) Experimental setup. The conscious mouse is head-fixed on the stage using non-reflective screws. LEDs illuminate the cortex sequentially and reflected light levels are captured by the camera during optical imaging recordings. Whisker stimulation is provided by an air puffer fixed to blow air on either side of the whiskers. Changes in light levels are then processed and analyzed using MATLAB. (right) Representative image showing average GCaMP and oxygenated hemoglobin (Oxy) signals during right whisker stimulation in control mouse. **(B)** Change in oxygenated hemoglobin (OxyHb, above) and GCaMP (below) signals during whisker stimulation (arrowheads) in control and in the presence of (0.025 mg/g) glibenclamide (left) or (0.4 mg/g) pinacidil treatment (n=14 hemispheres/7mice in each case, mean ± s.e.m. for each time point). **(C)** Mean area under the curve (± s.e.m.) of oxygenated hemoglobin (OxyHb, above) and GCaMP (below) signals, measured from ROIs as in C. **(D)** Average cross-covariance of GCaMP and Oxy signals from mice before and after treatment with glibenclamide (above) and pinacidil (below). **(E)** Average energy (± s.e.m.) of cross covariance in the positive direction as well as average peak amplitude (± s.e.m.) are shown for glibenclamide (above) and pinacidil (below).

2.5.2 K_{ATP} knockout or Cantu syndrome K_{ATP} GOF also reduce neurovascular coupling

Vascular K_{ATP} channels are generated by the Kir6.1 and SUR2B subunits, encoded by *KCNJ8* and *ABCC9*, respectively [72, 89]. Loss of *ABCC9*-dependent (and hence potentially *KCNJ8*-dependent) K_{ATP} channels results in a distinct complex disorder which we have termed ABCC9-dependent intellectual disability myopathy syndrome (AIMS) [75]. It has previously been demonstrated that loss of *KCNJ8*-encoded Kir6.1 disrupts NVC, with a delayed and reduced blood flow response to whisker stimulation in anesthetized animals [74]. Loss of SUR2 has previously been shown to attenuate

vasodilation induced by oxygen and glucose deprivation [89], although NVC has not previously been tested. We observe a delayed rise and ~30% reduction in the maximum amplitude of OxyHb in *ABCC9* (SUR2) KO mice (n=10, purple in Figure 2.2A,B). In marked contrast to WT mice, Pinacidil (400 mg/Kg) had almost no effect on NVC in these KO mice (Figure 2.2A,B), confirming that the striking abolition of NVC in WT mice (Figure 2.1C) is indeed through activation of SUR2-containing K_{ATP} channels. This further suggests that maximum K_{ATP} channel activation by Pinacidil in WT reduces resting vessel tone to the extent that no further dilation is possible in response to neural activity. Cross-covariance between OxyHb and GCaMP (Figure 2.2C,D) shows that, as with Glibenclamide treatment in WT, stimulus-evoked NVC is significantly delayed in SUR2 KO animals relative to control animals (Figure 2.2C, Time delays of ~1 s in WT animals and ~2.5 s in SUR2 KO animals), although cross-covariance plots were similar in SUR2 KO and WT (Figure 2.2D). Collectively, these results indicate that genetic deletion of SUR2 reduces NVC and leads to slower vascular responses following stimulus-evoked neural activity.

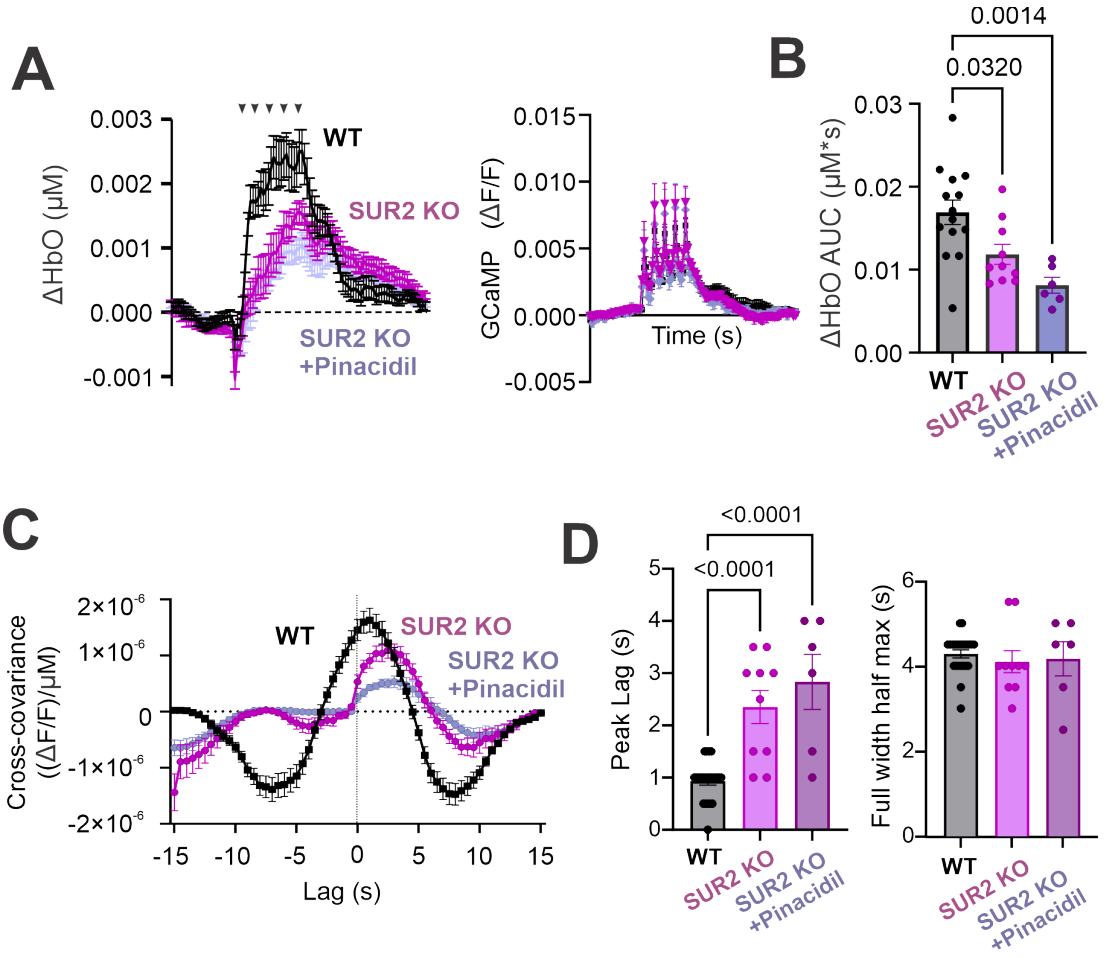

Figure 2.2: Effect of SUR2 KO on neurovascular coupling (A) Mean change (± s.e.m.) of oxygenated hemoglobin (OxyHb, left) and GCaMP (right) signals, measured from ROIs as in Figure 2.1B, in WT and SUR2 KO mice (with or without 0.4 mg/g pinacidil). **(B)** Average (± s.e.m.) AUC of oxygenated hemoglobin signals from experiments in A. **(C)** Cross-covariance calculated from the experiments in A. **(D)** Average (± s.e.m.) delay in OxyHb response following GCaMP signal (peak lag) and full width at half max of peak amplitude.

Similar to treatment with K_{ATP} channel openers such as Pinacidil, Cantú syndrome, resulting from GOF mutations in *ABCC9* or *KCNJ8* [90, 91], is also associated with

various neurological features, including prominently increased risk of migraines [76, 92, 93]. Such effects may be linked to inappropriate blood flow control. In Kir6.1[V65M] mice, which recapitulate multiple key Cantú syndrome features [69, 94], the maximum OxyHb signal was significantly reduced compared to littermate controls (Figure 2.3A,B). As with WT mice, Glibenclamide treatment reduced the maximum OxyHb response for V65M mice, and cross covariance analysis revealed a significant reduction in coupling, with a peak amplitude of $1.5x10^{-6}$ in WT and $9.7x10^{-7}$ in V65M (Figure 2.3C,D). We measured the dose response of Pinacidil on maximal oxygenated hemoglobin in Control and V65M mice. There was a significant (~10-fold) increase in Pinacidil sensitivity in the latter (Figure 2.3E).

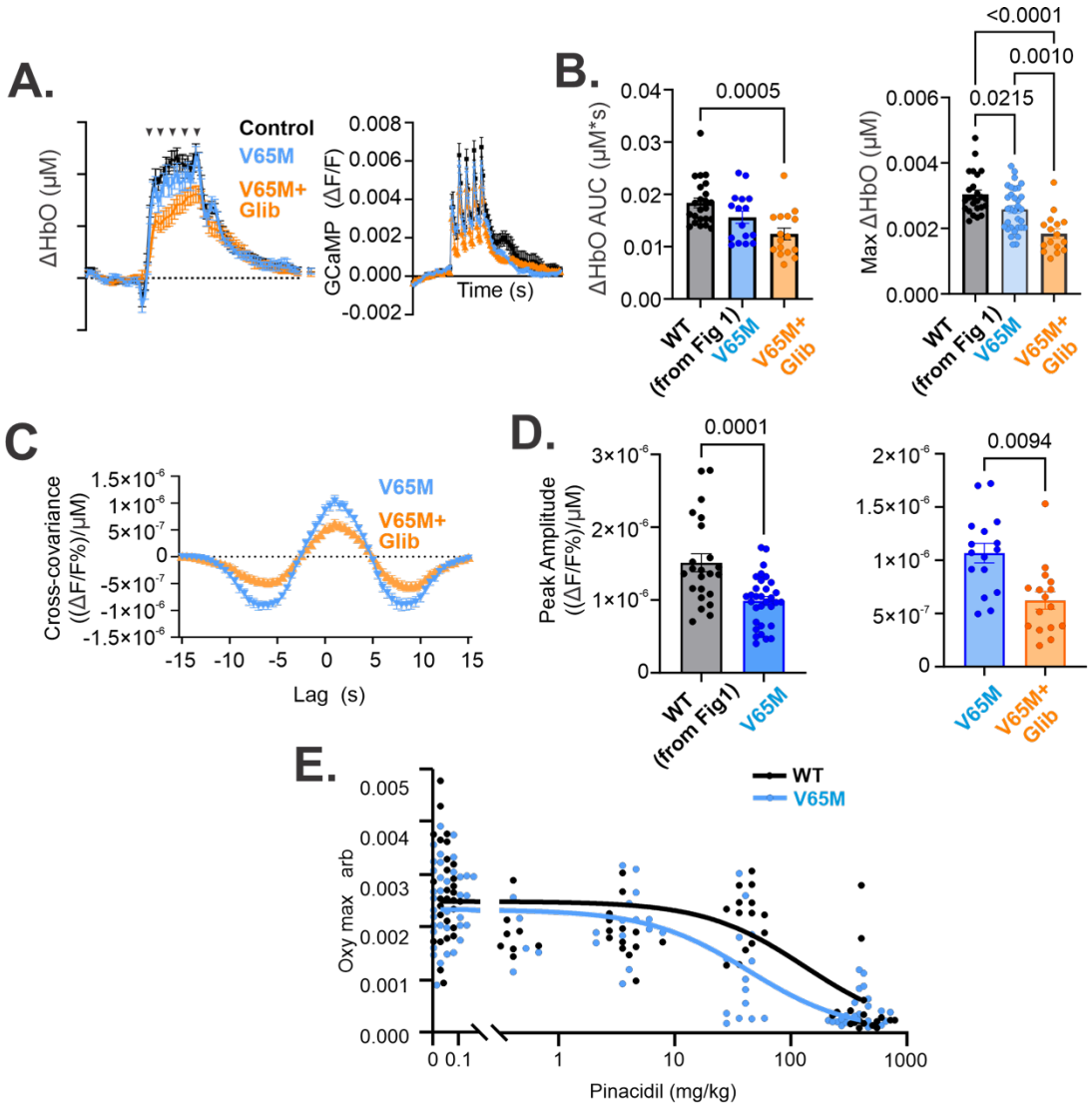

Figure 2.3: Effect of K_{ATP} GOF mutation on neurovascular coupling Mean change (± s.e.m.) of oxygenated hemoglobin (OxyHb, left) and GCaMP, right) signals in WT and Kir6.1[V65M] mice (right) (n=25 hemispheres/13 mice in each case). Control data are from Figure 2.1. **(B)** Average (± s.e.m.) AUC of oxygenated hemoglobin (left) as well as the maximum change in oxygenated hemoglobin (right) signals from experiments in A. **(C)** Cross-covariance calculated from V65M experiments in A. **(D)** Comparison of average (± s.e.m.) peak amplitude of the cross-covariance between WT and V65M (left) as well as a paired comparison between V65M mice before and after Glibenclamide treatment

(left). **(E)** Average (± s.e.m.) maximum change in oxygenated hemoglobin (Oxy max) signals as a function of injected [pinacidil], in WT and Kir6.1[V65M] mice. Mean data at each concentration fit with sigmoidal function, $K_{1/2}$ = 130 mg/kg and 42.72 mg/kg, for WT and V65M, respectively, H fixed at 1 in each case.

2.6 Discussion

2.6.1 Ion channel players in neurovascular coupling

It has long been recognized that neurovascular coupling involves transduction of chemical signals released from active neurons to electrical signals in cells associated with the capillaries to upstream smooth muscle or other contractile cells. These processes lead to relaxation and dilation of the vasculature and subsequent increases in blood flow, volume, and oxygenation. While the underlying mechanisms remain unclear, there appears to be both early contributions from cell-specific vasoactive messaging, and then later responses to signals from by-products of neural activity [42, 84, 95-97]. A well-championed mechanism implicates increased external [K^+], resulting from increased neural activity, causing increased inward rectifier Kir2 channel activity in capillary endothelial cells, which spreads retrograde via gap junctions to hyperpolarize arteriolar smooth muscle [62]. Recent work from several groups has also begun to implicate K_{ATP} channels [64, 73, 74], with demonstration of delayed and reduced neurovascular coupling (NVC) response to whisker stimulation in anesthetized Kir6.1 KO mice [74]. In this study we first utilized multiple pharmacological and genetic manipulations to fully establish that K_{ATP} channels are indeed robust regulators of NVC in awake, conscious animals. Both pharmacological activation and inhibition of K_{ATP} channels reduce NVC, despite the

opposing cellular consequences. This indicates a reliance of NVC on normal K_{ATP} function and suggests that dynamic changes in K_{ATP} activity may be actively involved in controlling the vascular response. Technically, we cannot measure absolute levels of excitability or oxygenation, such that baseline levels may be significantly different in the distinct genetic models, but the complete loss of NVC in Pinacidil-treated mice demonstrates the power of K_{ATP} to maximally dilate the vasculature and obviate any vascular response. By showing that the Pinacidil effect is essentially lost in the genetic absence of K_{ATP}, (i.e. in SUR2-STOP mice), we can confirm that the effect is specifically on K_{ATP}.

2.6.2 Dual mechanisms of K_{ATP} in neurovascular coupling

Both genetic and pharmacologic interventions convincingly demonstrate that either global loss of K_{ATP} activity (glibenclamide or SUR2 KO) or global gain of K_{ATP} activity (pinacidil or Kir6.1[V65M]) both significantly impair neurovascular coupling; with glibenclamide reducing the local rise in oxygenated hemodynamic response to whisker stimulation, and pinacidil completely abolishing it. It is important to note that we are indirectly inferring changes in blood flow from changes in oxygenated hemoglobin and so any absolute change in baseline blood flow is not considered here. Since multiple K channels are present in arteriolar smooth muscle, muscle polarization, and hence contractility, is dependent on overall K conductance [68, 98]. Because of polyamine-dependent rectification [99], Kir2 channels, located in capillary endothelial and smooth muscle cells, exhibit a unique, instantaneous, extracellular [K]-dependence of conductance, such that the membrane potential can hyperpolarize as [K] increases in the

range of 3-8 mM [62]. Recent studies have convincingly demonstrated that conduction of this hyperpolarizing signal to upstream arteriolar smooth muscle via gap junctions, is a primary driver of arteriolar relaxation leading to increased blood flow in neurovascular coupling [62].

2.6.3 Feedback vasculo-neural coupling?

We consistently observed a reduction in GCaMP signals, in both pinacidil- and glibenclamide-treated animals. The underlying cause is unclear, but could relate to an inhibitory consequence of impaired NVC, or potentially to the presence of pinacidil-sensitive K_{ATP} in neurons. However, there is little evidence for ABCC9 expression in cortical neurons [100], and although further study is clearly warranted, we suggest that impaired vascular response may somehow play a role. Although it is recognized that baseline oxygenation in the normal brain is probably sufficient to meet local metabolic demand, it is conceivable that impaired vascular response may cause failure to restore full metabolic support, leading to loss of excitatory currents, or perhaps even activation of neurally expressed Kir6.2/SUR1 K_{ATP} channels [101].

2.6.4 Pathological implications

Cantu Syndrome (CS), characterized by hypertrichosis, cardiomegaly, and multiple other organ issues, is caused by GOF mutations in the genes encoding SUR2 and Kir6.1. Cardiovascular issues include dilated, tortuous blood vessels, physiologically low blood pressure and low systemic vascular resistance, and greatly enlarged hearts with high

cardiac output [90]. CS patients also have tortuous vessels in the cerebral vasculature and a relatively high incidence of migraines as well as several other neurological abnormalities, along with persistent fetal brain blood vessels and enhanced diffuse white matter lesions [69, 76, 77]. The dramatic loss of NVC with the KCO pinacidil, as well as the reduced basal NVC and increased sensitivity to this pinacidil effect in Kir6.1[V65M] mice, suggests that the NVC response may be reduced in patients with CS. There is now mounting evidence that pinacidil and other K channel openers induce or exacerbate migraines in humans [76, 92, 93], supporting the hypothesis that disrupted NVC could underlie the enhanced migraine incidence in CS.

We observed a pronounced slowing and reduction of the NVC response after global knockout of ABCC9 (SUR2) in mice. In contrast to CS, AIMS patients, presumably lacking any SUR2 expression, exhibit significant intellectual disability [75]. Potential LOF *ABCC9* variants are also associated with hippocampal sclerosis of ageing (HSA) [102, 103]. HSA indicates pathologic neural cell loss and gliosis in the hippocampus [104] and is a common Alzheimer's dementia-related disorder, associated with vascular cognitive impairment and dementia [105]. Given the scant evidence for SUR2 expression in anywhere other than vascular cells in the brain [105], we therefore suggest that intellectual disability in AIMS, and dementia in HSA may also be linked to severe loss of NVC.

2.7 Conclusions

Our study comprehensively demonstrates the significant role of Kir6.1/SUR2-dependent K_{ATP} in regulating functional hyperemia in response to neural activity, and shows that either increased or decreased K_{ATP} activity can markedly impair the coupling response. Disrupted NVC, as a result of either increased or decreased K_{ATP} activity, respectively in Cantú syndrome or AIMS, may lead to altered neural activity underlying migraine development or intellectual disability in these conditions.

Chapter 3:

Optical Imaging in

Neurovascular Injury and Repair

3.1 Optical Imaging after Stroke

In Section 1.4 through Chapter 2, I discussed disruptions in neurovascular coupling that exist in several disease states, causing inaccuracy in the estimation of neural activity using hemodynamic signals. In the case of Cantu syndrome, marked disruptions in neurovascular coupling are shown to be caused by the dysfunction of only one ion channel, suggesting severe sensitivity of this neurovascular system to perturbation. One of the most prominent pathologies in which coupling is distinctly altered exists in cerebrovascular disease [106], including stroke. Stroke is the leading cause of chronic disability in the United States [107], and recovery is often unpredictable and incomplete, likely due to the brain's limited capacity for repair [108-115]. Repair after stroke constitutes multiple levels of plasticity, from the remodeling of individual synapses to the restoration of global brain networks, all of which are imperative for functional recovery. Repair at the molecular level constitutes the upregulation and translation of a variety of growth factors to mediate neurogenesis [116-118], axonal spouting [119-122], and angiogenesis [118, 123], like BDNF [124], GDF10 [120], and GAP43 [125, 126]. At the

cellular scale, dendritic spine turnover and mitochondrial trafficking is increased [127-129]. Synaptic scaling via long term potentiation and inhibition is heightened both in regions surrounding the infarct created by stroke, known as peri-infarct regions [130-132], as well as in regions in the contralesional hemisphere [133-135]. These molecular and cellular events set the stage for larger scale remodeling of local circuits and larger brain networks.

Remapping is the apparent migration of function from irreparably damaged regions of the brain to healthy regions caused by synaptic scaling and remodeling after injury [136, 137]. The upregulation of genes that facilitate dendritic arborization [138-142], axonal sprouting [119, 122], and synaptogenesis [121, 126], such as glial derived synaptogenic thrombospondin 1 and 2 [143], CAP23 [125], GAP43 [126], and Arc [144-146], has been demonstrated in stroke-affected circuits undergoing repair, leading to preferential remodeling of these circuits over unaffected circuits. In smaller cortical strokes, remapping is typically observed in peri-infarct cortex [147, 148] and is associated with improved recovery [149], while in larger strokes, the recruitment of distant regions, like those in the contralesional hemisphere (the cortical hemisphere without the infarct), is necessary to aid in remapping [150, 151], which is linked to worsened functional outcomes [152, 153]. Generally, during recovery, it has been shown that lateralization and localization of responses predicts improved recovery, while bilateral activation during task-based activity prognosticates poor outcome [121, 151].

In addition to remapping of local circuits, it's also likely that integration of remapped circuits into functional brain networks is equally important for recovery. Functional connectivity (FC) networks, which are proxy measures of structural global brain networks and were introduced in the previous section, are disrupted after ischemic stroke [154, 155], and their repair is associated with improved functional outcome [156]. In humans, the severity of behavioral deficit after a stroke is strongly correlated to the degree of interhemispheric FC disruption [157, 158]. Rodent stroke experiments have shown striking similarities in the repair patterns of global brain networks across multiple imaging modalities to humans, thus representing an excellent model to study network repair [26, 157, 159].

Given alterations in neurovascular coupling observed in disease states including stroke [41, 50], directly monitoring neural activity is imperative for examining neural repair of both local circuits and global networks after stroke. Wide-field optical imaging in Thy1-GCaMP mice offers a unique method of data capture, which, when employed alongside cranial windowing that permits visualization of the entire dorsal neocortex in mice, allows for the non-invasive, longitudinal measurement of changes in both functional circuits and networks. Spatial and temporal relationships between circuit and network repair are still poorly characterized, as are those between hemodynamic and neural repair after stroke. Longitudinal, simultaneous optical imaging of neural and hemodynamic activity provides an avenue to elucidate some of these relationships between repair at different scales, as well as between neural and vascular remodeling.

3.2 Summary of Findings

In the next chapter, I present a novel stroke experiment aimed at determining early mechanisms and signatures of circuit- and network-level repair that are predictive of long-term behavioral recovery. The study also examines the effects of photothrombotic stroke size, performed in the primary forepaw somatosensory cortex ($S1_{FP}$), on patterns of spatial remapping, network repair, and somatomotor behavioral recovery in Thy1-GCaMP mice. I demonstrate that increasing stroke size, while still only ablating a relatively small cortical volume, causes markedly different patterns of circuit repair, including diffuse spatial remapping and significant changes in temporal dynamics of both affected and unaffected circuits, in addition to changes in stimulus-driven and resting-state connectivity of global brain networks in the early stages of recovery. The repair patterns of mice that received smaller strokes were noticeably different than the patterns observed in mice with larger strokes, and these differences are potentially explained by the degree of injury sustained by the affected somatotopic domain (forepaw domain). Early dynamic changes in spatiotemporal features of circuit and network function predicted long-term behavioral outcome in mice, independent of infarct size. These findings may help to further understand adaptive patterns of repair, as well as to identify targets for therapeutic intervention in cases of maladaptive repair.

Chapter 4:

Early Changes in Spatiotemporal Dynamics of Remapped Circuits and Global Networks Predict Functional Recovery after Focal Ischemia in Mice

4.1 Abstract

Recovery from stroke is often incomplete and unpredictable. Both remapping of damaged local circuits and repair of disrupted global brain networks after stroke have been shown to herald improved outcomes, but the spatiotemporal characteristics of these two levels of repair that explain and predict recovery are poorly understood. We used wide-field optical calcium imaging in Thy1-GCaMP mice to map changes in local circuits and global networks, and to investigate patterns of population- and network-level neuronal dynamics that predict functional recovery after focal photothrombotic stroke of varying size centered in the primary forepaw somatosensory cortex ($S1_{FP}$). We show that larger strokes with complete ablation of $S1_{FP}$ cause diffuse and widespread forepaw stimulus-evoked cortical activation, including contralesional regions. Larger strokes also

decreased neuronal fidelity and bilateral coherence during stimulation of both affected and unaffected forepaws, individually. Finally, larger strokes induced hyperconnectivity within the contralesional hemisphere. We also demonstrate that the degree of each of these metrics predicts longer term behavioral recovery better than infarct volume alone. These findings may shed light on early changes in cortical neuronal dynamics that predict longer term recovery and outcomes after stroke.

4.2 Introduction

Stroke is one of the leading causes of chronic disability in the United States, affecting more than 795,000 people annually and costing $56.5 billion in direct and indirect costs [107]. Recovery from stroke is spontaneous, but often incomplete, aided by rehabilitative therapies to regain affected functional ability [108-115]. Identifying early predictive neuroimaging biomarkers may not only be helpful for prognostic purposes, but may also reveal early brain repair mechanisms that are important for behavioral recovery. While adaptive patterns of functional brain activity that predict stroke recovery are important, equally important are maladaptive patterns of activity in populations of neurons, which can point to targets for therapeutic intervention. Remapping of affected function has been explored after stroke recovery, and its correlation with functional outcome is seemingly spatially dependent, with perilesional remapping being strongly associated with improved behavioral recovery [153, 160, 161], and distant/diffuse remapping being associated with poorer outcomes [162-164]. Distant remapping into functionally related cortical regions (as seen in bilateral activation) is generally observed

in animal models of large stroke, such as middle cerebral artery occlusion (MCAO) [151]. Similar findings have been noted in human stroke, where fMRI has shown bilateral, diffuse task-based activation after stroke [108, 153]. However, little is known about the threshold of stroke size that results in distant/diffuse remapping. Furthermore, while deficits in function of limbs ipsilateral to stroke have been documented [165-167], changes that occur in unaffected circuits into which affected functions remap when distant remapping occurs are also poorly understood. Meso- and macroscopic characteristics of remapping that may be predictive of stroke recovery, and whether these characteristics are independent of the initial degree of injury, are yet to be explored.

In addition to remapping, it is likely that the integration of remapped functional circuits into global brain networks is also necessary for favorable recovery. Synchrony of spontaneous neuronal activity across the cortex can be parsed into distinct functional networks that are consistent across and within subjects [168, 169]. Normalization of these global neuronal networks, which are disrupted after focal ischemic stroke [25, 26, 155], has also been associated with functional improvement after stroke [26, 27, 156]. Still, how the extent of injury to a somatotopic domain affects global functional network changes and how these functional network changes may prognosticate recovery after stroke remain unknown. Moreover, integration of affected remapped circuits into these global functional networks, and how changes in affected circuits influence functionally-related but uninjured circuits, is still poorly understood.

Here, we used a variable-sized photothrombotic stroke model that targets the right primary forepaw somatosensory cortex ($S1_{FP}$) to produce partial or complete ablation in conjunction with wide-field calcium imaging in transgenic Thy1-GCaMP mice to examine the effects of infarct size and degree of injury sustained in $S1_{FP}$ (partial vs. complete ablation) on remapping, functional network repair, network dynamics, and behavioral recovery. Forepaw somatosensory cortex was used due to its well-characterized nature and extensive battery of reliable functional assays available. Longitudinal wide-field calcium imaging permitted the monitoring of changes in both local circuits and global brain networks, allowing for the contextualization of multiple scales of repair. Our results indicate that larger infarct sizes (completely ablating $S1_{FP}$) cause diffuse, bilateral remapping of affected, and in some cases unaffected, thalamocortical circuits. Subsequent to diffuse remapping, we observed the development of hyperconnectivity within functional networks of abnormal topography, and significant decreases in neuronal fidelity and bilateral coherence during stimulation of both affected and unaffected forepaws after larger photothrombotic stroke. All these measures were independently predictive of worsened functional outcome after stroke, suggesting that the patterns of remapping and network changes were maladaptive. In contrast, a slightly smaller infarct (partially ablating $S1_{FP}$) resulted in remapping of affected paw function within the original $S1_{FP}$, no remapping of unaffected paw function, normal functional connectivity topologies, and less severe decreases in neuronal fidelity during affected paw stimulation, predicting better behavioral recovery.

4.3 Methods

4.3.1 Study design

The two primary goals of this study were: 1. To examine the impact of stroke size on remapping, network repair, network dynamics, and behavioral recovery, and 2. To investigate multiscale patterns of circuit/network repair that predict behavioral recovery. To accomplish the first goal, mice were administered photothrombotic stroke with a laser spot diameter of either 1 or 2 mm centered in right forepaw somatosensory cortex to achieve partial or complete ablation of $S1_{FP}$, respectively. To examine changes in neuronal dynamics to predict behavioral recovery, mice were only imaged before stroke, and 1 and 4 weeks after stroke, while behavioral assays were performed before stroke, and 1 and 8 weeks after stroke. Mice were imaged infrequently to avoid negative effects of repeated anesthetic exposure. Behavioral assays were performed infrequently to prevent learning effects due to repeated testing. Importantly, behavioral recovery was measured as the change in forepaw asymmetry from Week 1 to Week 8, providing a measure of maximum deficit to final deficit at 8 weeks (recovery). An illustration of the study design is provided in Figure 4.1.

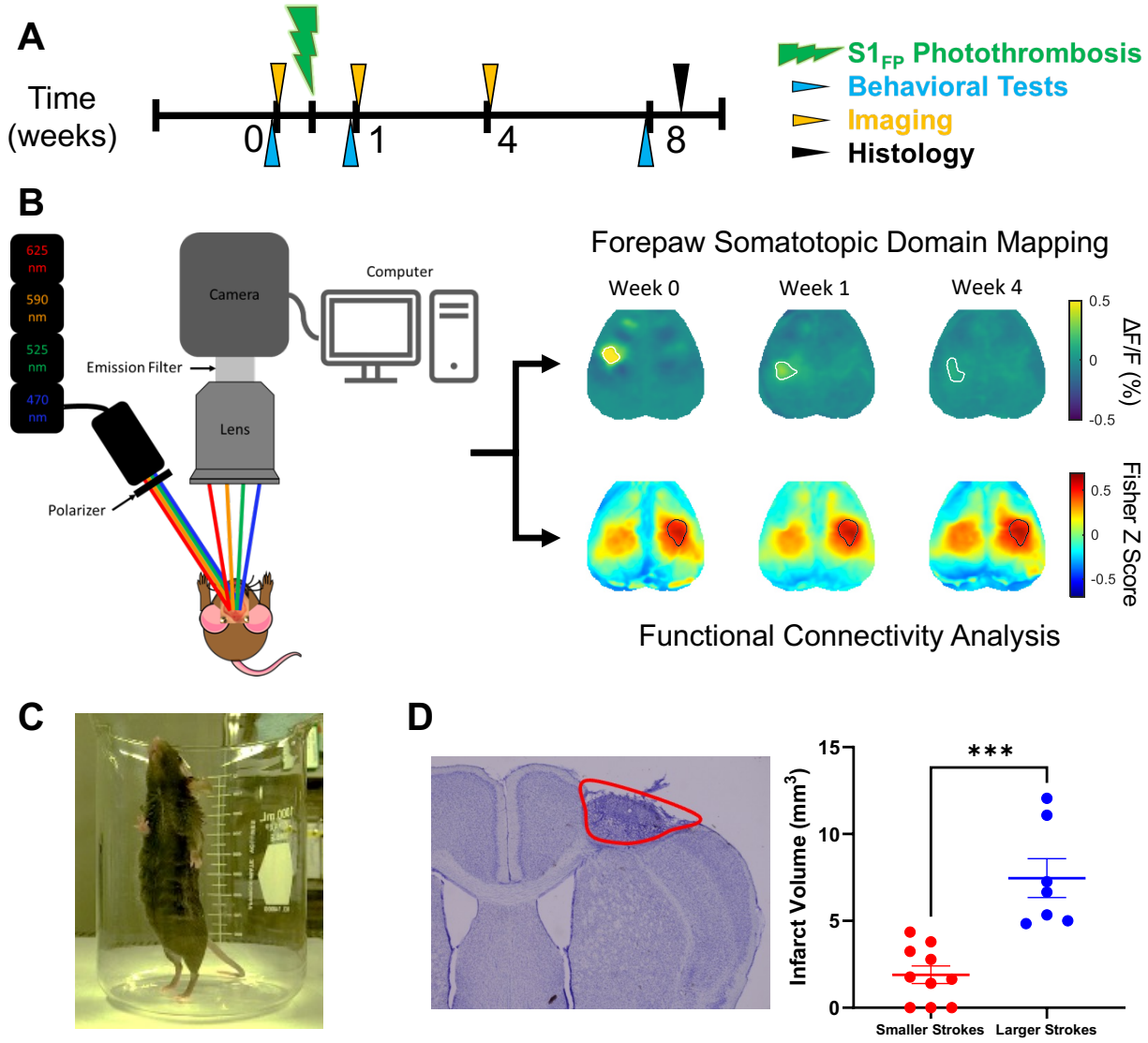

Figure 4.1: Experimental design to predict long-term stroke recovery using early patterns of repair. (A), A timeline of our experiment is provided showing imaging, behavioral testing, photothrombosis, and histological analysis timepoints. The timeline is given in weeks, where mice were 12 weeks old at time t = 0. (B), A diagram of the optical imaging rig used to perform widefield optical imaging on mice (left). Imaging for forepaw somatotopic domain mapping was performed while mice received anesthetized electrical forepaw stimulation, while imaging for functional connectivity analyses was performed on awake, resting-state mice. Example maps of each imaging and analysis paradigm are shown for an individual mouse during each imaging timepoint in the 3 panels on the right. (C), Somatomotor function was quantified using the cylinder rearing assay. (D), Infarct volume quantification was performed using Cresyl violet staining; an example image is

shown on the left. Histological infarct volumes were significantly larger ($p = 0.0002$) in the larger stroke group (n = 7 mice) compared to the smaller stroke group (n = 10 mice).

4.3.2 Mice and procedures

Mouse model: All methods below were performed in accordance with Washington University Animal Studies Committee policy in agreement with the American Association for Accreditation of Laboratory Animal Care guidelines. Mice raised in enriched housing (as previously described, [170]) to increase dynamic range of recovery following stroke were given ad libitum food and water with a 12 hour - 12 hour light-dark cycle. The studies described used 12-week-old hemizygous Thy1-GCaMP6f mice on a C57-BL6J background [14]. Mouse genotype was confirmed using PCR: forward primer 5′-CATCAGTGCAGCAGAGCTTC-3′ and reverse primer 5′-CAGCGTATCCACATAGCGTA-3′.

Cranial windows for optical imaging: Cranial windows were prepared on the dorsal cranium of each mouse as previously described [171]. Mice were anesthetized with isoflurane (induction 3-5%, maintenance 1-2%), and head-fixed in a stereotaxic frame. Body temperature was maintained using a feedback-controlled heating pad. The scalp was shaven and sterilized, and then incised and retracted along midline. Metabond dental cement (C&B Metabond, Parkell Inc.) was used to adhere a custom Plexiglas window to the mouse's cranium, completely covering the surgical site. 5 days of recovery were allotted before any behavioral or imaging tests were performed.

Photothrombosis: Photothrombosis was performed as previously described [172]. Mice were administered Rose Bengal via IP injection. A 523-nm diode pumped solid state laser illuminated right forepaw somatosensory cortex (-2.2 bregma, 0.5 lambda) for 10 minutes. Mice receiving small strokes had laser diameters of 1 mm, while mice receiving large strokes had 2 mm laser diameters. Imaging and behavioral tests were not performed for a week following stroke.

Behavioral assays: After stroke to $S1_{FP}$, mice are known to exhibit asymmetric forepaw use favoring the unaffected limb during the cylinder rearing assay, which then typically become more symmetric as the mouse recovers [172, 173]. Mice were recorded while performing exploratory rearing behavior for 10 minutes. The number of frames that each forepaw contacted the wall of the cylinder in the video was recorded and used to calculate forepaw asymmetry using the equation Asymmetry = (Left - Right)/(Left + Right + Both), as previously described (Figure 4.1C) [172]. Recovery was defined as any improvement in asymmetry of the affected paw (greater use of the affected paw) from Week 1 to Week 8, while deficit was defined as decline in asymmetry of the affected paw (greater use of the unaffected paw).

Infarct volume quantification: Infarct volumes were quantified as previously described [174]. Mice were deeply anesthetized with pentobarbital and perfused with heparinized phosphate-buffered saline solution. Brains were harvested, frozen on a sliding microtome, and sliced in 40-micron coronal sections. Each successive slice containing

infarcted tissue was mounted and stained with cresyl violet. Brightfield images of stained slices were taken using a Keyence BZ-X800 microscope. Cross sectional area of infarcted tissue on each slice was determined by blind experimenters using ImageJ. Areas were summed and multiplied by the slice thickness to obtain infarct volumes for each mouse (Figure 4.1D).

4.3.3 Wide-field optical imaging recordings

Wide-field optical imaging: Cortical calcium and hemoglobin activity were measured using wide-field optical imaging, as previously described [171]. Sequential illumination of the dorsal neocortex was performed using four LEDs of wavelengths 470 nm, 525 nm, 605 nm, and 625 nm. GCaMP was excited with the 470 nm LED, while multispectral hemodynamic imaging was performed using the remainder of the LEDs. Multiwavelength dichroic beam combiners for LED collimator sources at 480, 560, 585, and 605 nm (LCS-BC25-0480, LCS-BC25-0560, LCS-BC25-0585, LCS-BC25-0605, Mightex Systems) were used to collimate and combined all LED beams. A cooled, sCMOS camera (Zyla 5.5-USB3, Andor) with a 75-mm f/1.8 camera lens and 80 Hz acquisition framerate (20 Hz acquisition rate for each channel) was used for image detection.

Optical imaging recordings: Optical imaging recordings were performed as described previously [174]. Resting state image recordings (Figure 4.1B, bottom) for functional connectivity processing were performed while mice were awake; forepaw evoked response imaging recordings (Figure 4.1B, top) were performed while mice were

anesthetized with a ketamine-xylazine cocktail (100 mg/kg ketamine, 10 mg/kg xylazine). Body temperature was maintained as described above. Forepaw stimulation was performed on each paw for 5 minutes using computer controlled, 1 mA electric pulses delivered via microvascular clips (Roboz) attached to either side of the forepaw [174]. Stimulation was administered in a block design (5 s rest; 5 s of 3 Hz, 1 mA, 0.3 ms pulses; 10 s rest; 15 blocks/5 minutes recording). Imaging was performed before stroke, and 1 and 4 weeks after stroke.

4.3.4 Optical imaging processing and analyses

Optical imaging signal processing: Binary brain masks were created for each mouse, and all analyses that followed were performed only on brain pixels. Brain masks and image sequences of brain pixels were affine transformed to Paxinos atlas space using cranial landmarks. A matrix of the mean of 5 seconds of baseline light levels with no LED illumination was subtracted from all raw data. Stimulation runs underwent baseline subtraction [174], and then spatial and temporal detrending was then performed on all brain pixel time traces as previously described [2]. Oximetric changes were quantified [21], and hemoglobin confound was removed from the GCaMP signal, as previously described [175]. Global signal regression was performed on all brain pixels to expose the topography of functional networks. Imaging runs containing motion artifact, which were detected by thresholding light levels [171], were excluded from analyses.

Evoked response analysis: Regions of interest (ROIs) were defined for forepaw somatosensory cortex by thresholding individual and group-averaged forepaw evoked responses, averaged across blocks and peaks for GCaMP ROIs at 50% of the maximum pixel intensity of the peak-averaged response map at each timepoint for each paw. Evoked response maps displayed show group-, block-, and peak-averaged fluorescence signals following each of 15 3-Hz electrical pulses. Individual areas of activation were obtained by counting the number of pixels in individual GCaMP ROIs and converting units to mm^2 (the length of one side of a pixel was equal to 78 microns). Amplitude-area products were calculated by multiplying an individual mouse's area of activation by the summed fluorescence contained in that area. Mice whose maximum GCaMP response amplitude was less than 10% of their baseline maximum value were excluded from analyses.

Power and fidelity analyses: Fast Fourier transforms (FFTs, native fft() function in MATLAB) were performed as previously described [171] on block-averaged stimulation runs during both affected and unaffected paw stimulation. 3 Hz power maps were created by finding group-averaged evoked response power at 3 Hz. Individual ipsilesional and contralesional fidelity values were calculated as previously described [171].

Magnitude-squared coherence analysis: Magnitude-squared coherence maps were generated by calculating magnitude squared coherence (native mscohere() function in MATLAB) between activity in an individual mouse's unaffected paw evoked response ROI

(see above, Evoked Response Analysis) and the activity of every other pixel in the brain space. Individual magnitude-squared coherence values were determined by calculating magnitude-squared coherence between an individual mouse's average activity in the unaffected paw evoked response ROI and affected paw evoked response ROI.

Functional connectivity analysis: Functional connectivity analyses were performed as previously described [171]. Pre-processed resting state data was filtered for a desired frequency range (infraslow: 0.1 – 1 Hz, delta: 1 – 4 Hz, and theta: 4 – 7 Hz). The GCaMP fluorescence time signal within an ROI (also referred to as a seed) was averaged and correlated to the fluorescence time signal of every pixel in the brain space for a given mouse and Pearson z-correlations were plotted on maps at each week to show longitudinal functional network changes. Individual evoked response ROIs from unaffected paw stimulation at specific time points were used for the calculation of seed-based functional connectivity measures including node degree. Node degree was calculated by counting the number of pixels in the brain space that had a Pearson z-correlation of at least 0.4.

Optical imaging infarct size quantification: Quantification of infarct size in optical imaging recordings was optimized by comparing several functional connectivity measures. Homotopy maps were calculated by filtering resting state recordings into one of the desired frequency bands listed in the Functional Connectivity section above, and finding Pearson z-correlations of pixels reflected across the midline from one another (mirror

image pixels). Pearson z-correlations of homotopy maps calculated 1 week after stroke (Week 1) were divided by the analogous Pearson z-correlations of homotopy maps at baseline (Week 0) to obtain ratio homotopy maps. Ratio homotopy maps were then binarized by a threshold of 0.2 and the largest contiguous region in the binarized map was taken as the infarct ROI. Ratio integrated power ROIs were obtained by calculating the ratio of integrated power (0.1-8 Hz) in each pixel at Week 1 compared to Week 0, and thresholding the resulting map for values less than 0.2. Seed-based functional connectivity maps were created as described in the Functional Connectivity section above, and ratio seed-based FC maps were calculated in the same ratiometric way homotopy maps were. Different thresholds were used to determine infarct sizes using the ratio seed-based FC maps, and are displayed in their respective plots.

4.3.5 Statistical analyses

Statistical analysis: All statistical analyses, excluding mediation analyses delineated below, were performed using GraphPad Prism 10.1. Statistical differences in longitudinal optical imaging measures were calculated using two-way repeated measures ANOVA tests. Post-hoc Dunnett's tests for multiple comparisons were performed to compare each group's mean values at Weeks 1 and 4 with its mean pre-stroke value. Linear regressions to predict functional recovery using optical imaging measures were performed using the linear regression analysis function in GraphPad Prism. The threshold for statistical significance was set at $p = 0.05$ for all analyses.

Statistical mediation analysis: Statistical mediation analyses were conducted in R v4.3.0 [176]. Data were visually inspected for univariate and multivariate outliers prior to statistical modeling, none were found, and residuals from the linear models were inspected for normality, homoscedasticity and influential data points [177]. Mediation was tested through a series of linear models [178, 179]:

Model 1: $Y_i \sim c(X_i) + \epsilon_i$ (where Y is the outcome of interest)

Model 2: $M_i \sim a(X_i) + \epsilon_i$ (where M is the mediator of interest)

Model 3: $Y_i \sim b(M_i) + c'(X_i) + \epsilon_i$

These models are diagramed in tripartite figures shown in Figure 4.S3. Across models, the outcome of interest (Y) was always behavioral recovery, defined as the change in forepaw asymmetry during exploratory rearing in the cylinder rearing assay from Week 1 to Week 8. X and M were different histological or neuroimaging variables (detailed below), but these variables were always collected earlier (from Week 1 to Week 4), so all variables temporally precede recovery. Coefficient *c* reflects the unadjusted relationship between Y~X. Coefficient *a* reflects the unadjusted relationship between M~X. Coefficient b is the effect of M on Y, controlling for X, and coefficient *c'* is the effect X on Y controlling for M.

Model 1 is useful for seeing the unadjusted relationship between recovery and a candidate predictor. This path, c, is referred to as the *total effect*, but is not a formal part of the mediation. Instead, the mediation focuses on Models 2 and 3 to understand the potential path through the mediator, i.e., X → M → Y, which is referred to as the *indirect*

effect. And any remaining *direct effect* of X on Y after controlling for M, i.e., X → Y. Statistical significance for the mediation effects was based on nonparametric bootstrap estimate of the standard error (n=1000 iterations) [179].

4.4 Results

4.4.1 Variance in photothrombotic infarct size

Mice were subjected to photothrombotic strokes of two sizes by varying laser diameter (1 vs. 2 mm). Infarct size was significantly different between the two groups (smaller strokes: 1.899 ± 1.610 mm^3; larger strokes: 7.462 ± 2.954 mm^3; p = 0.0002) (Figure 4.1D). However, 7 of 28 mice died during the course of this study. 1 mouse died before stroke administration, while the other 6 mice died during week 1 or week 4 imaging, likely due to repeated anesthesia. Lesion volumes were therefore missing for these mice. To obtain a reliable imaging proxy for final infarct volume, we tested a 1-week imaging measure: delta-range homotopy maps (functional connectivity maps of mirror-image pixels across the midline), termed delta homotopy infarct maps, as described in methods (Figure 4.2A). Incidence maps for delta homotopy infarcts for each group are shown in Figure 4.2B. Delta homotopy size was significantly correlated to histological infarct volume (R^2 = 0.5921, p = 0.0003; Figure 4.2C) in those mice that had both measurements. We also tested imaging metrics of theta homotopy infarct maps, integrated power ratio, and contralesional $S1_{FP}$-seed-based functional connectivity ratio maps in the delta and theta bands (Figure 4.S1D-G), but none were as strongly correlated to histological lesion

volume as delta homotopy infarct maps. In subsequent results, we use delta homotopy infarcts as a proxy for final infarct volume for regression analyses.

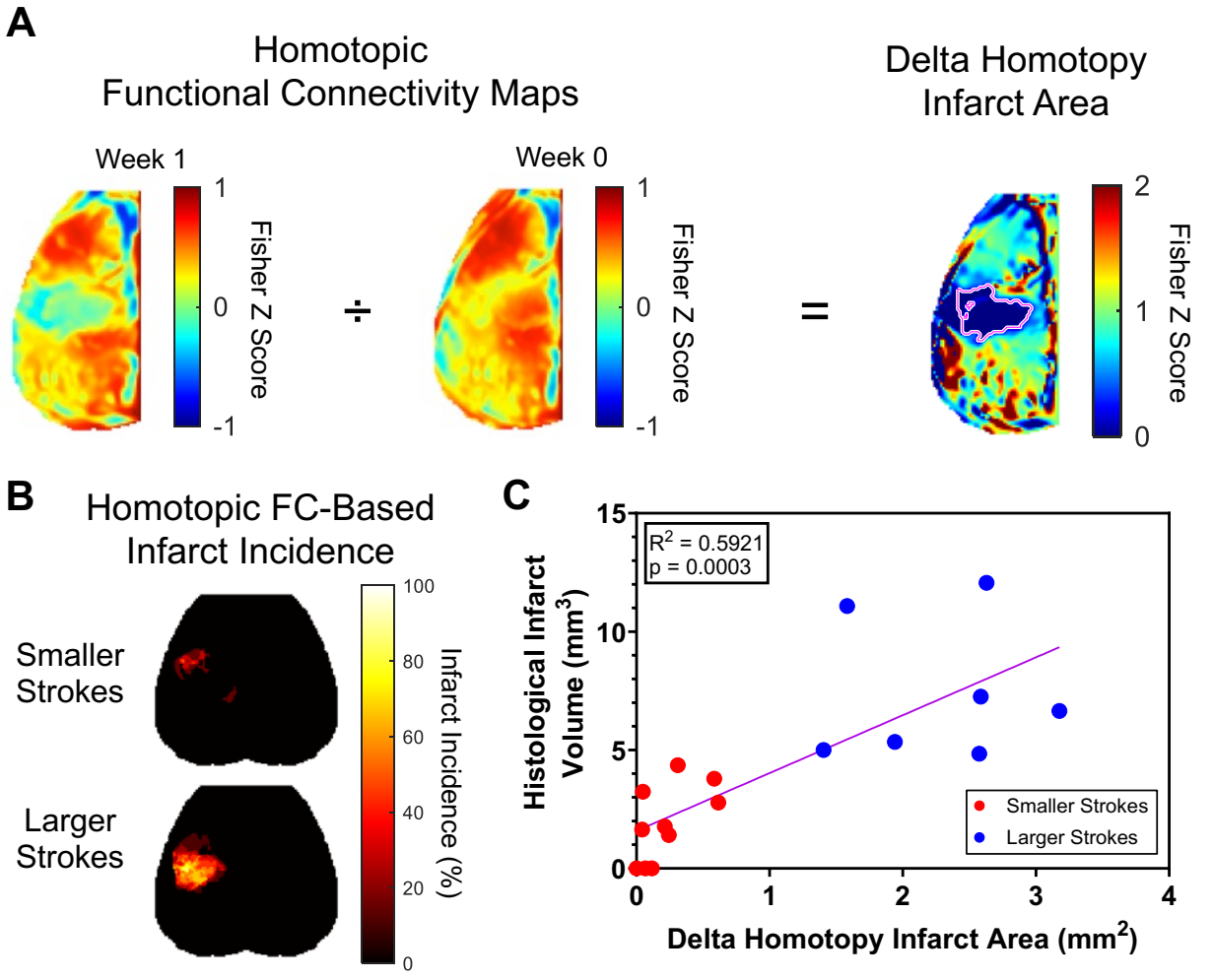

Figure 4.2: Quantification of infarct size using optical imaging is a reliable proxy of histological infarct volume. (A), Fisher Z scores of Week 1 homotopic delta (1-4 Hz) FC maps (left) were divided by Z scores of analogous pixels at baseline (middle) to obtain homotopic functional connectivity ratio maps (right). Values 0.2 or lower were classified as delta homotopy infarct areas for each mouse. (B), Incidence maps showing proportions of mice with infarcted tissue across the cortex. (C), Delta homotopy infarct areas at Week 1 were plotted against Week 8 histological infarct volumes (n = 17 mice). R^2 and p values are displayed on the plot.

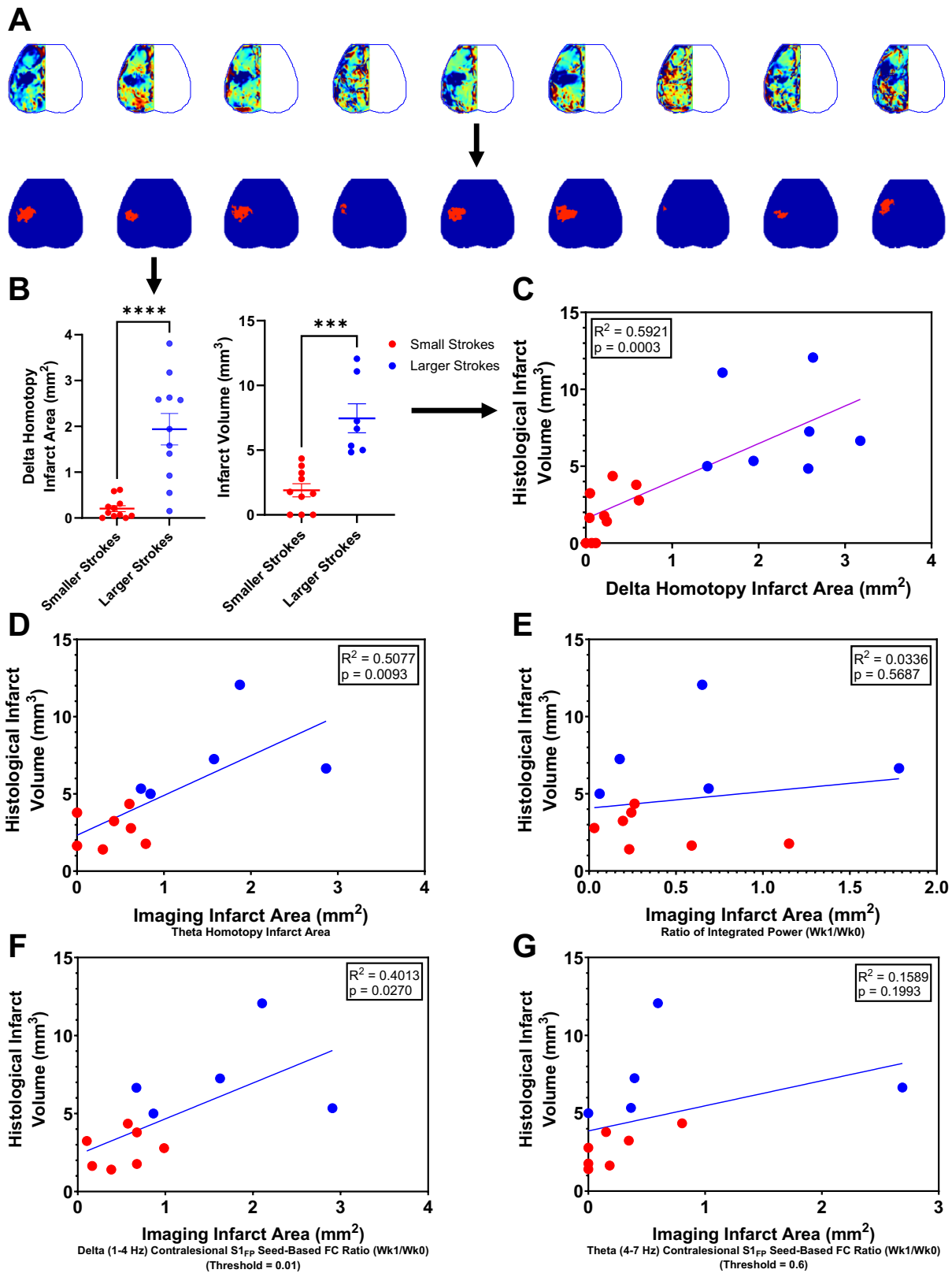
A
B
C
D
E
F
G
****
***
Delta Homotopy Infarct Area (mm²)
Infarct Volume (mm³)
Smaller Strokes
Larger Strokes
Small Strokes
Larger Strokes
Histological Infarct Volume (mm³)
R² = 0.5921
p = 0.0003
Delta Homotopy Infarct Area (mm²)
R² = 0.5077
p = 0.0093
Imaging Infarct Area (mm²)
Theta Homotopy Infarct Area
R² = 0.0336
p = 0.5687
Ratio of Integrated Power (Wk1/Wk0)
R² = 0.4013
p = 0.0270
Delta (1-4 Hz) Contralesional S1FP Seed-Based FC Ratio (Wk1/Wk0)
(Threshold = 0.01)
R² = 0.1589
p = 0.1993
Theta (4-7 Hz) Contralesional S1FP Seed-Based FC Ratio (Wk1/Wk0)
(Threshold = 0.6)

Figure 4.S1: Multiple Week 1 imaging measures predict histological infarct size at Week 8. (A), Individual delta homotopy infarct area maps (top) are shown for select mice in the larger stroke group, and binarized to obtain infarct ROIs (bottom). (B), Both delta homotopy infarct size ($p < 0.0001$) and histological infarct volume ($p = 0.0002$) of mice with larger strokes were significantly greater than the analogous measures for mice with smaller strokes. (C), Individual delta homotopy infarct areas are plotted against individual histological infarct volumes. (D), Individual theta (4-7 Hz) homotopy infarct areas are plotted against individual histological infarct volumes. (E), Individual areas of infarcts, obtained by applying a threshold to the pixel-wise ratio of integrated cortical GCaMP fluorescence power (0.01 – 7 Hz) from Week 0 to Week 1 at 0.2, are plotted against individual histological infarct volumes. (F), Individual infarct areas, obtained by applying a threshold to pixel-wise ratio of seed-based delta FC from Week 0 to Week 1 at 0.01, are plotted against individual histological infarct volumes. (G), Individual infarct areas, obtained by applying a threshold to the pixel-wise ratio of seed-based theta FC from Week 0 to Week 1 at 0.6, are plotted against individual histological infarct volumes. R_2 and p-values are displayed on each plot.

4.4.2 Altering $S1_{FP}$ stroke size elicits markedly different remapping patterns

To examine how infarct size influences remapping and behavioral recovery, we administered photothrombotic stroke of varying sizes centered in $S1_{FP}$ and performed wide-field calcium imaging during peripheral forepaw stimulation 1 and 4 weeks after stroke (Figure 4.1A,B). GCaMP fluorescence is strongly associated with population-level neuronal activity [180], providing a mesoscopic view of cortical neuronal activity. Mice show attenuation of stimulus-evoked GCaMP fluorescence after stroke (Figure 4.S1), leading to diffuse responses. Thresholding at consistent values across timepoints therefore poses a problem when using area of activation during stimulation as a metric of remapping (i.e. areas of activation will be greater due to lower GCaMP fluorescence maxima after stroke and may not reflect remapped circuits). Therefore, we used the product of area of activation and the summed fluorescence contained within that area as

a metric of remapping that includes information concerning both amplitude and area of a stimulus-evoked response, which we have termed amplitude-area. Representative group-averaged fluorescence maps during stimulation at each time point for each group are shown in Figure 4.3A. One week after stroke, mice that received smaller strokes demonstrated remapping within or near the original $S1_{FP}$, but did not demonstrate any significant changes in the amplitude-areas of their responses (Figure 4.3A,C,D). However, mice with larger strokes were observed to have bilateral and diffuse remapping, with significantly lower amplitude-areas of activation in the ipsilesional hemisphere (Figure 4.3C), and significantly greater amplitude-areas of activation in the contralesional hemisphere (Figure 4.3D) at Week 4 compared to Week 0. Surprisingly, there was only a small difference in infarct size that resulted in contralesional activation. Mice whose infarct sizes were greater than or equal to 1 mm^2 demonstrated contralesional activation, while mice with infarct volumes less than or equal to 0.8 mm^2) did not demonstrate contralesional activation. Indeed, it appeared that a threshold infarct size anywhere from 0.8-1.0 mm^2 triggered contralesional activation.

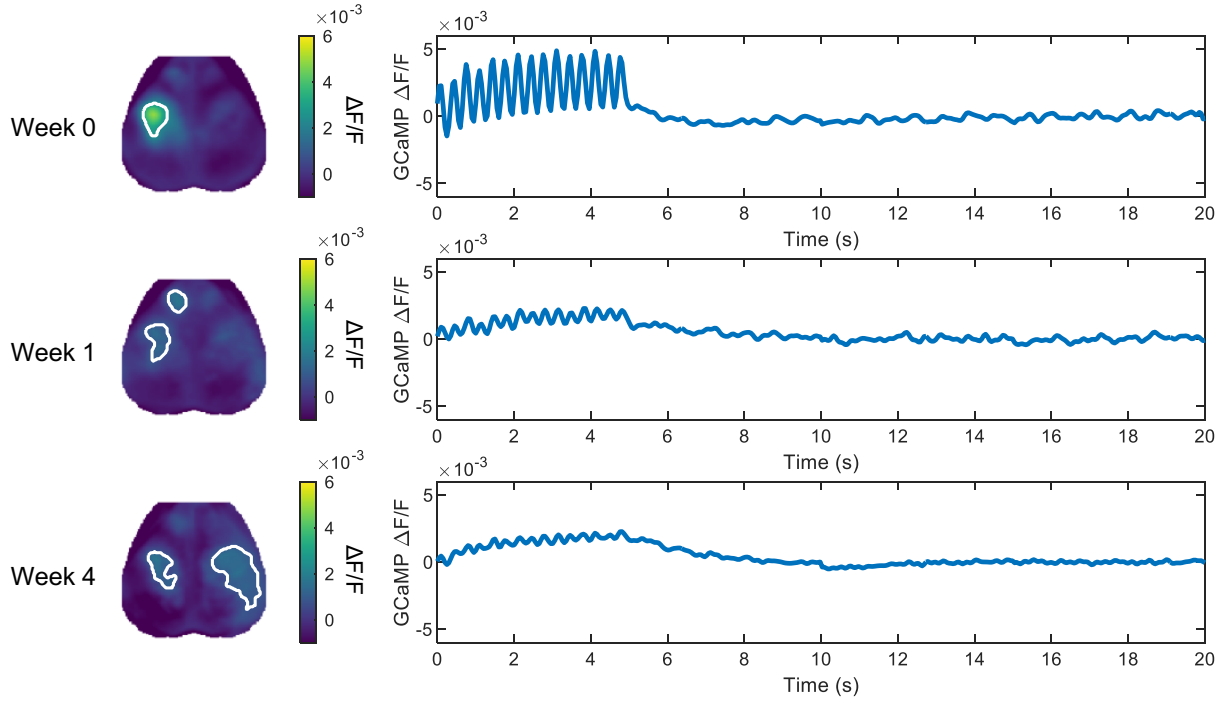

Figure 4.S2: Stimulus-evoked GCaMP fluorescence is markedly attenuated after stroke in mice. Group-averaged, block-averaged, and peak-averaged GCaMP fluorescence maps (left) during affected forepaw stimulation are shown at each timepoint for mice that received larger strokes. To the right of each map is a group-averaged, block-averaged, ROI-averaged (outlined in white in the maps) trace of GCaMP activity during affected paw stimulation during that timepoint. Time traces of GCaMP fluorescence activity show stimulation from time t = 0 to t = 5 seconds.

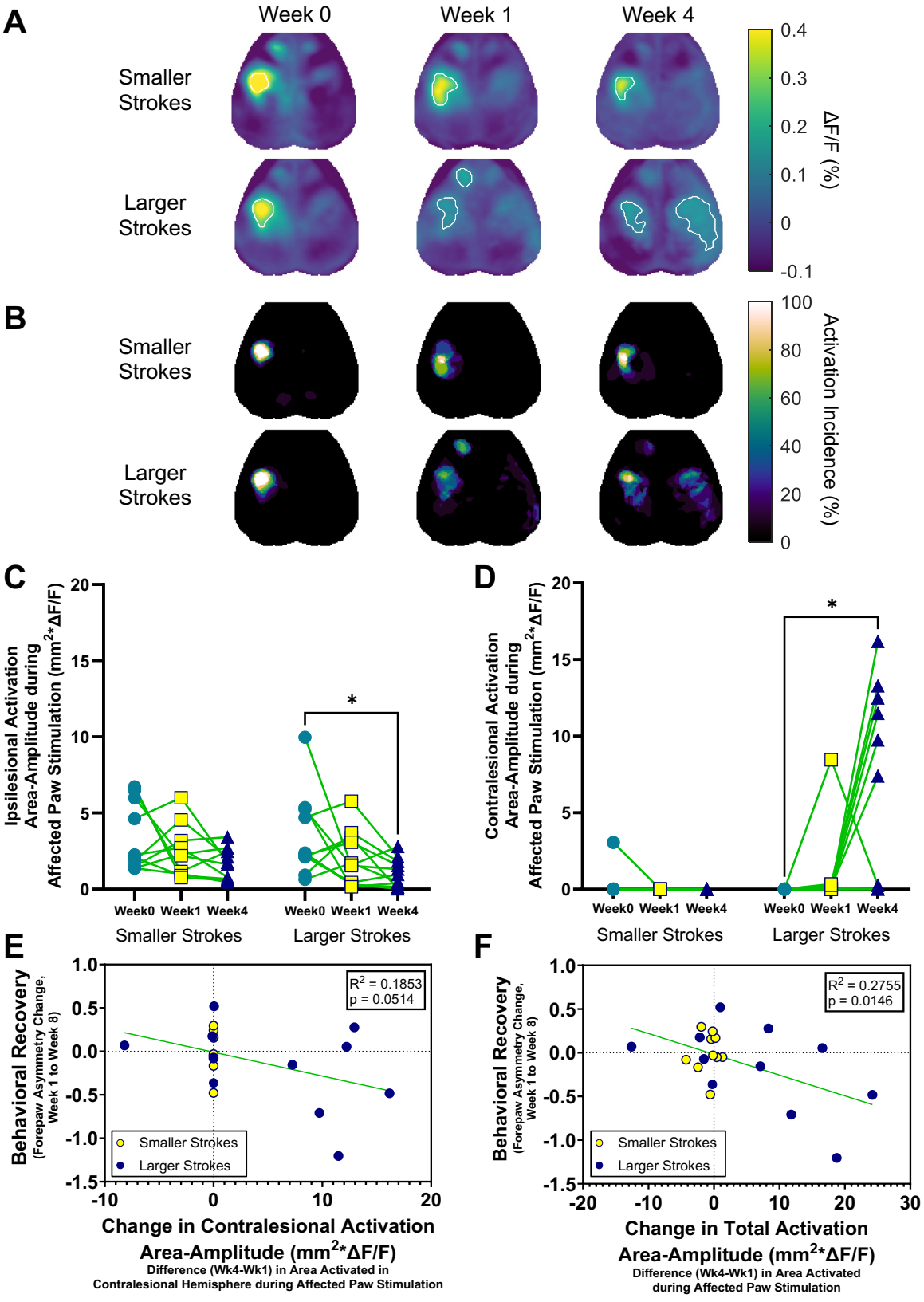
A
Week 0
Week 1
Week 4
Smaller Strokes
Larger Strokes
0.4
0.3
0.2
0.1
0
-0.1
ΔF/F (%)
B
Smaller Strokes
Larger Strokes
100
80
60
40
20
0
Activation Incidence (%)
C
Ipsilesional Activation Area-Amplitude during Affected Paw Stimulation (mm2*ΔF/F)
20
15
10
5
0
*
Week0 Week1 Week4
Week0 Week1 Week4
Smaller Strokes
Larger Strokes
D
Contralesional Activation Area-Amplitude during Affected Paw Stimulation (mm2*ΔF/F)
20
15
10
5
0
*
Week0 Week1 Week4
Week0 Week1 Week4
Smaller Strokes
Larger Strokes
E
Behavioral Recovery
(Forepaw Asymmetry Change, Week 1 to Week 8)
1.0
0.5
0.0
-0.5
-1.0
-1.5
R2 = 0.1853
p = 0.0514
Smaller Strokes
Larger Strokes
-10
0
10
20
Change in Contralesional Activation Area-Amplitude (mm2*ΔF/F)
Difference (Wk4-Wk1) in Area Activated in Contralesional Hemisphere during Affected Paw Stimulation
F
Behavioral Recovery
(Forepaw Asymmetry Change, Week 1 to Week 8)
1.0
0.5
0.0
-0.5
-1.0
-1.5
R2 = 0.2755
p = 0.0146
Smaller Strokes
Larger Strokes
-20
-10
0
10
20
30
Change in Total Activation Area-Amplitude (mm2*ΔF/F)
Difference (Wk4-Wk1) in Area Activated during Affected Paw Stimulation

Figure 4.3: Altering $S1_{FP}$ stroke size elicits differential changes in early spatial remapping patterns of affected paw circuits. (A), Group-averaged, block-averaged, and peak-averaged GCaMP fluorescence maps during affected forepaw stimulation are shown at each timepoint for each group. (B), Incidence maps of individual areas of activation during affected paw stimulation are shown at each timepoint for each group. (C-D), Areas of activation in the ipsilesional (C) and contralesional (D) hemispheres from (B) were multiplied by the summed fluorescence contained in those areas to obtain amplitude-area measures of activation for each mouse. Individual area-amplitudes in each hemisphere are plotted in spaghetti plots for each group (smaller strokes: n =10 mice; larger strokes: n = 11 mice). Two-way ANOVA tests with Dunnett's tests for multiple comparisons were performed on each group and hemisphere to test for significant changes in the area-amplitude measure. * denotes $p < 0.05$. (C), Larger strokes: $p = 0.0209$, n = 11 mice. (D), Larger strokes: $p = 0.0146$, n = 11 mice. (E-F), Changes in individual area-amplitudes of activation from Week 1 to Week 4 in the contralesional hemisphere (E) and across the entire cortex (F) are plotted against each mouse's change in forepaw asymmetry from Week 1 to Week 8 (n = 21 mice). Mice that received smaller strokes are shown as yellow circles outlined in dark blue; mice that received larger strokes are shown as solid dark blue circles. R^2 and p values are displayed on each plot.

To determine if early changes in remapping patterns of affected paw function predicted 8-week behavioral recovery, we correlated early changes in amplitude-areas of remapping to changes in forepaw asymmetry between week 1 and 8 using the cylinder rearing test. Early changes in contralesional (Figure 4.3E) and total (Figure 4.3F) stimulus-evoked activation amplitude-area (from week 1 to 4) predicted forepaw recovery at week 8. Larger amplitude-areas of stimulus-evoked activation forecasted worsened behavioral outcome. Mediation analyses of these data showed that both contralesional and total activation amplitude-areas predicted functional recovery, independent of infarct size (contralesional activation: $p = 0.021$ and total activation: $p = 0.008$; Figure 4.S3A,B).

Surprisingly, mice with larger strokes exhibited remapping of unaffected paw function as well (Figure 4.4). Larger strokes caused significant increases in unaffected paw evoked-response activation amplitude-areas at Week 4 in the contralesional hemisphere (Figure 4.4D), while no significant changes in evoked response contralesional activation amplitude-areas were observed in mice with smaller strokes during unaffected paw stimulation. There were instances of mice with larger stroke demonstrating ipsilesional evoked response activation during unaffected paw stimulation as well, though changes in ipsilesional activation amplitude-areas were not significant in either group (Figure 4.4C).

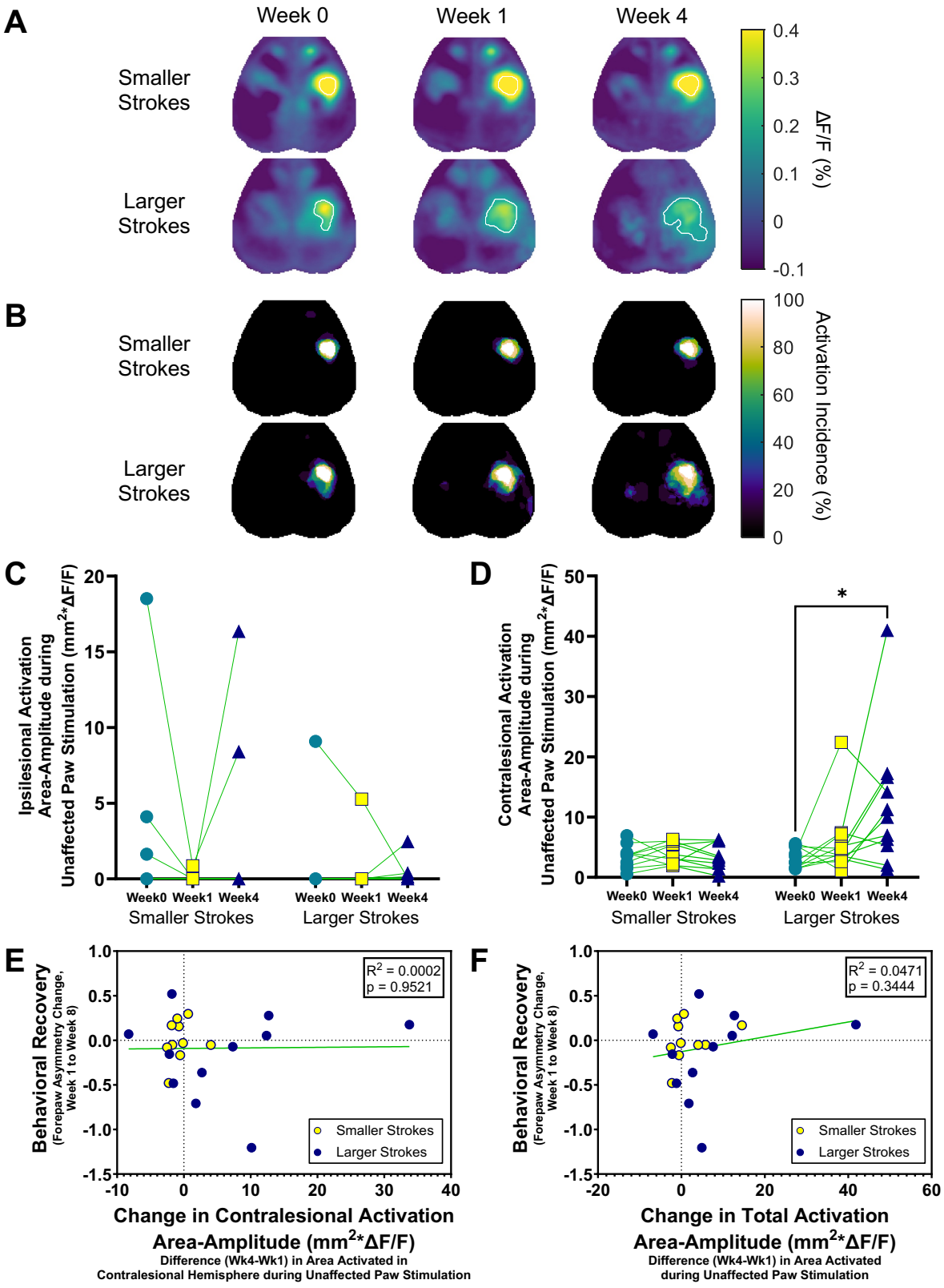
A
Week 0
Week 1
Week 4
Smaller Strokes
Larger Strokes
0.4
0.3
0.2
0.1
0
-0.1
ΔF/F (%)
B
Smaller Strokes
Larger Strokes
100
80
60
40
20
0
Activation Incidence (%)
C
Ipsilesional Activation Area-Amplitude during Unaffected Paw Stimulation (mm2*ΔF/F)
Week0 Week1 Week4
Smaller Strokes
Larger Strokes
D
Contralesional Activation Area-Amplitude during Unaffected Paw Stimulation (mm2*ΔF/F)
*
Week0 Week1 Week4
Smaller Strokes
Larger Strokes
E
Behavioral Recovery (Forepaw Asymmetry Change, Week 1 to Week 8)
R2 = 0.0002
p = 0.9521
Smaller Strokes
Larger Strokes
Change in Contralesional Activation Area-Amplitude (mm2*ΔF/F)
Difference (Wk4-Wk1) in Area Activated in Contralesional Hemisphere during Unaffected Paw Stimulation
F
Behavioral Recovery (Forepaw Asymmetry Change, Week 1 to Week 8)
R2 = 0.0471
p = 0.3444
Smaller Strokes
Larger Strokes
Change in Total Activation Area-Amplitude (mm2*ΔF/F)
Difference (Wk4-Wk1) in Area Activated during Unaffected Paw Stimulation

Figure 4.4: Larger stroke in $S1_{FP}$ causes diffuse remapping of unaffected forepaw circuits. (A), Group-averaged, block-averaged, and peak-averaged GCaMP fluorescence maps during unaffected forepaw stimulation are shown at each timepoint for each group. (B), Incidence maps of individual areas of activation during unaffected paw stimulation are shown at each timepoint for each group. (C-D), Areas of activation in the ipsilesional (C) and contralesional (D) hemispheres from (B) were multiplied by the summed fluorescence contained in those areas to obtain amplitude-area measures of activation for each mouse. Individual area-amplitudes in each hemisphere are plotted in spaghetti plots for each group (smaller strokes: n =10 mice; larger strokes: n = 11 mice). Two-way ANOVA tests with Dunnett's tests for multiple comparisons were performed for each group and hemisphere to test for significant changes in the area-amplitude measure. * denotes $p < 0.05$. (D), Larger strokes: $p = 0.0498$, n = 11 mice. (E-F), Changes in individual area-amplitudes of activation from Week 1 to Week 4 in the contralesional hemisphere (E) and across the entire cortex (F) are plotted against each mouse's change in forepaw asymmetry from Week 1 to Week 8 (n = 21 mice). Mice that received smaller strokes are shown as yellow circles outlined in dark blue; mice that received larger strokes are shown as solid dark blue circles. R^2 and p values are displayed on each plot.

4.4.3 Neuronal fidelity is differentially disrupted after $S1_{FP}$ stroke in an infarct size-dependent manner

In addition to spatial patterns of remapping, it is known that temporal dynamics of remapped areas can also influence behavioral recovery [181]. We investigated changes in temporal dynamics of both ipsilesional and contralesional remapped regions during unilateral stimulation of each forepaw. In particular, we examined neuronal fidelity, (the likelihood of a population of neurons to fire in response to a stimulus) over the first four weeks after stroke. To quantify fidelity, we measured changes in 3 Hz (the frequency of electrical forepaw stimulation) GCaMP power in both ipsilesional and contralesional regions of evoked activation during stimulation of each forepaw in individual mice.

As expected during affected paw stimulation, both groups of mice experienced significant attenuations of neuronal fidelity in ipsilesional areas of activation at Week 1 and Week 4 compared to Week 0, regardless of infarct size (Figure 4.5C). Both groups of mice also experienced significant reductions in neuronal fidelity in the contralesional forepaw somatotopic domain during affected paw stimulation at Week 1 compared to Week 0 (Figure 4.5D). Mice that received larger strokes also demonstrated significant decreases in neuronal fidelity in the contralesional forepaw somatotopic domain at Week 4 relative to Week 0 (Figure 4.5D).

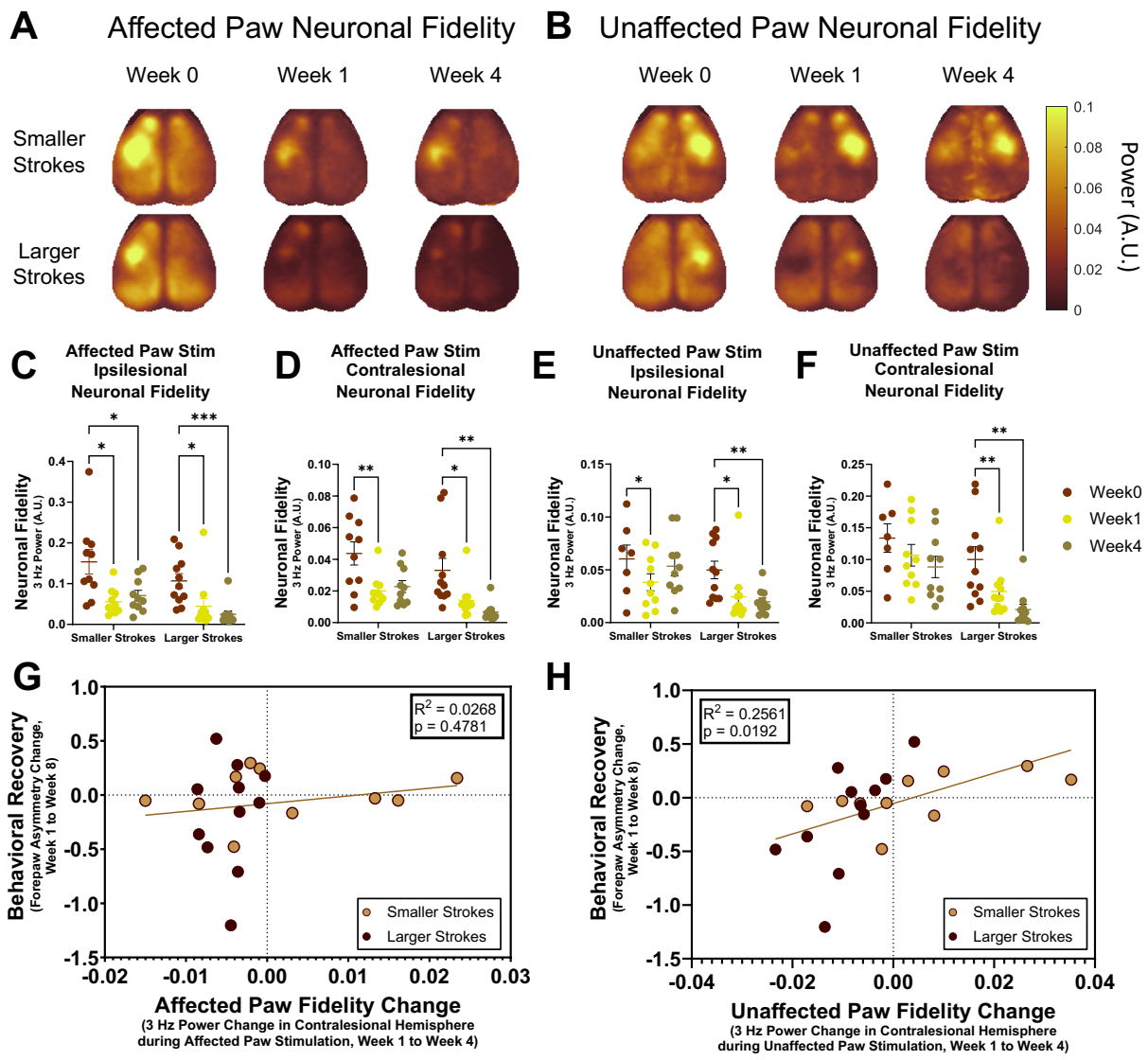

Figure 4.5: Neuronal fidelity of affected and unaffected circuits is differentially impacted in an infarct size-dependent fashion after S1$_{FP}$ stroke. (A-B), Group-averaged, block-averaged 3 Hz power maps denoting neuronal fidelity to stimulation are shown for each group and timepoint during affected (A) and unaffected (B) forepaw stimulation. (C-F) Fidelity is quantified in the ipsilesional S1$_{FP}$ using areas of activation obtained during affected paw stimulation (Figure 4.3) and in the contralesional S1$_{FP}$ using areas of activation obtained during unaffected paw stimulation (Figure 4.4). Fidelity is quantified in individual areas of activation in each hemisphere during unilateral stimulation of each forepaw. Individual data points are shown as circles, and means with standard error are shown as horizontal lines with error bars. Two-way ANOVA tests with Dunnett's tests for multiple comparisons were performed for each group and hemisphere to test for

significant changes in fidelity. * denotes $p < 0.05$, ** denotes $p < 0.01$, *** denotes $p < 0.001$. (C), Smaller strokes Week 1: $p = 0.0156$, $n = 10$; Smaller strokes Week 4: $p = 0.0342$, $n = 10$. Larger strokes Week 1: $p = 0.0114$, $n = 11$; Larger strokes Week 4: $p = 0.0006$, $n = 11$. (D), Smaller strokes Week 1: $p = 0.0083$, $n = 10$. Larger strokes Week 1: $p = 0.0198$, $n = 11$; Larger strokes Week 4: $p = 0.0041$, $n = 11$. (E), Smaller strokes Week 1: $p = 0.0367$, $n = 10$. Larger strokes Week 1: $p = 0.0321$, $n = 11$; Larger strokes Week 4: $p = 0.0024$, $n = 11$. (F), Larger strokes Week 1: $p = 0.0045$, $n = 11$; Larger strokes Week 4: $p = 0.0012$, $n = 11$. (G-H), Changes in individual neuronal fidelity from Week 1 to Week 4 in the contralesional hemisphere during affected (G) and unaffected (H) forepaw stimulation are plotted against each mouse's change in forepaw asymmetry from Week 1 to Week 8 ($n = 21$ mice). Mice that received smaller strokes are shown as light brown circles outlined in dark brown; mice that received larger strokes are shown as solid dark brown circles. R^2 and p values are displayed on each plot.

Unexpectedly, however, stimulation of the unaffected forepaw differentially induced changes in neuronal fidelity in the contralesional (intact) $S1_{FP}$ that was dependent on infarct size. Smaller infarcts had no effect on contralesional neuronal fidelity, whereas larger infarcts caused reductions in fidelity at Week 1 that worsened at Week 4 (Figure 4.5F). All mice showed attenuations in fidelity in ipsilesional regions of activation during unaffected paw stimulation at Week 1 compared to Week 0 (Figure 4.5E). Mice with larger strokes demonstrated a sustained reduction in fidelity in ipsilesional remapped regions at Week 4, as well (Figure 4.5E).

Changes in fidelity in the contralesional hemisphere during unaffected paw stimulation from Week 1 to 4 predicted 8-week recovery ($R^2 = 0.2561$, $p = 0.0192$)), with larger decreases in unaffected paw fidelity predicting worsening behavioral recovery (Figure 4.5H). Changes in fidelity in ipsilesional and contralesional areas of activation during affected paw stimulation ($R^2 = 0.0268$, $p = 0.4781$; Figure 4.5G), as well as

changes in fidelity in ipsilesional areas of activation during unaffected paw stimulation, did not predict functional recovery.

4.4.4 Disruptions in evoked coherence of bilateral forepaw somatosensory cortices predict functional outcome after stroke

Remapping and changes in neuronal fidelity to forepaw stimulation suggest that stroke caused both spatial and temporal changes in patterns of neural activation. We hypothesized that these dynamic changes in thalamocortical circuits would alter global brain networks that included these affected circuits. To examine temporal changes in global somatosensory networks, we measured 3 Hz mean-squared coherence between contralesional and ipsilesional areas of activation (bilateral stimulation-driven coherence) during individual stimulation of each forepaw.

Mice with larger strokes had significant decreases in bilateral coherence during unilateral affected paw stimulation 1 and 4 weeks after stroke (Figure 4.6A,C), and during unaffected paw stimulation 4 weeks after stroke (Figure 4.6B,D), while no other significant group-level coherence changes were noted for mice that underwent smaller strokes during stimulation of either paw (Figure 4.6A-D). Changes in bilateral stimulation-driven coherence during unaffected forepaw stimulation from baseline to week 1 predicted functional outcome (Figure 4.6F), but changes in coherence during affected paw stimulation did not correlate with or predict behavioral recovery (Figure 4.6E). Bilateral coherence changes during unaffected paw stimulation from baseline to week 1 predicted

functional outcome independent of infarct size measured by delta homotopy changes, as shown by mediation analysis (Figure 4.S3C).

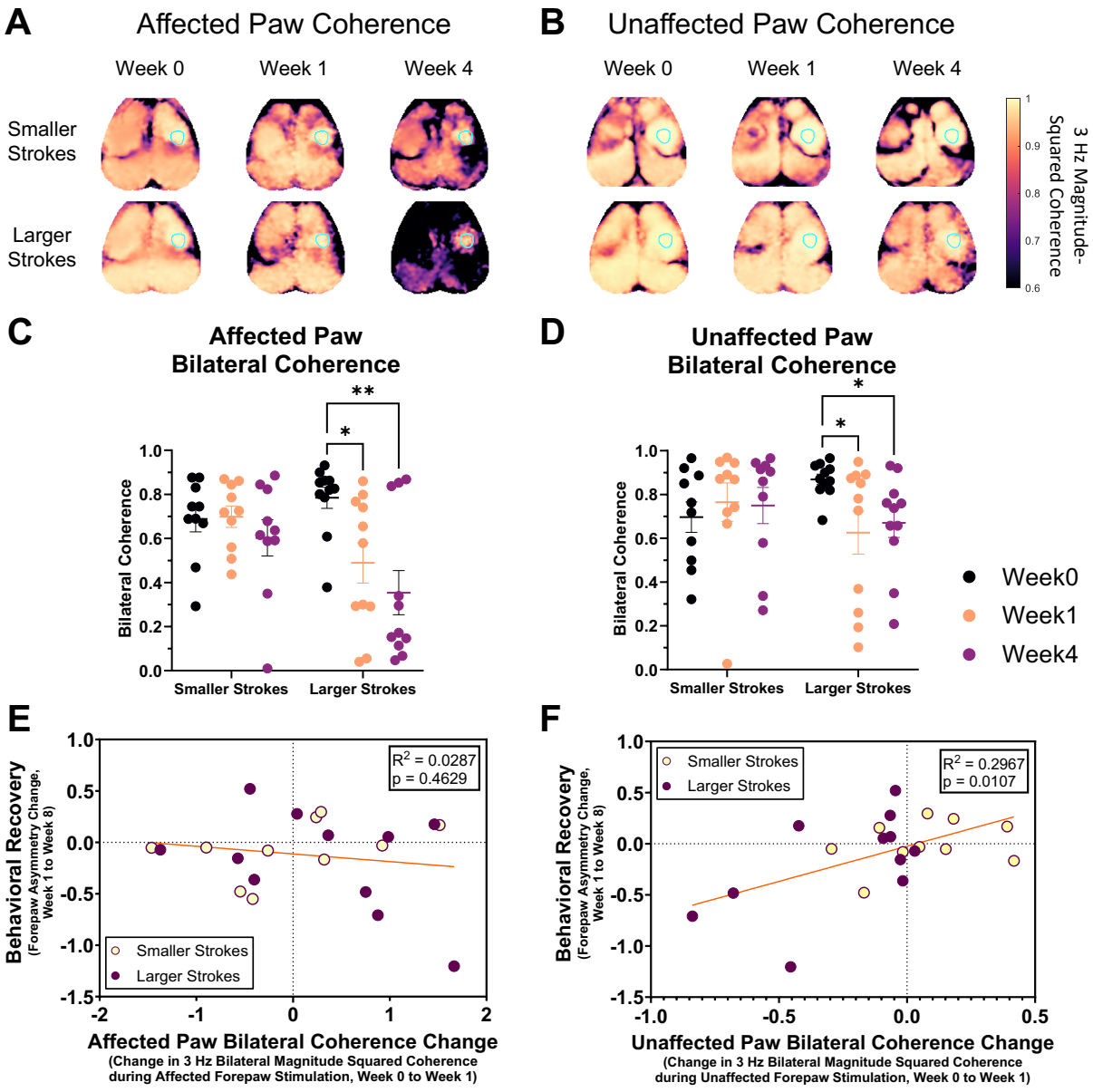

Figure 4.6: $S1_{FP}$ stroke size disparately influences bilateral coherence changes during unilateral stimulation of each forepaw. (A-B), Group-averaged, block-averaged 3 Hz mean-squared coherence maps are shown for each group and timepoint

during affected (A) and unaffected (B) forepaw stimulation. ROIs of group-averaged activation during unaffected paw stimulation are outlined in light blue to show approximate locations of average activity used to calculate maps. (C-D), Quantification of bilateral coherence between individual contralesional $S1_{FP}$ and ipsilesional $S1_{FP}$ are displayed during affected (C) and unaffected (D) forepaw stimulation. Individual data points are shown as circles, and means with standard error are shown as horizontal lines with error bars. Two-way ANOVA tests with Dunnett's test for multiple comparisons were performed for each group and hemisphere to test for significant changes in coherence. * denotes $p < 0.05$, ** denotes $p < 0.01$. (C), Larger strokes Week 1: $p = 0.0135$, $n = 11$; Larger strokes Week 4: $p = 0.0030$, $n = 11$. (D), Larger strokes Week 1: $p = 0.0429$, $n = 11$; Larger strokes Week 4: $p = 0.0322$, $n = 11$. (E-F), Changes in individual bilateral coherence from Week 1 to Week 4 during affected (E) and unaffected (F) forepaw stimulation are plotted against each mouse's change in forepaw asymmetry from Week 1 to Week 8 ($n = 21$ mice). Mice that received smaller strokes are shown as light yellow circles outlined in purple; mice that received larger strokes are shown as solid purple circles. R^2 and p values are displayed for each plot.

4.4.5 Larger $S1_{FP}$ strokes trigger hyperconnectivity across the contralesional hemisphere and with ipsilesional remapped circuits

To characterize global brain network changes after stroke, we performed awake, resting-state imaging on mice at all timepoints for functional connectivity (FC) analysis. Representative FC maps are shown in Figure 4.7A. We observed that larger strokes of $S1_{FP}$ caused hyperconnectivity between contralesional $S1_{FP}$ and large portions of the contralesional hemisphere, as well as with ipsilesional remapped $S1_{FP}$ regions 4 weeks after stroke. Mice that received smaller strokes did not experience any hyperconnectivity. Changes in spatial patterns of functional connectivity were quantified using node degree, a measure of a region's degree of connectivity with the rest of the cortex, of contralesional $S1_{FP}$ with the rest of the contralesional hemisphere (Figure 4.7B), which showed significant differences between mice that received smaller vs larger strokes.

Contralesional node degree 4 weeks after stroke was predictive of behavioral recovery as measured by the cylinder rearing assay, with a higher degree of contralesional hyperconnectivity forecasting worsening functional outcome (Figure 4.7C). Mediation analysis showed that Week 4 contralesional node degree predicted behavioral recovery independent of delta homotopy infarct size (Figure 4.S3D).

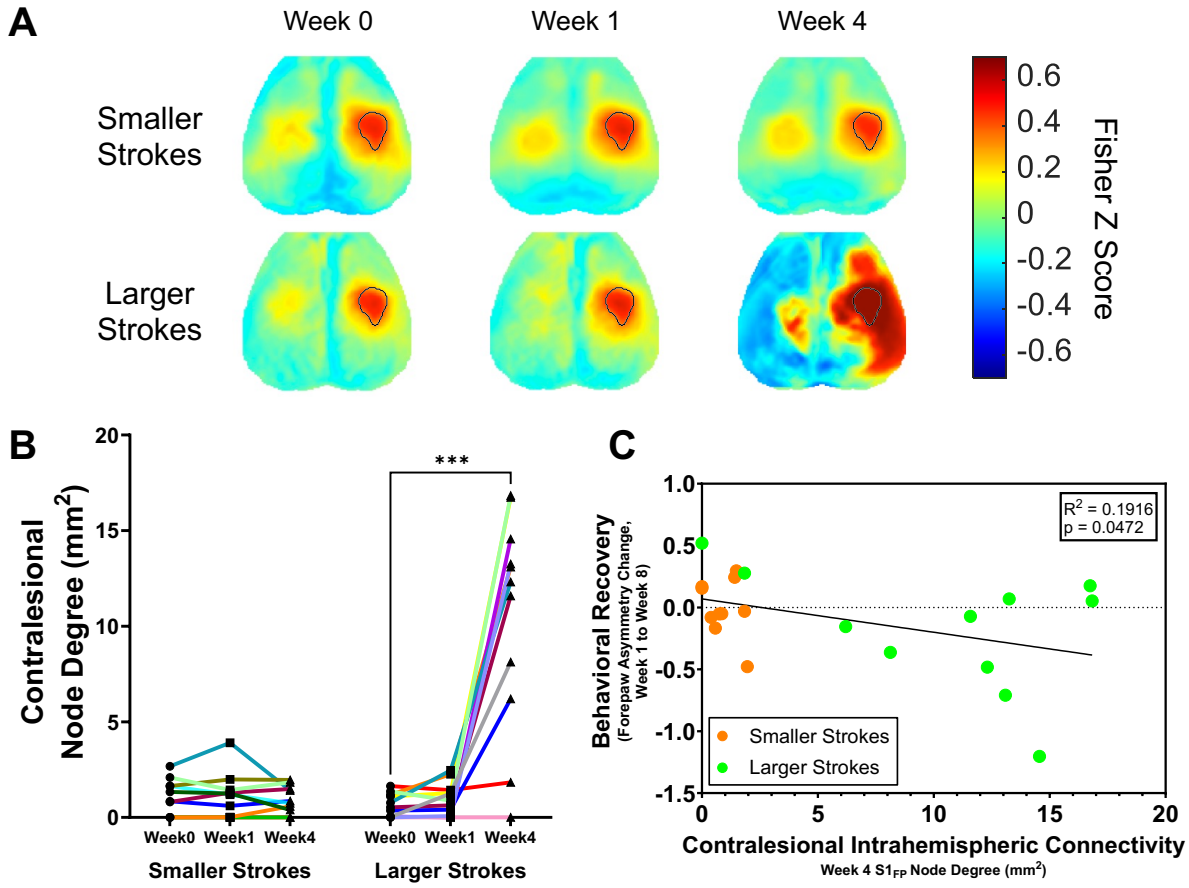

Figure 4.7: Larger stroke in $S1_{FP}$ causes substantial and maladaptive hyperconnectivity within the contralesional hemisphere. (A), Group-averaged, delta range (1-4 Hz) seed-based functional connectivity (FC) maps are displayed for each group at each timepoint. Maps were obtained by correlating average activity in the ROI outlined in black and white with activity in every other pixel in the cortex. (B), Node degree of the contralesional hemisphere was quantified by determining the number of pixels in

the contralesional hemisphere of an individual mouse's seed-based FC map with Fisher Z scores of at least 0.5. A two-way ANOVA test with Dunnett's tests for multiple comparisons was performed for each group to test for significant changes in node degree. Mice with larger strokes had significantly higher contralesional node degrees at Week 4 than at Week 0 ($p = 0.0003$, $n = 11$). (C), Individual Week 4 contralesional node degree values are plotted against each mouse's change in forepaw asymmetry from Week 1 to Week 8 ($n = 21$ mice). Mice that received smaller strokes are shown in orange; mice that received larger strokes are shown in green. R^2 and p values are displayed on the plot.

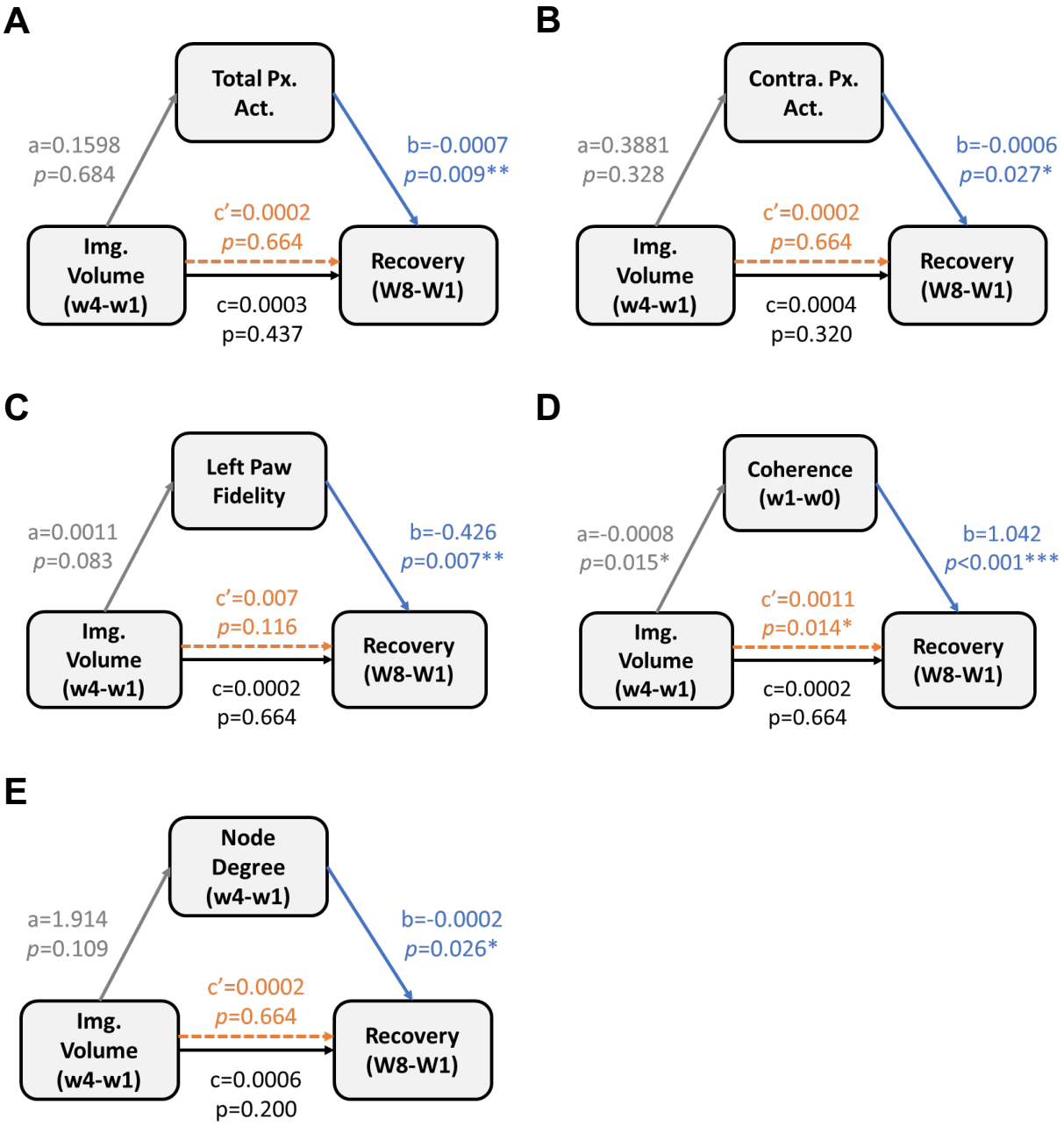

Figure 4.S3: Early changes in dynamics of local circuits and global networks predict functional recovery independently of infarct size. (A-E), Tripartite diagrams of mediation analyses are shown illustrating the statistical effect of infarct size (as measured by delta homotopy infarct area) on functional recovery (as measured by changes in forepaw asymmetry in the cylinder rearing assay) mediated through the variables total pixel activation-area (A), contralesional pixel activation-area (B), unaffected paw fidelity changes (C), unaffected paw bilateral coherence changes (D), and

Week 4 contralesional node degree (E). In each diagram, “a” represents the effect of infarct volume on the variable at the top of the diagram (termed the mediator), “b” represents the effect of the mediator on recovery (controlling for infarct size; the statistical effect of greatest interest), “c” represents the total effect of infarct size on recovery without controlling for the mediator, and “c’ ” represents the direct effect of infarct size on recovery, controlling for the mediator.

4.5 Discussion

Infarct volume is known to be a salient predictor of recovery after stroke in animal models [182], as well as in human stroke [183, 184]. In this study, we used smaller and larger infarcts centered on $S1_{FP}$ mice to examine early changes in functional imaging parameters (reflective of circuit and network plasticity) that predict longer-term behavioral recovery. We found that larger strokes completely ablating $S1_{FP}$ caused diffuse, bilateral remapping of affected paw function with larger activation areas, while smaller, partial infarctions of $S1_{FP}$ elicited focal remapping within the original $S1_{FP}$. Neuronal fidelity was differentially impacted by stroke size: all strokes unsurprisingly elicited significant attenuations in fidelity during affected paw stimulation, but complete ablations caused markedly greater disruptions in fidelity during unaffected paw stimulation. Complete ablations of $S1_{FP}$ also induced significant decreases in bilateral coherence during stimulation of either paw, as well as hyperconnectivity in the contralesional, intact hemisphere, findings that were absent in mice that received partial ablations of $S1_{FP}$. These results suggest that spatiotemporal characteristics of early circuit and network repair influence behavioral recovery in mice, and that these properties of plasticity can facilitate prediction of functional outcome better than infarct size alone.

4.5.1 Disparate spatial patterns of neuronal remapping after $S1_{FP}$ stroke

Remapping as imaged from the cortical surface likely represents repair of damaged excitatory [185] and inhibitory [186] cortical circuits, as well as thalamocortical [187] projections after smaller stroke. In our study, smaller $S1_{FP}$ strokes (partial ablation) induced remapping within and nearby $S1_{FP}$, likely representing repair of thalamocortical connections. Consistent with this hypothesis, reorganization of thalamocortical projections to sensory cortex likely causes mesoscale remapping after small photothrombotic stroke in rats [188]. Furthermore, optogenetic stimulation of thalamocortical projections enhances motor outcome after small photothrombotic stroke in $S1_{FP}$ of mice [187], suggesting that remodeling of thalamocortical projections heralds recovery of function. Our data support this finding, demonstrating that mice that underwent peri-infarct remapping within $S1_{FP}$, likely due to thalamocortical circuit repair, experienced improved behavioral recovery.

Mice subjected to slightly larger $S1_{FP}$ strokes exhibited a drastically different remapping pattern. These animals demonstrated diffuse, bilateral activations during affected paw stimulation, exhibiting remapping into ipsilesional regions outside the original $S1_{FP}$ and into large portions of the spared, contralesional hemisphere. Prior work has demonstrated that diffuse, bilateral patterns of remapping are typically observed in stroke patients with large infarcts—such as those with large vessel occlusion (LVO) [189], and herald poor outcome [108, 153]. In rodents, middle cerebral artery occlusion (MCAO,

the mouse equivalent of an LVO stroke in humans) produces a similar diffuse pattern of remapping [148, 151], and causes more severe behavioral deficits than those produced by smaller photothrombotic lesions [190]. Our results show similar findings; however, the surprising observation is that a small increase in infarct size can have a major impact on patterns of remapping and recovery. We found that a threshold surface area of 0.8-1.0 mm^2 resulted in a dramatic transition to diffuse, bilateral remapping patterns. Interestingly, these mice are also those that appear to have major ablation of the $S1_{FP}$ based on activation patterns at week 1, suggesting an importance of residual healthy tissue in the injured somatotopic domain for robust repair and recovery. Moreover, it has been shown that receptive fields for a given cell often only reflect a small portion of the functional inputs they receive [191, 192]. This is broadly seen across the somatosensory cortex [193], and is demonstrated by the activation of hindlimb cortices during peripheral forelimb stimulation after photothrombotic stroke in mice [194]. Furthermore, sensitivities of receptive fields of cells in contralesional limb cortices, which normally are highly tuned to unaffected limb function, are altered to favor affected limb function after stroke [195]. In our experiment, mice with larger strokes exhibited similar remapping and activation in ipsilesional hindlimb and contralesional sensory cortices, which is likely due to a maladaptive compensatory remodeling of cortico-cortical networks by altering synaptic efficacies, not by remodeling thalamocortical circuits.

Spatial remodeling of intact circuits not only occurred in affected paw circuits, but also in unaffected paw circuits. Our results show significantly larger activation areas

during unaffected paw stimulation than at baseline in mice with larger strokes, a trend that was not observed in mice with smaller strokes. The functional significance of this finding is unclear because our behavioral tests assess relative function (right vs. left function) but not the absolute ability of individual limbs. However, it is interesting that previous papers have reported deficits in unaffected limb function after stroke in humans [166, 167]. Remapping of unaffected paw function could be due to varying degrees of disinhibition of the contralesional hemisphere caused by varying degrees of ischemic injury [196-198]. Greater areas of unilateral cortical injury may cause disinhibition to larger areas of the contralesional hemisphere. This disinhibition likely mediates temporal changes in connected regions in the contralesional hemisphere as well, which we discuss in more depth later. Still, the reason as to why complete ablation of the somatotopic domain seems to be the threshold that induces remapping of unaffected circuits remains elusive and should be explored further.

The enhanced activation of the contralesional hemisphere during affected paw stimulation was also progressive: the contralesional areas activated in Week 4 were generally larger than those observed in Week 1. This growth of contralesional activation area was strongly predictive of poor behavioral recovery as well, suggesting that this progression was a maladaptive change to brain circuitry. This finding is validated in other studies which consistently show that the normalization and return of lateralization of evoked responses after stroke is associated with improved behavioral recovery, both in animal models [148, 199] and humans [121]. Additionally, contralesional activation during

peripheral stimulation temporally precedes the contralesional hyperconnectivity that we observed in mice with larger strokes at Week 4, something that has not been shown previously. Though hyperconnectivity has been demonstrated after both TBI [200] and stroke [28], the functional relevance of this hyperconnectivity is unknown. We consider the functional implications of our connectivity findings later in this discussion.

4.5.2 Temporal dynamics of remapped circuits

Our results show an infarct size-dependent loss of synchronization, which we measure as neuronal fidelity, in areas of activation during stimulus-evoked responses. Larger strokes induce population-level neuronal fidelity decreases that progressively worsen from Week 1 to Week 4, both in ipsilesional and contralesional cortices, whereas smaller strokes only show fidelity decreases ipsilesionally. It is likely that some of the changes in temporal dynamics and synchronization we observed are related to circuit remodeling, mentioned above, and damage to inhibitory networks. The activity of inhibitory interneurons and groups thereof are known to control network synchrony across the cortex, and damage to these gate-keeping networks, such as that caused by stroke, can lead to asynchrony in network dynamics across multiple timescales in humans [201-203]. Moreover, increasing the order of polysynaptic connection of a circuit, which likely occurs during circuit remodeling that we have suggested is involved in the case of larger strokes, adds increasing levels of noise [201, 204], degrading signal strength and synchronization. Degradation of signal strength and synchronization likely compounds as the signal spreads across nodes of a network. Greater degrees of damage to these

inhibitory networks probably produce greater disruptions in network synchronization, leading to more severe behavioral deficits [203].

The decline in neuronal fidelity and synchronization in areas of activation during unaffected paw stimulation after larger strokes ablating the entire forepaw somatotopic domain, which is absent in mice with smaller strokes, is even more perplexing. Areas of cortex that are activated during both unilateral affected and unaffected paw stimulation at Week 4 after larger stroke suggests that sensitivities or tuning of neuronal populations in these regions have begun to shift toward the affected paw. As neuronal tuning has been shown to impact firing rate [205, 206], it is therefore plausible that firing rates of these cells are being affected by these tuning shifts. Furthermore, ischemia-inflicted damage to nodes, and specifically inhibitory interneuron networks, projecting to these contralesional regions may also cause disinhibition within functionally related circuits, similar to that demonstrated in motor cortex strokes [196-198].

4.5.3 Connectivity changes after stroke

In our analysis of resting-state functional connectivity changes after stroke, we observed substantial increases in the degree of connectivity of the unaffected $S1_{FP}$ with much of the contralesional hemisphere after larger strokes, which is likely a spatial quantification of contralesional hyperexcitability [207, 208]. Nonetheless, the resting-state nature of these analyses does not provide any tuning or sensitivity information about these circuits. Activation topographies during affected and unaffected paw stimulation

both mirror those of resting state functional connectivity maps, further clouding the functionality of this network.

Most of the research concerning connectivity changes of stroke-affected circuits has focused on resting-state functional connectivity (RSFC) networks [25, 155]. Though changes in RSFC networks have been associated with functional recovery after stroke, the signal to noise ratio of resting-state activity is low and confounded by functionally irrelevant signals [209]. Here, we also employ a different connectivity approach for prognosis: stimulus-driven bilateral coherence of functional circuits. We believe this measure is more sensitive than RSFC because of the higher amplitude neuronal activity (relative to resting state activity) that is driven in functionally relevant circuits by peripheral stimulation. Our results show greater 3 Hz bilateral coherence deficits in mice with larger strokes during affected paw stimulation, as well as significant deficits in 3 Hz bilateral coherence during unaffected paw stimulation, an observation absent in mice with smaller strokes. These results further suggest a dose-dependent disruption of population-level neuronal synchronization caused by graded damage to inhibitory circuits [202, 203], in addition to commenting on the importance of inhibitory networks within a functional domain in controlling spatially and temporally efficient global brain network function. Inhibitory neurons also play an important role in the propagation of slow waves across the cortex [210]. In our experiments, bilateral coherence maps also show significant coherence of cortical areas involved in propagating slow waves of neuronal activity during affected paw stimulation at baseline that is significantly disrupted after stroke in mice, a

finding that agrees with previous work [174]. Our results build upon this, demonstrating an infarct size-based graded disruption (though not statistically significant) of bilateral coherence during affected forepaw stimulation and a significant degradation of coherence during unaffected forepaw stimulation in mice with larger strokes. These data suggest that the efficiency of slow wave propagation is dictated by the degree of spared functional cortical territory, and in turn inhibitory circuitry, that initiates the wave.

In summary, we have shown significantly different courses of repair and recovery after focal ischemic stroke of varying size in mice. We also establish the importance of spatiotemporal dynamics of both affected and unaffected functional circuits, as well as the brain networks including these circuits, in the prediction of functional recovery after stroke. These results inform and motivate new experiments investigating mechanisms that govern repair of local circuits and global networks after stroke and how these mechanisms of repair contribute to functional recovery.

Chapter 5:

Conclusions and Future Directions

5.1 Neurovascular Coupling in Cantu Syndrome

In Chapter 2, I discussed a case study on the sensitivity of neurovascular coupling in a mouse model of Cantu syndrome, a disease caused by gain-of-function mutations in pore-forming and regulatory subunits of ATP-sensitive potassium channels (K_{ATP}). Our data show significant disruptions of neurovascular coupling during both pharmacological activation and inactivation of K_{ATP} channels, in addition to enhanced sensitivity of gain-of-function mutant animals to pharmacological activation. The results demonstrate the delicateness of the neurovascular unit and suggest complex roles played by multiple different cell and tissue types to maintain this important connection. As discussed earlier, the responsibilities of different mural and vascular endothelial cells in the neurovascular coupling response are still poorly understood.

Previous experiments have demonstrated marked effects of K_{ATP} channel activity on systemic blood pressure [57, 211-213]. These results suggest that K_{ATP} activity is extant in cells surrounding arteries and arterioles in normal conditions, and that K_{ATP} activity in arterial and arteriolar smooth muscle cells is essential to setting vascular tone at a point in which hemodynamic responses to functional activity, such as neural activity

in the brain, is optimized. In such a model, shown in Figure 5.2B, vascular smooth muscle cells are maximally contracted when K_{ATP} conductance is below a certain point, and maximally dilated when K_{ATP} conductance is above a certain point. Between these extreme levels of K_{ATP} activity though, K_{ATP} activity via Kir2.1 channels (discussed in Chapter 3) allows for dynamic regulation of arterial and arteriolar tone to modulate blood flow. The dynamics of the model also show decreasing changes in hemodynamic responses when K_{ATP} cells are operating close to their activity extrema, which we believe may represent their activity levels in dysfunction and disease.

In the mechanism presented above, K_{ATP} activity in vascular smooth muscle cells is the main driver of vascular tone and hemodynamic response alterations. However, single-cell transcriptomics have predicted high expression of K_{ATP} channels in pericytes [214, 215], and other experiments have implicated pericytes in the neurovascular response, as well [39, 40, 216]. Pinacidil application to arteriolar-capillary junctions caused strong vasodilation, but decreased vasodilatory responses during whisker stimulation [39], suggesting a dynamic responsibility for pericytes in neurovascular coupling.

Examining the role of pericytes in neurovascular coupling requires transgenic mice to express mutant channels in a selective, pericyte-specific manner. We crossed Tg[CX1-eGFP-Kir6.1-AAA] mice (Kir6.1 [AAA]) with NG2-Cre mice to obtain offspring (NG2-Cre x Kir6.1 [AAA], or NG2-DN) that express a tamoxifen-inducible dominant negative isoform

of a mutant Kir6.1 subunit, in which the channel's selectivity filter sequence Gly-Tyr-Gly is replaced with a nonfunctional Ala-Ala-Ala sequence, under the pericyte-specific promoter NG2. The NG2 promoter was selected over other pericyte-specific promoters, such as PDGFRB, due to the salient changes in potassium current observed upon application of the K_{ATP} activator, pinacidil, and the K_{ATP} inhibitor, glibenclamide, during whole cell patch-clamp recordings (Figure 5.1A,B). Pericytes isolated from NG2-Cre x Kir6.1 [AAA] animals showed an absence of potassium current during patch clamp recordings even during pinacidil and glibenclamide application, confirming integration of the nonfunctional dominant negative Kir6.1 [AAA] channel isoforms into endogenous K_{ATP} channels (Figure 5.1C,D).

To determine the role of pericyte-specific K_{ATP} activity in the neurovascular response, we used the same whisker-evoked response optical imaging recording and analysis techniques described in Chapter 2 and compared hemodynamic responses of NG2-Cre x Kir6.1 [AAA] animals before and after induction of the dominant negative channel isoform transgene, as well as against littermate controls. Relative to pre-induction measurements, NG2-Cre x Kir6.1 [AAA] mice demonstrated a significant attenuation of the maxima of their hemodynamic responses ($p = 0.0170$, $n = 10$ hemispheres), in addition to shortening of their hemodynamic responses ($p = 0.0024$, $n = 10$ hemispheres), after transgenic induction (Figure 5.1E-H). However, the time to maxima was not significantly different for either group, before or after tamoxifen administration. Given the significant reduction in hemodynamic responses during both

K_{ATP} activation and inhibition reported in Chapter 2, these data suggest that pericyte-specific K_{ATP} channel activity is responsible for only some of the effects observed in the hemodynamic response, and likely those pertaining to the later portions of the response.

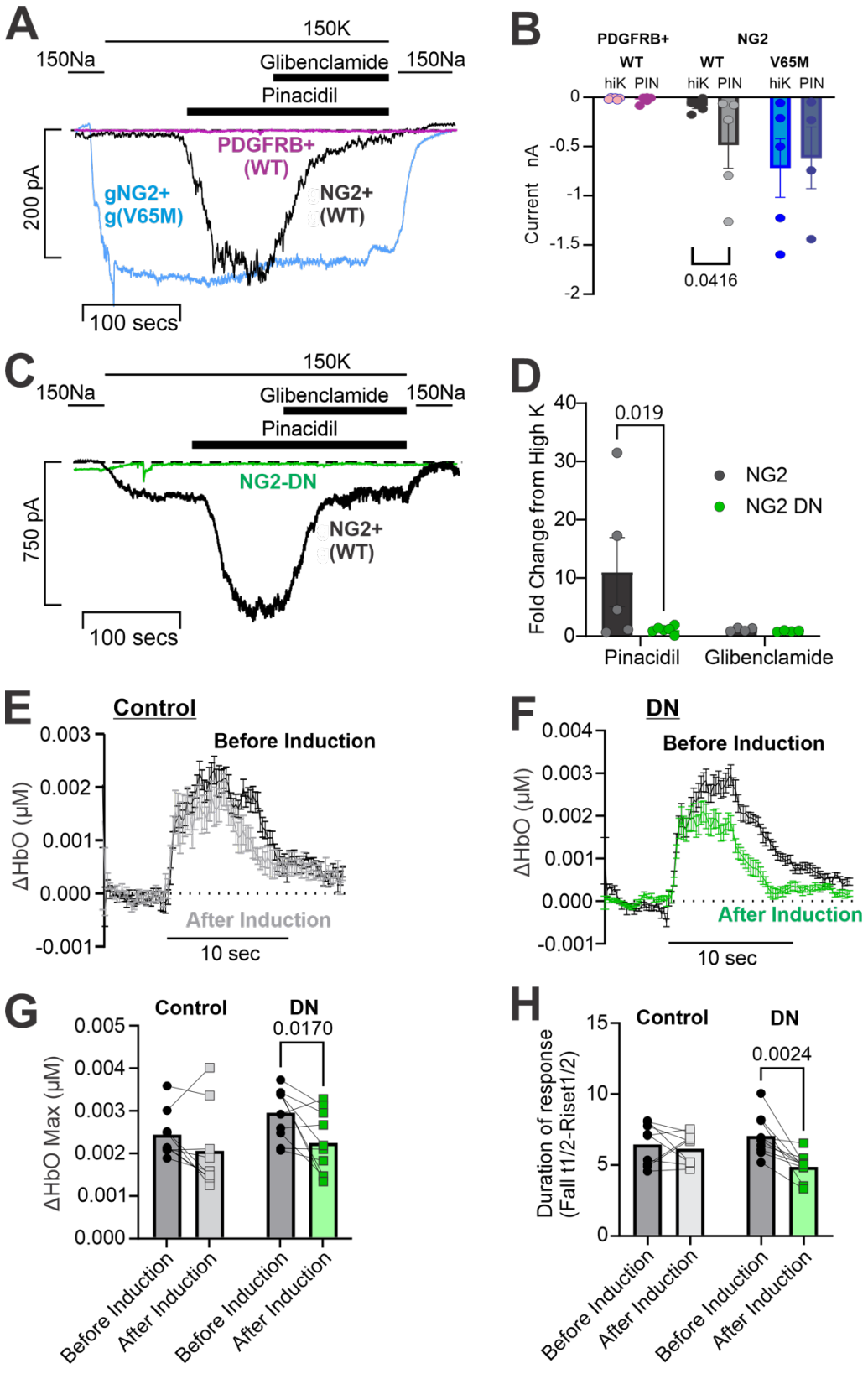
A
150K
150Na
Glibenclamide
150Na
Pinacidil
PDGFRB+
(WT)
gNG2+
g(V65M)
NG2+
(WT)
200 pA
100 secs
B
PDGFRB+
NG2
WT
WT
V65M
hiK PIN
hiK PIN
hiK PIN
Current nA
0
-0.5
-1
-1.5
-2
0.0416
C
150K
150Na
Glibenclamide
150Na
Pinacidil
NG2-DN
NG2+
(WT)
750 pA
100 secs
D
Fold Change from High K
40
30
20
10
0
0.019
NG2
NG2 DN
Pinacidil
Glibenclamide
E
Control
Before Induction
ΔHbO (μM)
0.003
0.002
0.001
0.000
-0.001
After Induction
10 sec
F
DN
Before Induction
ΔHbO (μM)
0.004
0.003
0.002
0.001
0.000
-0.001
After Induction
10 sec
G
Control
DN
0.0170
ΔHbO Max (μM)
0.005
0.004
0.003
0.002
0.001
0.000
Before Induction
After Induction
Before Induction
After Induction
H
Control
DN
0.0024
Duration of response
(Fall t1/2-Riset1/2)
15
10
5
0
Before Induction
After Induction
Before Induction
After Induction

Figure 5.1: Role of pericyte K_{ATP} in neurovascular coupling response (A) Representative whole cell voltage-clamp traces from PDGFRB-positive WT, and NG2-positive WT or Kir6.1[V65M] pericytes. Patches were exposed to high [Na] or high [K], and 10 μM glibenclamide, or 100 μM pinacidil, as indicated. **(B)** Steady-state current, during final 50 seconds in each condition (± s.e.m.) from experiments as in A. **(C)** Representative whole cell voltage-clamp traces from NG2-positive WT and tamoxifen-induced dominant-negative NG2-Cre recombinase/Kir6.1[AAA] double transgenic (NG2-DN) pericytes. Patches were exposed to high Na or high K and 10 μM glibenclamide, or 100 μM pinacidil, as indicated. **(D)** Fold change in current relative to that in high [K], during final 50 seconds in pinacidil or glibenclamide (± s.e.m.) from experiments as in C. **(E,F)** Mean change (± s.e.m.) of oxygenated hemoglobin (Oxy) signals, before and after tamoxifen-induction of single transgenic Cre-recombinase (control, E), and NG2-Cre recombinase/Kir6.1[AAA] double transgenic animals (F). **(G)** Maximum change in oxygenated hemoglobin (Oxy max) signals in WT and NG2-DN, before and after induction. Individual paired values are given and significant p-values, in addition to mean values. **(H)** Duration of Oxy signal in WT and NG2-DN, before and after induction. Individual paired values are given and significant p-values, in addition to mean values.

In the context of recent literature, the discrepancies between hemodynamic responses during global inactivation (SUR2 KO) and pericyte-specific knockdown of K_{ATP} activity have led us to propose a dual mechanism for the control of neurovascular coupling by cell-dependent K_{ATP} activity, visually described in Figure 5.2. We postulate that the total hemodynamic response observed is in fact a sum of the contributions of K_{ATP} channel activity from vascular smooth muscle cells and pericytes. Shortened hemodynamic responses in NG2-DN animals suggest that pericytes play a delayed, metabolically mediated role in neurovascular coupling, in contrast to the immediate, [K+]-mediated role played by vascular smooth muscle cells. In NG2-DN animals, initial hemodynamic responses are strong, much like those of wildtype animals, but after repeated stimuli, the hemodynamic response tapers off and quickly vanishes after cessation of stimulation, suggesting that a delayed component of coupling is lost in these animals (Figure 5.2C).

Consistent with this dual-controlled model, neurovascular coupling is delayed in global K_{ATP} SUR2 KO animals, further implicating vascular smooth muscle cells in the immediate responses to local neural activity. Several experiments have substantiated the finding that arteriolar vascular responses are quicker than capillary-based vascular responses [217-219].

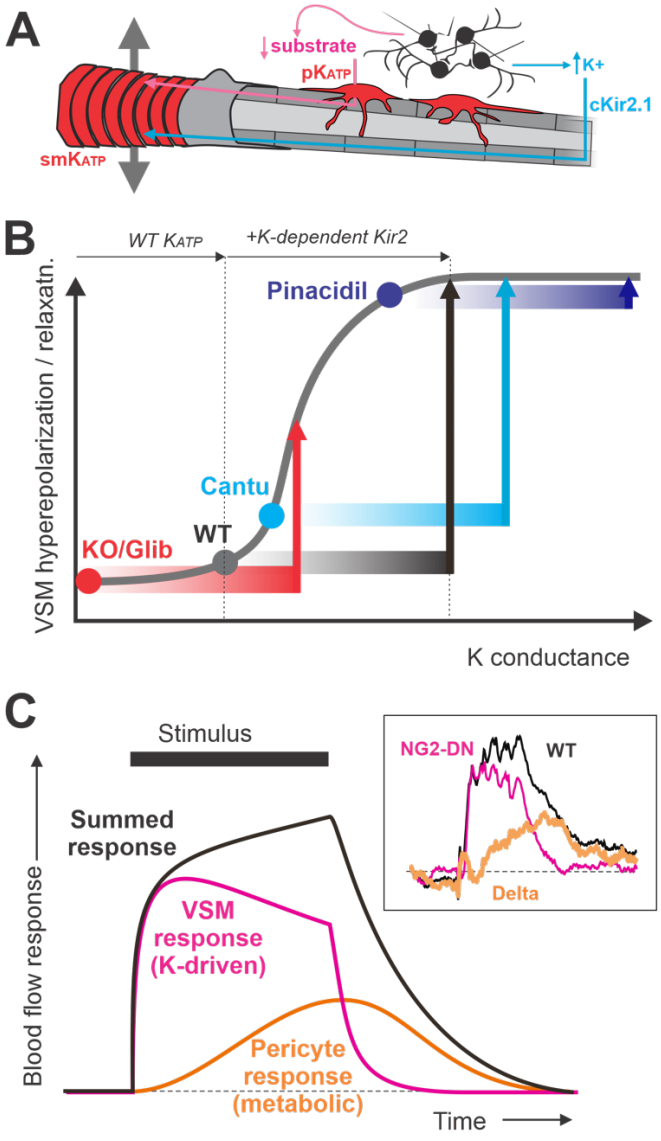

Figure 5.2: Proposed dual role of Kir6.1/SUR2-dependent K_{ATP} channels in neurovascular coupling (A) Cartoon illustration of the proposed mechanistic involvement of K_{ATP} in two distinct locations - smooth muscle K_{ATP} (smK_{ATP}) in pre-capillary arterioles and pericyte K_{ATP} (pK_{ATP}). Local neural activity leads to increased extracellular [K], activating Kir2.1 channels in capillary endothelium, generating a hyperpolarizing conductance that is propagated back to VSM via gap junctions (pink). K_{ATP} activity in arteriolar smooth muscle (VSM) determines the set-point for the hyperpolarization and relaxation that then results. Neural activity also reduces metabolic substrate, activating pK_{ATP}, generaqting additional hyperpolarizing conductance that is also propagated back to VSM via gap junctions (orange). **(B)** K_{ATP} activity in arteriolar smooth muscle (VSM) determines the set-point for the hyperpolarizing and relaxing effects conducted to the arteriole by gap junctional coupling of K-driven Kir2 channel activation in capillary endothelial cells[ref]. Under normal conditions (WT), the added K-dependent Kir2 conductance will shift rightwards along the response curve causing optimal hyperpolarization and relaxation. Below a certain overall K conductance, VSM cells will be maximally depolarized and contracted; above a certain level, cells will be maximally hyperpolarized and relaxed. The model thus implies that the same level of [K]-induced Kir2 conductance will have a lesser hyperpolarizing effect when K_{ATP} is very low (KO, glibenclamide) or increased (Cantu, pinacidil). **(C)** We propose that VSM and pericyte K_{ATP} play two distinct roles in NVC. In response to a given stimulus, the K-driven VSM response (pink) will be nearly instantaneously activated, and decay rapidly following the end of the stimulus. Conversely, being very closely associated with neurons, pericyte K_{ATP} will show delayed activation due to metabolical effects once neural activity is initiated, adding an additional hyperpolarizing/relaxing signal that further increases blood flow during stimulation (orange), summing with the K-driven response to generate the full response (black). The inset shows the the mean oxygenated hemoglobin signals from WT and NG2-DN mice (from Figure 2.3E). Assuming that these reflect the normal summed response (WT) and the K-driven VSM component only (NG2-DN), the difference between them (orange) will reflect the pericyte-specific component.

The validity of this model relies upon the accurate isolation of each cell-type-specific contribution of the neurovascular response. Isolation of each cell-type-specific component of the neurovascular response hinges upon the specificities of the promoters used to knockdown K_{ATP} activity in target tissue types. NG2, the pericyte-specific promoter used in this study, is expressed in mural cells beyond pericytes, like vascular

smooth muscle cells [220], and more specific promoters exist to more precisely target dominant negative channel expression to pericytes, such as the Atp13a5 promoter [221]. It is likely that the experiment will need to be repeated with dominant negative channel knockdown under either the Atp13a5 promoter, or a similarly precise pericyte-specific promoter, to confirm the pericyte-specific contribution to neurovascular coupling. Furthermore, it is also probable that K_{ATP} activity in endothelial cells contributes to neurovascular response dynamics. We are currently examining hemodynamic responses in mice who have Kir6.1 [AAA] dominant negative knockdown of K_{ATP} activity under the SM22 and TIE2 promoters. SM22 is vascular and visceral smooth muscle cell-specific promoter [222, 223], while TIE2 is a promoter specific to vascular endothelial cells, with robust expression in arteriolar endothelial cells [224, 225], though some TIE2 expression can also be observed in endothelial cells surrounding capillaries [226]. In accordance with our proposed model, we expect to see significant delays in the time-to-peak of hemodynamic responses to stimulation in SM22-DN animals, but are uncertain of how the hemodynamic responses of TIE22-DN animals will be affected. In both strains of animals, barring nonspecific knockdown of K_{ATP} activity, we expect to see oximetric decay kinetics similar to those observed in wildtype mice, as we believe this latter portion of the hemodynamic response is governed by K_{ATP} activity in pericytes. We will confirm specificity of dominant negative transgene expression in both animal lines using whole cell-patch clamp recordings of pericytes, arteriolar smooth muscle cells, and vascular endothelial cells.

The future of this line of inquiry has enormous potential to shed light upon cell- and channel-specific contributions to the neurovascular response, as well as offer targets for therapeutic interventions. A condition similar to Cantu Syndrome, called ABCC9-dependent Intellectual disability Myopathy Syndrome (AIMS), is caused by loss-of-function mutations to ABCC9, the gene encoding the SUR2 subunit of KATP channels. AIMS patients are thought to lack any SUR2 expression, and demonstrate clear intellectual disability [227]. ABCC9 loss-of-function mutations are also related to hippocampal sclerosis of aging (HSA) [228, 229], a frequently-observed Alzheimer's-related condition of pathological neuron death and gliosis in the hippocampus [230] that is correlated with dementia and vascular cognitive impairment [231]. As little evidence exists pointing to SUR2 expression anywhere besides vascular tissue in the brain [231], we believe that intellectual disability exhibited in AIMS and HSA-related dementias could be due to critical K_{ATP}-mediated disruption of neurovascular coupling.

5.2 Early Repair and Long-Term Recovery after Stroke

In Chapter 4, I showed that early patterns of neural circuit and network repair can be used to predict long-term functional outcome after stroke. This experiment was methodologically innovative, using photothrombosis to create infarcts of different sizes. But the true novelty in the study lies in the elucidation of *early* mechanisms of repair that prognosticate long-term recovery independently of infarct size. In these investigations, I demonstrated that spatial remapping patterns of both affected and unaffected circuits were differentially impacted by focal ischemic stroke of varying size. Furthermore,

temporal dynamics of affected and unaffected remapped circuits were also affected disparately by infarct size. There were also significant differences in connectivity and coherence patterns between ipsilesional and contralesional regions of activation in larger strokes compared to smaller strokes. Ultimately, we demonstrated that only slight increases in infarct volume can cause distinctly different modes of repair, but continuous variables measuring spatiotemporal characteristics of repair, regardless of repair trajectory, were predictive of functional outcome independently of infarct size.

Our examination of early repair patterns that predicted long-term recovery trajectories used a GECI, specifically GCaMP6f, to directly measure neural activity. However, with a half-decay time of approximately 200-300 ms [23], it is only capable of measuring activity up to around 8 Hz. This limitation of temporal resolution thus significantly constrains our ability to measure neural activity in higher frequency bands, such as beta (15-30 Hz) [232-234] and gamma bands (30-80 Hz) [235, 236], which contain important information regarding neural dynamics and how they relate to function, especially after stroke. Indeed, optical imaging of high-frequency neural activity is currently limited by fluorophore decay kinetics, with the fastest half-lives of population-level neural activity being on the order of 100-200 ms [23, 237]. The most advanced family of fluorophores currently available, the jGCaMP8 series, has decay half-lives anywhere from 90-140 ms, which allows for the visualization of up to 40 Hz activity in small groups of neurons (less than 5) *in vitro* using two-photon microscopy [237]. However, wavelength-dependent absorption and scattering of emitted light by cortical

tissue and the cranium attenuates fluorescence of blue-shifted fluorophores, like those in the jGCaMP family, more than red-shifted fluorophores [238], like those in the jRGECO family. Furthermore, optogenetic tools using channel rhodopsins have significant absorption in the blue range of visible light, making the use of GCaMPs difficult in experimental paradigms involving optogenetic stimulation [23]. The use of red-shifted fluorophores like jRGECO *in vivo* thus holds promise to improve signal-to-noise ratios of fluorescence representing neural activity, a characteristic that could substantially improve studies in which signal-to-noise ratio of neural activity is reduced, as it as after stroke.

Our study also examined patterns of neural activity at meso- and macroscopic levels. Microscopic imaging techniques such as two-photon microscopy offer higher spatial resolution than our employed method of wide-field optical imaging and are capable of examining dynamic subcellular structures and processes, like dendritic spine turnover [239-241] and axonal sprouting [242-244]. Leveraging these types of imaging modalities in conjunction with wide-field optical imaging could provide important information concerning morphological changes related to circuit repair. Used in parallel with behavioral assays, microscopic imaging could be used to determine morphological changes in remapped circuits that were functionally adaptive, as well as those that were maladaptive. This information would both help to better characterize neural repair processes and provide targets for therapeutic and pharmacological intervention.

Furthermore, this experiment did not examine any molecular correlates of neural repair. I discussed several growth factors, like GAP43, BDNF, Arc, and GDF10, that are upregulated in stroke-affected circuits to promote dendritic spine turnover, axonal branching, and synaptogenesis in Section 3.1. Though upregulation of such factors in stroke affected circuits, including those undergoing functional remapping, offers therapeutic promise, we currently do not have any biomarkers of stroke available for use in clinical settings [245]. New methods of transcriptomics and multi-omics could provide great insight into alterations of transcriptome and proteome profiles in stroke-affected circuits in both animal models of stroke [123, 246, 247] and humans [123, 245, 248], and have potential to identify cellular and molecular targets to enhance plasticity after stroke. Used alongside a multimodal imaging approach consisting of wide-field optical imaging and two-photon microscopy, changes in expression of stroke-affected molecular targets identified in multi-omic approaches could be correlated with morphological changes observed in two-photon microscopy and mesoscopic spatial changes in neural circuits and networks after stroke, and manipulations of these targets may be able to improve neural repair and in turn functional outcomes.

Functional assessment in these stroke experiments is another factor limiting their strength. I used the cylinder rearing assay as a quantification of somatomotor function in mice after stroke, which tests the asymmetry of paw usage during exploratory rearing behavior in mice and rats. This test is simple to record and score, and requires no prior training for animals, but it quantifies function as a relative proportion, making it difficult to

isolate changes in somatomotor function of one paw and to separate somatosensory function from motor function. This can be troublesome in experiments such as those discussed in Chapter 4, as larger strokes can cause remapping of sensory function into contralesional somatosensory cortex and ipsilesional primary motor cortex. As such, it would be useful to employ additional assays to specifically quantify sensory function, like a pain threshold test, and motor function, like a pasta reaching test, unilaterally. In the case of larger strokes, assays to quantify higher order sensory integration functions may be more helpful behavioral correlates to network-level neural activity changes [249-251].

Although it has not yet been analyzed, hemodynamic data was also collected during the experiments of Chapter 4. This presents a whole new array of potential analyses to explore vascular repair and its relationship with neural repair after stroke. For instance, the temporal relationship between vascular repair and neural remapping is currently poorly understood, and data from these experiments could shed light on the time courses of these two types of repair. Additionally, longitudinal spatial changes in neurovascular coupling will be examined to determine whether changes in spatiotemporal parameters of coupling are predictive of functional recovery; spatial discrepancies between areas of hemodynamic activation and neural activation could inform maladaptive modes of repair. Likewise, disruptions in the dynamics of the hemodynamic response to neural activity may elucidate new patterns of neurovascular coupling that are associated with poor recovery.

Optical imaging has become a powerful tool to explore brain dynamics at multiple spatial and temporal levels, as well as their relationships with vascular activity. Multi-contrast optical imaging is a potent tool to study neurovascular coupling [252-254], and has been used to demonstrate associations between the changes in the strength of neurovascular coupling correlations and behavioral deficit after stroke [255]. Changes in neural activity in every frequency band measured by optical imaging have been correlated to recovery profiles, as well. To this end, it is crucial that we continue to develop these technologies, as they may serve as useful methods of clinical assessment. Yet, despite these technological advancements in the study of multiscale dynamics and neurovascular coupling, there is still far more that is unknown about these subjects than is known. Multimodal approaches to the study of neurovascular coupling and neural dynamics will likely prove the most effective at distinguishing the contributions of different molecular cascades, as well as the contributions of different cell-type-specific activity, to myriad neural and neurovascular processes. By improving our understanding of the mechanisms that direct these processes, we can transform our treatment of neurological and neurovascular disease.

References

1. Grinvald, A., et al., *Functional architecture of cortex revealed by optical imaging of intrinsic signals.* Nature, 1986. **324**(6095): p. 361-364.

2. Frostig, R.D., et al., *Cortical functional architecture and local coupling between neuronal activity and the microcirculation revealed by in vivo high-resolution optical imaging of intrinsic signals.* Proceedings of the National Academy of Sciences, 1990. **87**(16): p. 6082-6086.

3. Jöbsis, F.F., *Noninvasive, infrared monitoring of cerebral and myocardial oxygen sufficiency and circulatory parameters.* Science, 1977. **198**(4323): p. 1264-1267.

4. Malonek, D., et al., *Vascular imprints of neuronal activity: relationships between the dynamics of cortical blood flow, oxygenation, and volume changes following sensory stimulation.* Proceedings of the National Academy of Sciences, 1997. **94**(26): p. 14826-14831.

5. LaManna, J.C., et al., *Detection of an oxidizable fraction of cytochrome oxidase in intact rat brain.* American Journal of Physiology-Cell Physiology, 1987. **253**(3): p. C477-C483.

6. Jobsis, F.F., et al., *Reflectance spectrophotometry of cytochrome aa3 in vivo.* Journal of applied physiology, 1977. **43**(5): p. 858-872.

7. Wall, M.A., et al., *Metabolic imaging approaches: optical imaging.* Imaging and Metabolism, 2018: p. 99-126.

8. Georgakoudi, I. and K.P. Quinn, *Optical imaging using endogenous contrast to assess metabolic state.* Annual review of biomedical engineering, 2012. **14**: p. 351-367.

9. Walsh, A.J., R.S. Cook, and M.C. Skala, *Functional optical imaging of primary human tumor organoids: development of a personalized drug screen.* Journal of Nuclear Medicine, 2017. **58**(9): p. 1367-1372.

10. Nguyen, U., et al. *Optical imaging of zebrafish xenograft tumors for a high throughput drugs screen*. in *Multiscale Imaging and Spectroscopy II*. 2021. SPIE.

11. Cohen, L., et al., *Changes in axon fluorescence during activity: molecular probes of membrane potential.* The Journal of membrane biology, 1974. **19**: p. 1-36.

12. Lin, M.Z. and M.J. Schnitzer, *Genetically encoded indicators of neuronal activity.* Nature neuroscience, 2016. **19**(9): p. 1142.

13. Chen, T.-W., et al., *Ultrasensitive fluorescent proteins for imaging neuronal activity.* Nature, 2013. **499**(7458): p. 295-300.

14. Dana, H., et al., *Thy1-GCaMP6 transgenic mice for neuronal population imaging in vivo.* PloS one, 2014. **9**(9).

15. Meyer, H.S., et al., *Inhibitory interneurons in a cortical column form hot zones of inhibition in layers 2 and 5A.* Proceedings of the National Academy of Sciences, 2011. **108**(40): p. 16807-16812.

16. Chen, Q., et al., *Imaging neural activity using Thy1-GCaMP transgenic mice.* Neuron, 2012. **76**(2): p. 297-308.

17. Deng, X., et al., *Parvalbumin interneuron in the ventral hippocampus functions as a discriminator in social memory.* Proceedings of the National Academy of Sciences, 2019. **116**(33): p. 16583-16592.

18. Lee, A.T., et al., *VIP interneurons contribute to avoidance behavior by regulating information flow across hippocampal-prefrontal networks.* Neuron, 2019. **102**(6): p. 1223-1234. e4.

19. Murphy, M.C., et al., *Macroscale variation in resting-state neuronal activity and connectivity assessed by simultaneous calcium imaging, hemodynamic imaging and electrophysiology.* Neuroimage, 2018. **169**: p. 352-362.

20. Ma, Y., et al., *Wide-field optical mapping of neural activity and brain haemodynamics: considerations and novel approaches.* Philosophical Transactions of the Royal Society B: Biological Sciences, 2016. **371**(1705): p. 20150360.

21. White, B.R., et al., *Imaging of functional connectivity in the mouse brain.* PloS one, 2011. **6**(1): p. e16322.

22. Valley, M.T., et al., *Separation of hemodynamic signals from GCaMP fluorescence measured with wide-field imaging.* Journal of neurophysiology, 2020. **123**(1): p. 356-366.

23. Dana, H., et al., *Sensitive red protein calcium indicators for imaging neural activity.* elife, 2016. **5**: p. e12727.

24. Alexander-Bloch, A.F., et al., *The anatomical distance of functional connections predicts brain network topology in health and schizophrenia.* Cerebral cortex, 2013. **23**(1): p. 127-138.

25. Baldassarre, A., et al., *Brain connectivity and neurological disorders after stroke.* Current opinion in neurology, 2016. **29**(6): p. 706.

26. Bauer, A.Q., et al., *Optical imaging of disrupted functional connectivity following ischemic stroke in mice.* Neuroimage, 2014. **99**: p. 388-401.

27. Carter, A.R., et al., *Resting interhemispheric functional magnetic resonance imaging connectivity predicts performance after stroke.* Annals of neurology, 2010. **67**(3): p. 365-375.

28. Siegel, J.S., et al., *Disruptions of network connectivity predict impairment in multiple behavioral domains after stroke.* Proceedings of the National Academy of Sciences, 2016. **113**(30): p. E4367-E4376.

29. Mosso, A., *Ueber den Kreislauf des Blutes im menschlichen Gehirn*. 1881: Veit.

30. Roy, C.S. and C.S. Sherrington, *On the regulation of the blood-supply of the brain.* The Journal of physiology, 1890. **11**(1-2): p. 85.

31. Hoge, R.D., et al., *Linear coupling between cerebral blood flow and oxygen consumption in activated human cortex.* Proceedings of the National Academy of Sciences, 1999. **96**(16): p. 9403-9408.

32. Kim, S.G., et al., *Determination of relative CMRO2 from CBF and BOLD changes: significant increase of oxygen consumption rate during visual stimulation.* Magnetic Resonance in Medicine: An Official Journal of the International Society for Magnetic Resonance in Medicine, 1999. **41**(6): p. 1152-1161.

33. Devor, A., et al., *Frontiers in optical imaging of cerebral blood flow and metabolism.* Journal of Cerebral Blood Flow & Metabolism, 2012. **32**(7): p. 1259-1276.

34. Paulson, O.B., et al., *Cerebral blood flow response to functional activation.* Journal of Cerebral Blood Flow & Metabolism, 2010. **30**(1): p. 2-14.

35. Raichle, M.E. and M.A. Mintun, *Brain work and brain imaging.* Annu. Rev. Neurosci., 2006. **29**: p. 449-476.

36. Attwell, D., et al., *Glial and neuronal control of brain blood flow.* Nature, 2010. **468**(7321): p. 232-243.

37. Cauli, B. and E. Hamel, *Revisiting the role of neurons in neurovascular coupling.* Frontiers in neuroenergetics, 2010. **2**: p. 1661.

38. Lindquist, M.A., et al., *Modeling the hemodynamic response function in fMRI: efficiency, bias and mis-modeling.* Neuroimage, 2009. **45**(1): p. S187-S198.

39. Zambach, S.A., et al., *Precapillary sphincters and pericytes at first-order capillaries as key regulators for brain capillary perfusion.* Proceedings of the National Academy of Sciences, 2021. **118**(26): p. e2023749118.

40. Longden, T.A. and M.T. Nelson, *Vascular inward rectifier K+ channels as external K+ sensors in the control of cerebral blood flow.* Microcirculation, 2015. **22**(3): p. 183-196.

41. Girouard, H. and C. Iadecola, *Neurovascular coupling in the normal brain and in hypertension, stroke, and Alzheimer disease.* Journal of applied physiology, 2006. **100**(1): p. 328-335.

42. Iadecola, C., *The Neurovascular Unit Coming of Age: A Journey through Neurovascular Coupling in Health and Disease.* Neuron, 2017. **96**(1): p. 17-42.

43. Kisler, K., et al., *Cerebral blood flow regulation and neurovascular dysfunction in Alzheimer disease.* Nature Reviews Neuroscience, 2017. **18**(7): p. 419-434.

44. Montagne, A., et al., *Blood-brain barrier breakdown in the aging human hippocampus.* Neuron, 2015. **85**(2): p. 296-302.

45. Toledo, J.B., et al., *Contribution of cerebrovascular disease in autopsy confirmed neurodegenerative disease cases in the National Alzheimer's Coordinating Centre.* Brain, 2013. **136**(9): p. 2697-2706.

46. Winkler, E.A., et al., *Blood–spinal cord barrier breakdown and pericyte reductions in amyotrophic lateral sclerosis.* Acta neuropathologica, 2013. **125**: p. 111-120.

47. Kortekaas, R., et al., *Blood–brain barrier dysfunction in parkinsonian midbrain in vivo.* Annals of neurology, 2005. **57**(2): p. 176-179.

48. Kazama, K., et al., *Angiotensin II attenuates functional hyperemia in the mouse somatosensory cortex.* American Journal of Physiology-Heart and Circulatory Physiology, 2003. **285**(5): p. H1890-H1899.

49. Blicher, J.U., et al., *Visualization of altered neurovascular coupling in chronic stroke patients using multimodal functional MRI.* J Cereb Blood Flow Metab, 2012. **32**(11): p. 2044-54.

50. Iadecola, C., *Cerebral circulatory dysregulation in ischemia.* Cerebrovascular diseases, 1998. **1**: p. 319-332.

51. Salinet, A.S., T.G. Robinson, and R.B. Panerai, *Effects of cerebral ischemia on human neurovascular coupling, CO2 reactivity, and dynamic cerebral autoregulation.* Journal of Applied Physiology, 2015. **118**(2): p. 170-177.

52. Logothetis, N.K., *What we can do and what we cannot do with fMRI.* Nature, 2008. **453**(7197): p. 869-878.

53. Brownstein, C.A., et al., *Mutation of KCNJ8 in a patient with Cantu syndrome with unique vascular abnormalities–support for the role of K (ATP) channels in this condition.* European journal of medical genetics, 2013. **56**(12): p. 678-682.

54. Cooper, P.E., et al., *Cantú Syndrome Resulting from Activating Mutation in the KCNJ 8 Gene.* Human mutation, 2014. **35**(7): p. 809-813.

55. Harakalova, M., et al., *Dominant missense mutations in ABCC9 cause Cantu syndrome.* Nature genetics, 2012. **44**(7): p. 793-796.

56. Van Bon, B.W., et al., *Cantu syndrome is caused by mutations in ABCC9.* The American Journal of Human Genetics, 2012. **90**(6): p. 1094-1101.

57. Huang, Y., et al., *Cardiovascular consequences of KATP overactivity in Cantu syndrome.* JCI insight, 2018. **3**(15).

58. Nichols, C.G., G.K. Singh, and D.K. Grange, *KATP channels and cardiovascular disease: suddenly a syndrome.* Circulation research, 2013. **112**(7): p. 1059-1072.

59. Girouard, H. and C. Iadecola, *Neurovascular coupling in the normal brain and in hypertension, stroke, and Alzheimer disease.* J Appl Physiol (1985), 2006. **100**(1): p. 328-35.

60. Longden, T.A., et al., *Pericytes and the Control of Blood Flow in Brain and Heart.* Annu Rev Physiol, 2023. **85**: p. 137-164.

61. Zambach, S.A., et al., *Precapillary sphincters and pericytes at first-order capillaries as key regulators for brain capillary perfusion.* Proc Natl Acad Sci U S A, 2021. **118**(26).

62. Longden, T.A. and M.T. Nelson, *Vascular inward rectifier K+ channels as external K+ sensors in the control of cerebral blood flow.* Microcirculation, 2015. **22**(3): p. 183-96.

63. Longden, T.A., et al., *Capillary K(+)-sensing initiates retrograde hyperpolarization to increase local cerebral blood flow.* Nature Neuroscience, 2017. **20**(5): p. 717-726.

64. Hariharan, A., et al., *Brain capillary pericytes are metabolic sentinels that control blood flow through a K(ATP) channel-dependent energy switch.* Cell Rep, 2022. **41**(13): p. 111872.

65. Wells, J.A., et al., *A critical role for purinergic signalling in the mechanisms underlying generation of BOLD fMRI responses.* J Neurosci, 2015. **35**(13): p. 5284-92.

66. Nichols, C.G., *KATP channels as molecular sensors of cellular metabolism.* Nature, 2006. **440**: p. 471-476.

67. Inagaki, N., et al., *A family of sulfonylurea receptors determines the pharmacological properties of ATP-sensitive K+ channels.* Neuron, 1996. **16**(5): p. 1011-7.

68. Flagg, T.P., et al., *Muscle KATP channels: recent insights to energy sensing and myoprotection.* Physiol Rev, 2010. **90**(3): p. 799-829.

69. Huang, Y., et al., *Cardiovascular consequences of KATP overactivity in Cantu syndrome.* JCI insight, 2018. **3**(15).

70. Aziz, Q., et al., *The ATP-sensitive potassium channel subunit, Kir6.1, in vascular smooth muscle plays a major role in blood pressure control.* Hypertension, 2014. **64**(3): p. 523-9.

71. Li, A., et al., *Hypotension due to Kir6.1 gain-of-function in vascular smooth muscle.* J Am Heart Assoc, 2013. **2**(4): p. e000365.

72. Suzuki, M., et al., *Functional roles of cardiac and vascular ATP-sensitive potassium channels clarified by Kir6.2-knockout mice.* Circ Res, 2001. **88**(6): p. 570-7.

73. Sancho, M., et al., *Adenosine signaling activates ATP-sensitive K(+) channels in endothelial cells and pericytes in CNS capillaries.* Sci Signal, 2022. **15**(727): p. eabl5405.

74. Ando, K., et al., *KCNJ8/ABCC9-containing K-ATP channel modulates brain vascular smooth muscle development and neurovascular coupling.* Dev Cell, 2022. **57**(11): p. 1383-1399 e7.

75. Smeland, M.F., et al., *ABCC9-related Intellectual disability Myopathy Syndrome is a KATP channelopathy with loss-of-function mutations in ABCC9.* Nature communications, 2019. **10**(1): p. 4457.

76. Grange, D.K., et al., *Cantu syndrome: Findings from 74 patients in the International Cantu Syndrome Registry.* American journal of medical genetics. Part C, Seminars in medical genetics, 2019. **181**(4): p. 658-681.

77. Cooper, P.E., et al., *Cantu syndrome resulting from activating mutation in the KCNJ8 gene.* Hum Mutat, 2014. **35**(7): p. 809-13.

78. Leon Guerrero, C.R., et al., *Neurologic and neuroimaging manifestations of Cantu syndrome: A case series.* Neurology, 2016. **87**(3): p. 270-6.

79. Al-Karagholi, M.A., et al., *Opening of ATP-sensitive potassium channels causes migraine attacks: a new target for the treatment of migraine.* Brain, 2019. **142**(9): p. 2644-2654.

80. Brownstein, C.A., et al., *Mutation of KCNJ8 in a patient with Cantu syndrome with unique vascular abnormalities - support for the role of K(ATP) channels in this condition.* European journal of medical genetics, 2013. **56**(12): p. 678-82.

81. Albertson, A.J., et al., *Normal aging in mice is associated with a global reduction in cortical spectral power and network-specific declines in functional connectivity.* Neuroimage, 2022. **257**: p. 119287.

82. Rosenthal, Z.P., et al., *Local Perturbations of Cortical Excitability Propagate Differentially Through Large-Scale Functional Networks.* Cereb Cortex, 2020. **30**(5): p. 3352-3369.

83. Wright, P.W., et al., *Functional connectivity structure of cortical calcium dynamics in anesthetized and awake mice.* PLoS One, 2017. **12**(10): p. e0185759.

84. Bauer, A.Q., et al., *Effective Connectivity Measured Using Optogenetically Evoked Hemodynamic Signals Exhibits Topography Distinct from Resting State Functional Connectivity in the Mouse.* Cereb Cortex, 2018. **28**(1): p. 370-386.

85. Ma, Y., et al., *Resting-state hemodynamics are spatiotemporally coupled to synchronized and symmetric neural activity in excitatory neurons.* Proc Natl Acad Sci U S A, 2016. **113**(52): p. E8463-E8471.

86. White, B.R., et al., *Imaging of functional connectivity in the mouse brain.* PLoS One, 2011. **6**(1): p. e16322.

87. Padawer-Curry, J.A., et al., *Wide-Field Optical Imaging in Mouse Models of Ischemic Stroke.* Methods Mol Biol, 2023. **2616**: p. 113-151.

88. Zhu, X., D.E. Bergles, and A. Nishiyama, *NG2 cells generate both oligodendrocytes and gray matter astrocytes.* Development, 2008. **135**(1): p. 145-57.

89. Adebiyi, A., E.M. McNally, and J.H. Jaggar, *Vasodilation induced by oxygen/glucose deprivation is attenuated in cerebral arteries of SUR2 null mice.* Am J Physiol Heart Circ Physiol, 2011. **301**(4): p. H1360-8.

90. Grange, D.K., C.G. Nichols, and G.K. Singh, *Cantu Syndrome and Related Disorders*, in *GeneReviews(R)*, R.A. Pagon, et al., Editors. 2014: Seattle (WA).

91. Nichols, C.G., *Personalized Therapeutics for K(ATP)-Dependent Pathologies.* Annu Rev Pharmacol Toxicol, 2023. **63**: p. 541-563.

92. Kokoti, L., M.A. Al-Karagholi, and M. Ashina, *Latest Insights into the Pathophysiology of Migraine: the ATP-Sensitive Potassium Channels.* Curr Pain Headache Rep, 2020. **24**(12): p. 77.

93. Clement, A., et al., *ATP-Sensitive Potassium Channels in Migraine: Translational Findings and Therapeutic Potential.* Cells, 2022. **11**(15).

94. York, N.W., et al., *Kir6.1- and SUR2-dependent KATP over-activity disrupts intestinal motility in murine models of Cantu Syndrome.* JCI Insight, 2020.

95. Uhlirova, H., et al., *Cell type specificity of neurovascular coupling in cerebral cortex.* Elife, 2016. **5**.

96. Lee, L., et al., *Key Aspects of Neurovascular Control Mediated by Specific Populations of Inhibitory Cortical Interneurons.* Cereb Cortex, 2020. **30**(4): p. 2452-2464.

97. Lee, J., et al., *Opposed hemodynamic responses following increased excitation and parvalbumin-based inhibition.* J Cereb Blood Flow Metab, 2021. **41**(4): p. 841-856.

98. Nelson, M.T., et al., *Calcium channels, potassium channels, and voltage dependence of arterial smooth muscle tone.* Am J Physiol, 1990. **259**(1 Pt 1): p. C3-18.

99. Lopatin, A.N., E.N. Makhina, and C.G. Nichols, *The mechanism of inward rectification of potassium channels: "long-pore plugging" by cytoplasmic polyamines.* Journal of General Physiology, 1995. **106**(5): p. 923-55.

100. Nelson, P.T., et al., *ABCC9/SUR2 in the brain: Implications for hippocampal sclerosis of aging and a potential therapeutic target.* Ageing Res Rev, 2015. **24**(Pt B): p. 111-25.

101. Sakura, H., et al., *Altered functional properties of KATP channel conferred by a novel splice variant of SUR1.* J Physiol, 1999. **521 Pt 2**: p. 337-50.

102. Nelson, P.T., et al., *Novel human ABCC9/SUR2 brain-expressed transcripts and an eQTL relevant to hippocampal sclerosis of aging.* Journal of Neurochemistry, 2015. **134**(6): p. 1026-39.

103. Nelson, P.T., et al., *Reassessment of risk genotypes (GRN, TMEM106B, and ABCC9 variants) associated with hippocampal sclerosis of aging pathology.* J Neuropathol Exp Neurol, 2015. **74**(1): p. 75-84.

104. Montine, T.J., et al., *National Institute on Aging-Alzheimer's Association guidelines for the neuropathologic assessment of Alzheimer's disease: a practical approach.* Acta Neuropathol, 2012. **123**(1): p. 1-11.

105. Nelson, P.T., et al., *ABCC9/SUR2 in the brain: Implications for hippocampal sclerosis of aging and a potential therapeutic target.* Ageing research reviews, 2015. **24**(Pt B): p. 111-25.

106. Rossini, P., et al., *Does cerebrovascular disease affect the coupling between neuronal activity and local haemodynamics?* Brain, 2004. **127**(1): p. 99-110.

107. Tsao, C.W., et al., *Heart disease and stroke statistics—2023 update: a report from the American Heart Association.* Circulation, 2023. **147**(8): p. e93-e621.

108. Cramer, S.C., *Repairing the human brain after stroke: I. Mechanisms of spontaneous recovery.* Annals of neurology, 2008. **63**(3): p. 272-287.

109. Duncan, P.W., et al., *Measurement of motor recovery after stroke. Outcome assessment and sample size requirements.* Stroke, 1992. **23**(8): p. 1084-1089.

110. Hermann, D.M. and M. Chopp, *Promoting brain remodelling and plasticity for stroke recovery: therapeutic promise and potential pitfalls of clinical translation.* Lancet Neurol, 2012. **11**(4): p. 369-80.

111. Jones, T.A. and D.L. Adkins, *Motor System Reorganization After Stroke: Stimulating and Training Toward Perfection.* Physiology (Bethesda), 2015. **30**(5): p. 358-70.

112. Sanchez-Mendoza, E.H. and D.M. Hermann, *Correlates of post-stroke brain plasticity, relationship to pathophysiological settings and implications for human proof-of-concept studies.* Frontiers in cellular neuroscience, 2016. **10**: p. 196.

113. Skilbeck, C.E., et al., *Recovery after stroke.* J Neurol Neurosurg Psychiatry, 1983. **46**(1): p. 5-8.

114. Teasell, R., N.A. Bayona, and J. Bitensky, *Plasticity and reorganization of the brain post stroke.* Top Stroke Rehabil, 2005. **12**(3): p. 11-26.

115. Zeiler, S.R. and J.W. Krakauer, *The interaction between training and plasticity in the post-stroke brain.* Current opinion in neurology, 2013. **26**(6): p. 609.

116. Zhang, R.L., Z.G. Zhang, and M. Chopp, *Ischemic stroke and neurogenesis in the subventricular zone.* Neuropharmacology, 2008. **55**(3): p. 345-352.

117. Ohab, J.J., et al., *A neurovascular niche for neurogenesis after stroke.* Journal of Neuroscience, 2006. **26**(50): p. 13007-13016.

118. Wang, L., et al., *Treatment of stroke with erythropoietin enhances neurogenesis and angiogenesis and improves neurological function in rats.* Stroke, 2004. **35**(7): p. 1732-1737.

119. Li, S., et al., *An age-related sprouting transcriptome provides molecular control of axonal sprouting after stroke.* Nature neuroscience, 2010. **13**(12): p. 1496.

120. Li, S., et al., *GDF10 is a signal for axonal sprouting and functional recovery after stroke.* Nature neuroscience, 2015. **18**(12): p. 1737-1745.

121. Murphy, T.H. and D. Corbett, *Plasticity during stroke recovery: from synapse to behaviour.* Nat Rev Neurosci, 2009. **10**(12): p. 861-72.

122. Carmichael, S.T. and M.-F. Chesselet, *Synchronous neuronal activity is a signal for axonal sprouting after cortical lesions in the adult.* Journal of Neuroscience, 2002. **22**(14): p. 6062-6070.

123. Buga, A.M., et al., *Transcriptomics of post-stroke angiogenesis in the aged brain.* Frontiers in aging neuroscience, 2014. **6**: p. 44.

124. Santos, G.L., et al., *Decreased brain-derived neurotrophic factor serum concentrations in chronic post-stroke subjects.* Journal of Stroke and Cerebrovascular Diseases, 2016. **25**(12): p. 2968-2974.

125. Carmichael, S.T., et al., *Growth-associated gene expression after stroke: evidence for a growth-promoting region in peri-infarct cortex.* Experimental neurology, 2005. **193**(2): p. 291-311.

126. Stroemer, R.P., T.A. Kent, and C.E. Hulsebosch, *Neocortical neural sprouting, synaptogenesis, and behavioral recovery after neocortical infarction in rats.* Stroke, 1995. **26**(11): p. 2135-2144.

127. Bolaños, J.P., et al., *Mitochondria and reactive oxygen and nitrogen species in neurological disorders and stroke: therapeutic implications.* Advanced drug delivery reviews, 2009. **61**(14): p. 1299-1315.

128. Hayakawa, K., et al., *Transfer of mitochondria from astrocytes to neurons after stroke.* Nature, 2016. **535**(7613): p. 551-555.

129. Sims, N.R. and H. Muyderman, *Mitochondria, oxidative metabolism and cell death in stroke.* Biochimica et Biophysica Acta (BBA)-Molecular Basis of Disease, 2010. **1802**(1): p. 80-91.

130. Domann, R., et al., *Electrophysiological changes in the surrounding brain tissue of photochemically induced cortical infarcts in the rat.* Neuroscience letters, 1993. **155**(1): p. 69-72.

131. Hagemann, G., et al., *Increased long-term potentiation in the surround of experimentally induced focal cortical infarction.* Annals of Neurology: Official Journal of the American Neurological Association and the Child Neurology Society, 1998. **44**(2): p. 255-258.

132. Witte, O.W., et al., *Functional differentiation of multiple perilesional zones after focal cerebral ischemia.* Journal of Cerebral Blood Flow & Metabolism, 2000. **20**(8): p. 1149-1165.

133. Buchkremer-Ratzmann, I., et al., *Electrophysiological transcortical diaschisis after cortical photothrombosis in rat brain.* Stroke, 1996. **27**(6): p. 1105-1111.

134. Obi, K., I. Amano, and Y. Takatsuru, *Role of dopamine on functional recovery in the contralateral hemisphere after focal stroke in the somatosensory cortex.* Brain research, 2018. **1678**: p. 146-152.

135. Witte, O.W. and G. Stoll, *Delayed and remote effects of focal cortical infarctions: secondary damage and reactive plasticity.* Advances in neurology, 1997. **73**: p. 207-227.

136. Dancause, N., et al., *Extensive cortical rewiring after brain injury.* Journal of Neuroscience, 2005. **25**(44): p. 10167-10179.

137. Silasi, G. and T.H. Murphy, *Stroke and the connectome: how connectivity guides therapeutic intervention.* Neuron, 2014. **83**(6): p. 1354-1368.

138. Brown, C.E., J.D. Boyd, and T.H. Murphy, *Longitudinal in vivo imaging reveals balanced and branch-specific remodeling of mature cortical pyramidal dendritic arbors after stroke.* Journal of Cerebral Blood Flow & Metabolism, 2010. **30**(4): p. 783-791.

139. Brown, C.E., et al., *Extensive turnover of dendritic spines and vascular remodeling in cortical tissues recovering from stroke.* Journal of Neuroscience, 2007. **27**(15): p. 4101-4109.

140. Brown, C.E. and T.H. Murphy, *Livin'on the edge: imaging dendritic spine turnover in the peri-infarct zone during ischemic stroke and recovery.* The Neuroscientist, 2008. **14**(2): p. 139-146.

141. Brown, C.E., C. Wong, and T.H. Murphy, *Rapid morphologic plasticity of peri-infarct dendritic spines after focal ischemic stroke.* Stroke, 2008. **39**(4): p. 1286-1291.

142. Li, P. and T.H. Murphy, *Two-photon imaging during prolonged middle cerebral artery occlusion in mice reveals recovery of dendritic structure after reperfusion.* Journal of Neuroscience, 2008. **28**(46): p. 11970-11979.

143. Liauw, J., et al., *Thrombospondins 1 and 2 are necessary for synaptic plasticity and functional recovery after stroke.* Journal of Cerebral Blood Flow & Metabolism, 2008. **28**(10): p. 1722-1732.

144. Korb, E. and S. Finkbeiner, *Arc in synaptic plasticity: from gene to behavior.* Trends in neurosciences, 2011. **34**(11): p. 591-598.

145. Rickhag, M., M. Teilum, and T. Wieloch, *Rapid and long-term induction of effector immediate early genes (BDNF, Neuritin and Arc) in peri-infarct cortex and dentate gyrus after ischemic injury in rat brain.* Brain research, 2007. **1151**: p. 203-210.

146. Comelli, M., et al., *Time course, localization and pharmacological modulation of immediate early inducible genes, brain-derived neurotrophic factor and trkB messenger RNAs in the rat brain following photochemical stroke.* Neuroscience, 1993. **55**(2): p. 473-490.

147. Calautti, C. and J.-C. Baron, *Functional neuroimaging studies of motor recovery after stroke in adults: a review.* Stroke, 2003. **34**(6): p. 1553-1566.

148. Dijkhuizen, R.M., et al., *Functional magnetic resonance imaging of reorganization in rat brain after stroke.* Proceedings of the National Academy of Sciences, 2001. **98**(22): p. 12766-12771.

149. Cramer, S.C., et al., *Activity in the peri-infarct rim in relation to recovery from stroke.* Stroke, 2006. **37**(1): p. 111-115.

150. Abo, M., et al., *Functional recovery after brain lesion—contralateral neuromodulation: an fMRI study.* Neuroreport, 2001. **12**(7): p. 1543-1547.

151. Biernaskie, J., et al., *Bi-hemispheric contribution to functional motor recovery of the affected forelimb following focal ischemic brain injury in rats.* European Journal of Neuroscience, 2005. **21**(4): p. 989-999.

152. Cramer, S.C. and K.R. Crafton, *Somatotopy and movement representation sites following cortical stroke.* Experimental brain research, 2006. **168**: p. 25-32.

153. Ward, N., et al., *Neural correlates of motor recovery after stroke: a longitudinal fMRI study.* Brain, 2003. **126**(11): p. 2476-2496.

154. Desowska, A. and D.L. Turner, *Dynamics of brain connectivity after stroke.* Reviews in the Neurosciences, 2019. **30**(6): p. 605-623.

155. Grefkes, C. and G.R. Fink, *Reorganization of cerebral networks after stroke: new insights from neuroimaging with connectivity approaches.* Brain, 2011. **134**(5): p. 1264-1276.

156. Corbetta, M., *Functional connectivity and neurological recovery.* Developmental psychobiology, 2012. **54**(3): p. 239-253.

157. Van Meer, M.P., et al., *Recovery of sensorimotor function after experimental stroke correlates with restoration of resting-state interhemispheric functional connectivity.* Journal of Neuroscience, 2010. **30**(11): p. 3964-3972.

158. Westlake, K.P. and S.S. Nagarajan, *Functional connectivity in relation to motor performance and recovery after stroke.* Frontiers in systems neuroscience, 2011. **5**: p. 8.

159. Lim, D.H., et al., *Optogenetic mapping after stroke reveals network-wide scaling of functional connections and heterogeneous recovery of the peri-infarct.* Journal of Neuroscience, 2014. **34**(49): p. 16455-16466.

160. Schaechter, J.D., et al., *Structural and functional plasticity in the somatosensory cortex of chronic stroke patients.* Brain, 2006. **129**(10): p. 2722-2733.

161. Schaechter, J.D., et al., *Increase in sensorimotor cortex response to somatosensory stimulation over subacute poststroke period correlates with motor recovery in hemiparetic patients.* Neurorehabilitation and Neural Repair, 2012. **26**(4): p. 325-334.

162. Grefkes, C., et al., *Cortical connectivity after subcortical stroke assessed with functional magnetic resonance imaging.* Annals of neurology, 2008. **63**(2): p. 236-246.

163. Rehme, A.K., et al., *Dynamic causal modeling of cortical activity from the acute to the chronic stage after stroke.* Neuroimage, 2011. **55**(3): p. 1147-1158.

164. Rehme, A.K., et al., *The role of the contralesional motor cortex for motor recovery in the early days after stroke assessed with longitudinal FMRI.* Cerebral cortex, 2011. **21**(4): p. 756-768.

165. Gonzalez, C.L., et al., *Evidence for bilateral control of skilled movements: ipsilateral skilled forelimb reaching deficits and functional recovery in rats follow motor cortex and lateral frontal cortex lesions.* European Journal of Neuroscience, 2004. **20**(12): p. 3442-3452.

166. Kitsos, G.H., et al., *The ipsilesional upper limb can be affected following stroke.* The Scientific World Journal, 2013. **2013**.

167. Desrosiers, J., et al., *Performance of the 'unaffected'upper extremity of elderly stroke patients.* Stroke, 1996. **27**(9): p. 1564-1570.

168. Damoiseaux, J.S. and M.D. Greicius, *Greater than the sum of its parts: a review of studies combining structural connectivity and resting-state functional connectivity.* Brain Structure and Function, 2009. **213**(6): p. 525-533.

169. Friston, K.J., *Functional and effective connectivity in neuroimaging: a synthesis.* Human brain mapping, 1994. **2**(1-2): p. 56-78.

170. Hakon, J., et al., *Multisensory stimulation improves functional recovery and resting-state functional connectivity in the mouse brain after stroke.* Neuroimage Clin, 2018. **17**: p. 717-730.

171. Rosenthal, Z.P., et al., *Local Perturbations of Cortical Excitability Propagate Differentially Through Large-Scale Functional Networks.* Cerebral Cortex, 2020. **30**(5): p. 3352-3369.

172. Kraft, A.W., et al., *Sensory deprivation after focal ischemia in mice accelerates brain remapping and improves functional recovery through Arc-dependent synaptic plasticity.* Science translational medicine, 2018. **10**(426): p. eaag1328.

173. Schallert, T., et al., *CNS plasticity and assessment of forelimb sensorimotor outcome in unilateral rat models of stroke, cortical ablation, parkinsonism and spinal cord injury.* Neuropharmacology, 2000. **39**(5): p. 777-787.

174. Rosenthal, Z.P., et al., *Peripheral sensory stimulation elicits global slow waves by recruiting somatosensory cortex bilaterally.* Proceedings of the National Academy of Sciences, 2021. **118**(8): p. e2021252118.

175. Ma, Y., et al., *Resting-state hemodynamics are spatiotemporally coupled to synchronized and symmetric neural activity in excitatory neurons.* Proceedings of the National Academy of Sciences, 2016. **113**(52): p. E8463-E8471.

176. Team, R.C., *R: A language and environment for statistical computing. R Foundation for Statistical Computing.* (No Title), 2013.

177. Fox, J. and S. Weisberg, *An {R} companion to applied regression 3rd ed Sage Thousand Oaks*. 2019, CA.

178. Imai, K., L. Keele, and T. Yamamoto, *Identification, inference and sensitivity analysis for causal mediation effects.* 2010.

179. Tingley, D., et al., *Mediation: R package for causal mediation analysis.* 2014.

180. Dana, H., et al., *Thy1-GCaMP6 transgenic mice for neuronal population imaging in vivo.* PloS one, 2014. **9**(9): p. e108697.

181. Brown, C.E., et al., *In vivo voltage-sensitive dye imaging in adult mice reveals that somatosensory maps lost to stroke are replaced over weeks by new structural and functional circuits with prolonged modes of activation within both the peri-infarct zone and distant sites.* Journal of Neuroscience, 2009. **29**(6): p. 1719-1734.

182. Rogers, D.C., et al., *Correlation between motor impairment and infarct volume after permanent and transient middle cerebral artery occlusion in the rat.* Stroke, 1997. **28**(10): p. 2060-2066.

183. Saunders, D.E., A.G. Clifton, and M.M. Brown, *Measurement of infarct size using MRI predicts prognosis in middle cerebral artery infarction.* Stroke, 1995. **26**(12): p. 2272-2276.

184. Sperber, C., et al., *Stroke lesion size–Still a useful biomarker for stroke severity and outcome in times of high-dimensional models.* NeuroImage: Clinical, 2023. **40**: p. 103511.

185. He, F., et al., *Multimodal mapping of neural activity and cerebral blood flow reveals long-lasting neurovascular dissociations after small-scale strokes.* Science advances, 2020. **6**(21): p. eaba1933.

186. Kokinovic, B. and P. Medini, *Loss of GABAB-mediated interhemispheric synaptic inhibition in stroke periphery.* The Journal of physiology, 2018. **596**(10): p. 1949-1964.

187. Tennant, K.A., et al., *Optogenetic rewiring of thalamocortical circuits to restore function in the stroke injured brain.* Nature communications, 2017. **8**(1): p. 15879.

188. Jablonka, J., et al., *Remapping of the somatosensory cortex after a photothrombotic stroke: dynamics of the compensatory reorganization.* Neuroscience, 2010. **165**(1): p. 90-100.

189. Chmayssani, M., et al., *Reperfusion normalizes motor activation patterns in large-vessel disease.* Annals of Neurology: Official Journal of the American

Neurological Association and the Child Neurology Society, 2009. **65**(2): p. 203-208.

190. Choi, B.-i., et al., *Neurobehavioural deficits correlate with the cerebral infarction volume of stroke animals: a comparative study on ischaemia-reperfusion and photothrombosis models.* Environmental Toxicology and Pharmacology, 2012. **33**(1): p. 60-69.

191. Li, C.X. and R.S. Waters, *In vivo intracellular recording and labeling of neurons in the forepaw barrel subfield (FBS) of rat somatosensory cortex: possible physiological and morphological substrates for reorganization.* Neuroreport, 1996. **7**(14): p. 2261-2276.

192. Zarzecki, P., et al., *Synaptic mechanisms of cortical representational plasticity: somatosensory and corticocortical EPSPs in reorganized raccoon SI cortex.* Journal of neurophysiology, 1993. **69**(5): p. 1422-1432.

193. Ferezou, I., et al., *Spatiotemporal dynamics of cortical sensorimotor integration in behaving mice.* Neuron, 2007. **56**(5): p. 907-923.

194. Sigler, A., M.H. Mohajerani, and T.H. Murphy, *Imaging rapid redistribution of sensory-evoked depolarization through existing cortical pathways after targeted stroke in mice.* Proceedings of the National Academy of Sciences, 2009. **106**(28): p. 11759-11764.

195. Cramer, S.C., et al., *A functional MRI study of subjects recovered from hemiparetic stroke.* Stroke, 1997. **28**(12): p. 2518-2527.

196. Liepert, J., et al., *Motor cortex disinhibition in acute stroke.* Clinical Neurophysiology, 2000. **111**(4): p. 671-676.

197. Shimizu, T., et al., *Motor cortical disinhibition in the unaffected hemisphere after unilateral cortical stroke.* Brain, 2002. **125**(8): p. 1896-1907.

198. Starkstein, S.E. and R.G. Robinson, *Mechanism of disinhibition after brain lesions.* The Journal of nervous and mental disease, 1997. **185**(2): p. 108-114.

199. Dijkhuizen, R.M., et al., *Correlation between brain reorganization, ischemic damage, and neurologic status after transient focal cerebral ischemia in rats: a functional magnetic resonance imaging study.* Journal of Neuroscience, 2003. **23**(2): p. 510-517.

200. Harris, N., et al., *Disconnection and hyper-connectivity underlie reorganization after TBI: a rodent functional connectomic analysis.* Experimental neurology, 2016. **277**: p. 124-138.

201. Buzsáki, G., et al., *Interneuron diversity series: circuit complexity and axon wiring economy of cortical interneurons.* Trends in neurosciences, 2004. **27**(4): p. 186-193.

202. Jessen, S.B., et al., *Interneuron deficit associates attenuated network synchronization to mismatch of energy supply and demand in aging mouse brains.* Cerebral Cortex, 2017. **27**(1): p. 646-659.

203. Wu, W., et al., *Impaired neuronal synchrony after focal ischemic stroke in elderly patients.* Clinical Neurophysiology, 2011. **122**(1): p. 21-26.

204. Fetz, E. *Correlational strength and computational algebra of synaptic connections between neurons*. in *Neural Information Processing Systems*. 1987.

205. Butts, D.A. and M.S. Goldman, *Tuning curves, neuronal variability, and sensory coding.* PLoS biology, 2006. **4**(4): p. e92.

206. Carandini, M. and D. Ferster, *Membrane potential and firing rate in cat primary visual cortex.* Journal of Neuroscience, 2000. **20**(1): p. 470-484.

207. Greicius, M.D., et al., *Resting-state functional connectivity reflects structural connectivity in the default mode network.* Cerebral cortex, 2009. **19**(1): p. 72-78.

208. Huang, H. and M. Ding, *Linking functional connectivity and structural connectivity quantitatively: a comparison of methods.* Brain connectivity, 2016. **6**(2): p. 99-108.

209. Bastos, A.M. and J.-M. Schoffelen, *A tutorial review of functional connectivity analysis methods and their interpretational pitfalls.* Frontiers in systems neuroscience, 2016. **9**: p. 175.

210. Chen, J.Y., et al., *Interneuron-mediated inhibition synchronizes neuronal activity during slow oscillation.* The Journal of physiology, 2012. **590**(16): p. 3987-4010.

211. Aziz, Q., et al., *The ATP-sensitive potassium channel subunit, Kir6. 1, in vascular smooth muscle plays a major role in blood pressure control.* Hypertension, 2014. **64**(3): p. 523-529.

212. Flagg, T.P., et al., *Muscle KATP channels: recent insights to energy sensing and myoprotection.* Physiological reviews, 2010. **90**(3): p. 799-829.

213. Hamilton, N.B., D. Attwell, and C.N. Hall, *Pericyte-mediated regulation of capillary diameter: a component of neurovascular coupling in health and disease.* Frontiers in neuroenergetics, 2010. **2**: p. 1453.

214. Chasseigneaux, S., et al., *Isolation and differential transcriptome of vascular smooth muscle cells and mid-capillary pericytes from the rat brain.* Scientific reports, 2018. **8**(1): p. 12272.

215. He, L., et al., *Analysis of the brain mural cell transcriptome.* Scientific reports, 2016. **6**(1): p. 35108.

216. Sancho, M., et al., *Adenosine signaling activates ATP-sensitive K+ channels in endothelial cells and pericytes in CNS capillaries.* Science signaling, 2022. **15**(727): p. eabl5405.

217. Hillman, E.M., et al., *Depth-resolved optical imaging and microscopy of vascular compartment dynamics during somatosensory stimulation.* Neuroimage, 2007. **35**(1): p. 89-104.

218. Matsuura, T., et al., *CBF change evoked by somatosensory activation measured by laser-Doppler flowmetry: independent evaluation of RBC velocity and RBC concentration.* The Japanese journal of physiology, 1999. **49**(3): p. 289-296.

219. Vanzetta, I., R. Hildesheim, and A. Grinvald, *Compartment-resolved imaging of activity-dependent dynamics of cortical blood volume and oximetry.* Journal of Neuroscience, 2005. **25**(9): p. 2233-2244.

220. Stallcup, W.B., *The NG2 proteoglycan in pericyte biology.* Pericyte Biology-Novel Concepts, 2018: p. 5-19.

221. Guo, X., et al., *Atp13a5 marker reveals pericytes of the central nervous system in mice.* Biorxiv, 2021: p. 2021.07. 09.451694.

222. Li, L., et al., *Expression of the SM22alpha promoter in transgenic mice provides evidence for distinct transcriptional regulatory programs in vascular and visceral smooth muscle cells.* The Journal of cell biology, 1996. **132**(5): p. 849-859.

223. Moessler, H., et al., *The SM 22 promoter directs tissue-specific expression in arterial but not in venous or visceral smooth muscle cells in transgenic mice.* Development, 1996. **122**(8): p. 2415-2425.

224. Forde, A., et al., *Temporal Cre-mediated recombination exclusively in endothelial cells using Tie2 regulatory elements.* genesis, 2002. **33**(4): p. 191-197.

225. Kisanuki, Y.Y., et al., *Tie2-Cre transgenic mice: a new model for endothelial cell-lineage analysis in vivo.* Developmental biology, 2001. **230**(2): p. 230-242.

226. Anghelina, M., L. Moldovan, and N.I. Moldovan, *Preferential activity of Tie2 promoter in arteriolar endothelium.* Journal of cellular and molecular medicine, 2005. **9**(1): p. 113-121.

227. Smeland, M.F., et al., *ABCC9-related Intellectual disability Myopathy Syndrome is a KATP channelopathy with loss-of-function mutations in ABCC9.* Nature communications, 2019. **10**(1): p. 4457.

228. Nelson, P.T., et al., *Reassessment of risk genotypes (GRN, TMEM106B, and ABCC9 variants) associated with hippocampal sclerosis of aging pathology.* Journal of Neuropathology & Experimental Neurology, 2015. **74**(1): p. 75-84.

229. Nelson, P.T., et al., *Novel human ABCC9/SUR2 brain-expressed transcripts and an eQTL relevant to hippocampal sclerosis of aging.* Journal of neurochemistry, 2015. **134**(6): p. 1026-1039.

230. Montine, T.J., et al., *National Institute on Aging–Alzheimer's Association guidelines for the neuropathologic assessment of Alzheimer's disease: a practical approach.* Acta neuropathologica, 2012. **123**: p. 1-11.

231. Nelson, P.T., et al., *ABCC9/SUR2 in the brain: Implications for hippocampal sclerosis of aging and a potential therapeutic target.* Ageing research reviews, 2015. **24**: p. 111-125.

232. Rossiter, H.E., M.-H. Boudrias, and N.S. Ward, *Do movement-related beta oscillations change after stroke?* Journal of neurophysiology, 2014. **112**(9): p. 2053-2058.

233. Espenhahn, S., et al., *Sensorimotor cortex beta oscillations reflect motor skill learning ability after stroke.* Brain communications, 2020. **2**(2): p. fcaa161.

234. Thibaut, A., et al., *Using brain oscillations and corticospinal excitability to understand and predict post-stroke motor function.* Frontiers in neurology, 2017. **8**: p. 261298.

235. Balbi, M., et al., *Gamma frequency activation of inhibitory neurons in the acute phase after stroke attenuates vascular and behavioral dysfunction.* Cell Reports, 2021. **34**(5).

236. Hazime, M., et al., *Prolonged deficit of low gamma oscillations in the peri-infarct cortex of mice after stroke.* Experimental Neurology, 2021. **341**: p. 113696.

237. Zhang, Y., et al., *Fast and sensitive GCaMP calcium indicators for imaging neural populations.* Nature, 2023. **615**(7954): p. 884-891.

238. Van der Zee, P., M. Essenpreis, and D.T. Delpy. *Optical properties of brain tissue*. in *Photon Migration and Imaging in Random Media and Tissues*. 1993. SPIE.

239. Fino, E., et al., *RuBi-glutamate: two-photon and visible-light photoactivation of neurons and dendritic spines.* Frontiers in neural circuits, 2009. **3**: p. 556.

240. Pan, F. and W.B. Gan, *Two-photon imaging of dendritic spine development in the mouse cortex.* Developmental neurobiology, 2008. **68**(6): p. 771-778.

241. Rose, C.R., et al., *Two-photon Na+ imaging in spines and fine dendrites of central neurons.* Pflügers Archiv, 1999. **439**: p. 201-207.

242. Bradke, F., *Mechanisms of axon growth and regeneration: moving between development and disease.* Journal of Neuroscience, 2022. **42**(45): p. 8393-8405.

243. Dhar, M., et al., *Spatiotemporal dynamics of lesion-induced axonal sprouting and its relation to functional architecture of the cerebellum.* Nature communications, 2016. **7**(1): p. 12938.

244. Yamahachi, H., et al., *Rapid axonal sprouting and pruning accompany functional reorganization in primary visual cortex.* Neuron, 2009. **64**(5): p. 719-729.

245. Montaner, J., et al., *Multilevel omics for the discovery of biomarkers and therapeutic targets for stroke.* Nature Reviews Neurology, 2020. **16**(5): p. 247-264.

246. Deng, W., et al., *Transcriptomic characterization of microglia activation in a rat model of ischemic stroke.* Journal of Cerebral Blood Flow & Metabolism, 2020. **40**(1_suppl): p. S34-S48.

247. Simats, A., et al., *A mouse brain-based multi-omics integrative approach reveals potential blood biomarkers for ischemic stroke.* Molecular & Cellular Proteomics, 2020. **19**(12): p. 1921-1936.

248. Wang, R., et al., *RNA sequencing reveals novel macrophage transcriptome favoring neurovascular plasticity after ischemic stroke.* Journal of Cerebral Blood Flow & Metabolism, 2020. **40**(4): p. 720-738.

249. Celikel, T. and B. Sakmann, *Sensory integration across space and in time for decision making in the somatosensory system of rodents.* Proceedings of the National Academy of Sciences, 2007. **104**(4): p. 1395-1400.

250. Cloke, J.M., et al., *A novel multisensory integration task reveals robust deficits in rodent models of schizophrenia: converging evidence for remediation via nicotinic receptor stimulation of inhibitory transmission in the prefrontal cortex.* Journal of Neuroscience, 2016. **36**(50): p. 12570-12585.

251. Siemann, J.K., et al., *A novel behavioral paradigm to assess multisensory processing in mice.* Frontiers in behavioral neuroscience, 2015. **8**: p. 456.

252. Gu, X., et al., *Long-term optical imaging of neurovascular coupling in mouse cortex using GCaMP6f and intrinsic hemodynamic signals.* Neuroimage, 2018. **165**: p. 251-264.

253. Calcinaghi, N., et al., *Multimodal imaging in rats reveals impaired neurovascular coupling in sustained hypertension.* Stroke, 2013. **44**(7): p. 1957-1964.

254. Ma, H., et al., *Simultaneous multi-wavelength optical imaging of neuronal and hemodynamic activity.* Neurovascular coupling methods, 2014: p. 237-249.

255. Sunil, S., et al., *Neurovascular coupling is preserved in chronic stroke recovery after targeted photothrombosis.* NeuroImage: Clinical, 2023. **38**: p. 103377.